Thin Solid Films 660 (2018) 120–160

Contents lists available at ScienceDirect

Thin Solid Films

journal homepage: www.elsevier.com/locate/tsf

Critical review

Recent developments in surface science and engineering, thin films, nanoscience, biomaterials, plasma science, and vacuum technology

M. Mozetič[a,b], A. Vesel[a,b], G. Primc[a,b], C. Eisenmenger-Sittner[a,c], J. Bauer[a,c], A. Eder[a,c], G.H.S. Schmid[a,c], D.N. Ruzic[a,d], Z. Ahmed[a,e], D. Barker[a,e], K.O. Douglass[a,e], S. Eckel[a,e], J.A. Fedchak[a,e], J. Hendricks[a,e], N. Klimov[a,e], J. Ricker[a,e], J. Scherschligt[a,e], J. Stone[a,e], G. Strouse[a,e], I. Capan[a,f], M. Buljan[a,f], S. Milošević[a,g], C. Teichert[a,h], S.R. Cohen[a,i], A.G. Silva[a,j], M. Lehocky[a,k], P. Humpoličeк[a,k], C. Rodriguez[a,l], J. Hernandez-Montelongo[a,l,m], D. Mercier[a,n], M. Manso-Silván[a,l], G. Ceccone[a,o], A. Galtayries[a,n], K. Stana-Kleinschek[a,p], I. Petrov[a,q], J.E. Greene[a,q,*], J. Avila[a,r], C.Y. Chen[a,r], B. Caja-Munoz[a,r], H. Yi[a,r], A. Boury[a,r], S. Lorcy[a,r], M.C. Asensio[a,r], J. Bredin[s], T. Gans[a,s], D. O'Connell[a,s], J. Brendin[a,s], F. Reniers[a,t], A. Vincze[a,u], M. Anderle[a,v], L. Montelius[a,w]

[a] International Union for Vacuum Science, Technique and Applications, Avenue de la Renaissance 30, B-1000 Brussels, Belgium
[b] Jozef Stefan Institute, Jamova cesta 39, 1000 Ljubljana, Slovenia
[c] Techical University Vienna, Wiedner Hauptstrasse 8–10, A-1040 Vienna, Austria
[d] Department of Nuclear, Plasma and Radiological Engineering, University of Illinois at Urbana-Champaign, 104 S Wright St., Urbana, IL 61801, USA
[e] NIST, 100 Bureau Drive, Gaithersburg, MD 20899, USA
[f] Rudjer Bošković Institute, Bijenička cesta 54, 10000 Zagreb, Croatia
[g] Institute of Physics, Bijenička cesta 46, 10000 Zagreb, Croatia
[h] Institute of Physics, Montanuniversität Leoben, Franz Josef Str. 18, 8700 Leoben, Austria
[i] Weizmann Institute of Science, Herzl 234, Rehovot 7610001, Israel
[j] Universidade Nova de Lisboa, Campus da Caparica, P-2829-516 Caparica, Portugal
[k] Centre of Polymer Systems, Tomas Bata University in Zlin, Nam. T G Masaryka 5555, 760 01 Zlin, Czech Republic
[l] Departamento de Física Aplicada and Instituto de Ciencia de Materiales Nicolás Cabrera, Universidad Autónoma de Madrid, 28049 Madrid, Spain
[m] Departamento de Física Aplicada, Universidade Estadual de Campinas, 13083-859 Campinas, São Paulo, Brazil
[n] Chimie ParisTech, PSL Research University, CNRS, Institut de Recherche de Chimie Paris, 75005 Paris, France
[o] European Commission, Joint Research Center, Via Enrico Fermi, 21020 Ispra, Va, Italy
[p] University of Maribor, Smetanova 17, 2000 Maribor, Slovenia
[q] University of Illinois, Department of Materials Science, 104 S. Goodwin Avenue, Urbana, IL 61801, USA
[r] Synchrotron SOLEIL and Université Paris-Saclay, L'Orme des Merisiers, 91190 Saint-Aubin, BP 48, France
[s] York Plasma Institute, Department of Physics, University of York, Heslington, York YO10 5DD, UK
[t] Universite Libre de Brixelles, CP260, boulevard du Triomphe, 1050 Bruxelles, Belgium
[u] International Laser Centre, Ilkovicova 3, 84104 Bratislava, Slovakia
[v] Italian Embassy in Hanoi, 9, Le Phung Hieu, Hanoi, Viet Nam
[w] International Iberian Nanotechnology Laboratory, Avenida Mestre José Veiga s/n, 4715-330 Braga, Portugal

ABSTRACT

Nanometer-sized structures, surfaces and sub-surface phenomena have played an enormous role in science and technological applications and represent a driving-force of current interdisciplinary science. Recent developments include the atomic-scale characterization of nanoparticles, molecular reactions at surfaces, magnetism at the atomic scale, photoelectric characterization of nanostructures as well as two-dimensional solids. Research and development of smart nanostructured materials governed by their surface properties is a rapidly growing field. The main challenge is to develop an accurate and robust electronic structure description. The density of surface-related trap states is analyzed by transient UV photoconductivity and temperature-dependent admittance spectroscopy. An advanced application of thin films on shaped substrates is the deposition of catalytic layers on hollow glass microspheres for hydrogen storage controlled exothermal hydrolytic release. Surface properties of thin films including dissolution and corrosion, fouling resistance, and hydrophilicity/hydrophobicity are

* Corresponding author at: International Union for Vacuum Science, Technique and Applications, Avenue de la Renaissance 30, B-1000 Brussels, Belgium.
E-mail address: jegreene@illinois.edu (J.E. Greene).

https://doi.org/10.1016/j.tsf.2018.05.046

Available online 31 May 2018

explored to improve materials response in biological environments and medicine. Trends in surface biofunctionalization routes based on vacuum techniques, together with advances in surface analysis of biomaterials, are discussed. Pioneering advances in the application of X-ray nanodiffraction of thin film cross-sections for characterizing nanostructure and local strain including in-situ experiments during nanoindentation are described. Precise measurements and control of plasma properties are important for fundamental investigations and the development of next generation plasma-based technologies. Critical control parameters are the flux and energy distribution of incident ions at reactive surfaces; it is also crucial to control the dynamics of electrons initiating non-equilibrium chemical reactions. The most promising approach involves the exploitation of complementary advantages in direct measurements combined with specifically designed numerical simulations. Exciting new developments in vacuum science and technology have focused on forward-looking and next generation standards and sensors that take advantage of photonics based measurements. These measurements are inherently fast, frequency based, easily transferrable to sensors based on photonics and hold promise of being disruptive and transformative. Realization of Pascal, the SI unit for pressure, a cold-atom trap based ultra-high and extreme high vacuum (UHV and XHV) standard, dynamic pressure measurements and a photonic based thermometer are three key examples that are presented.

1. Introduction

Surface and sub-surface phenomena play crucial roles in functional properties of solid or liquid materials and have been preferred research objectives over the past decade. The complexity of the phenomena requires a multi-disciplinary approach from such diverse fields as pure and applied surface science, surface engineering and biointerfaces, thin films, nanometer structures and electronic materials. Surfaces and subsurfaces are often tailored by non-equilibrium states of gases, so the phenomena are frequently addressed by researchers skilled in plasma science and technology. Additionally, the functional properties of solid or liquid materials are often tailored under low-pressure or vacuum conditions. In fact, the majority of advanced techniques for surface and sub-surface characterization employ high or ultra-high vacuum conditions; therefore, the contribution of vacuum science and technology is essential. All above stated scientific fields are joined under the International Union for Vacuum Science and Applications – IUVSTA [1]. IVUSTA recognizes recent advances in above-stated scientific fields and prepares review papers based on highlight seminars which are organized every three years. The preceding review paper was published in 2014 [2], and the present paper highlights achievements in past few years that have been selected by chairs of IUVSTA scientific divisions. It includes highlights from all the fields mentioned above, as well those from vacuum science and technology.

2. Smart materials of nano-scale dimensions

Here we present a comprehensive review of the latest developments in instrumentation, techniques, and methodologies in the area of surface science motivated by the study of smart materials [3]. Advanced materials offer interesting solutions for many applications in powder metallurgy, technical ceramics, production and harvest of alternative energy sources, nanoelectronics [4], catalysis and additive manufacturing. Furthermore, nanomaterials are coming into use in healthcare, electronics, cosmetics, solar cells, textiles, information technology, environmental protection and other areas [5–8]. Their physical and chemical properties often differ from bulk materials due to quantum effects at such small dimensions. For nanomaterials, the surface to volume ratio is high, in many cases, only surface atoms constitute several of these materials, with just a few, or no, atoms constituting the bulk of the material, see Fig. 1. For example, graphene - a hexagonal arrangement of carbon atoms one atom thick and two-dimensional (2D) transition metal dichalcogenides (TMD), i.e. MoS_2, WSe_2, ReS_2, $MoSe_2$, WS_2, $ReSe_2$ as well as their derived hetero-structures, have much more interesting applications when they are used as mono- or diatomic thick materials.

The widespread use of nanomaterials calls for life cycle risk assessment. Therefore, it is important to understand the risks these new materials pose to the potential health risks of workers, consumers the environment [9].

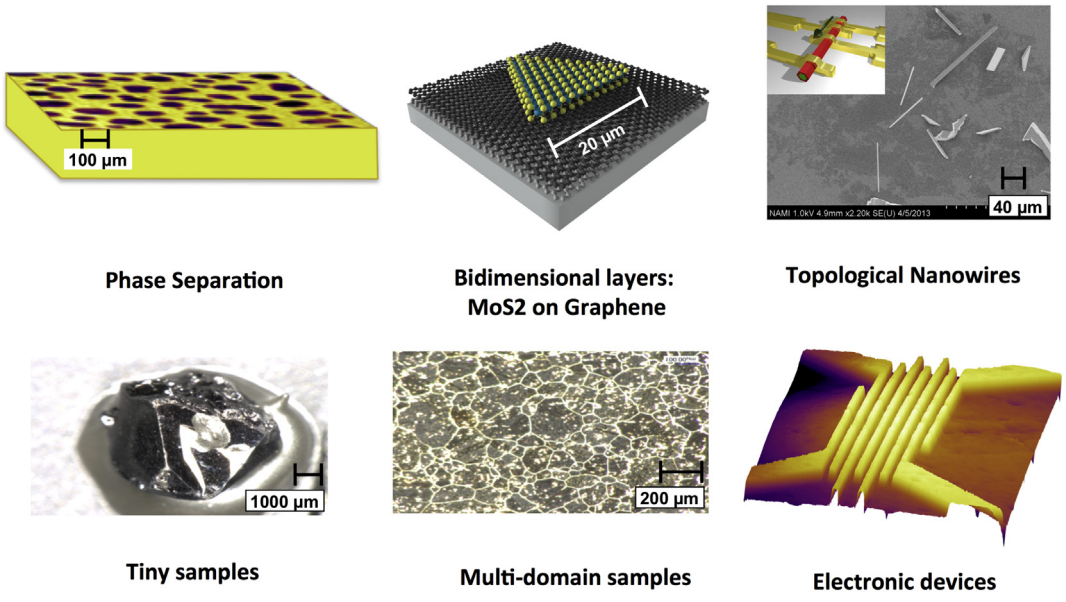

Fig. 1. The panels of the figure show a few examples where either the surface concentrations or the small size objects require high lateral resolution detection.

Certainly, nanomaterials require special characterization techniques, which must be able to precisely define their shape, size and the specific surface area, the number and/or size distribution as well as ability to stick together or remain dispersed in different environments. Their chemical properties are also relevant: the molecular structure, elemental composition, stability, alternative stoichiometry, surface chemistry and, in particular, their degree of dispersion in water, oils, fats or other liquids or solids.

3. Advanced surface characterization techniques

A range of powerful techniques have been developed to allow characterization of nanoparticles, microscopic objects and the first atomic surface layers of bulk materials. Moreover, new methods are under development, to tackle chemical and physical properties of this class of small objects, low dimensional or confined materials. We present a brief discussion of remarkable instrumental advances in *spectroscopic techniques* based on the realization of new light sources of modulated and tunable X-ray sources like synchrotron radiation installations and their application in chemical imaging. Microscopy, which has been in use since the sixteenth century, is now powerful enough to detect, identify, track, and manipulate single molecules on surfaces, in solutions, and even inside living cells. However, despite these advances, today's demands on imaging have grown well beyond traditional photographic images. The new frontiers in microelectronics, molecular biology, and chemical manufacturing demand scientists and engineers to push the limits of technology in pursuit the imaging of the *chemical and electronic properties* of nano-materials. Hence, the ability to visualize atomic and molecular structures, their interactions and chemical compositions over the spatial range of nanometers to micrometers in optically challenging environments is particularly attractive to large audiences. Smart nano-objects with remarkable properties can be synthetized nowadays, but would have remained almost unexploited if new and advanced tools were not available for their characterization at a variable scale from a few micrometers down to tens of nanometers. Hence, the precise and fine electronic and compositional description of advanced materials and, more specifically, their surfaces and sub-surfaces have been revealed to be rather intricate, particularly when the novel materials are affected by phase separation. This is the case of doped Mott insulators or magnetic domains, composites with nano- or microcrystallites embedded in isolating or flexible host materials as well as nano- or micropattered objects, among others.

Recently, a tremendous and fast expansion in modern microscopic methods has been realized. However, beyond the achievement of *Ångstrom* spatial resolution, the challenge remains in consolidating energy resolved spectroscopic methods with lateral nanometric resolution. A fine chemical and electronic analysis with submicron spatial discrimination has been revealed to be indispensable for many scientific problems. X-ray scanning spectromicroscopy, both photoelectron and X-ray absorption are in this sense techniques based on high brilliance tunable synchrotron radiation (SR) sources, which can be considered as unique for providing both spatial resolution and chemical sensitivity [10–13].

The last two decade of chemical imaging has been enabled by development of novel techniques such as near edge X-ray absorption (NEXAFS), photoelectron spectroscopy (PES), X-ray scanning transmission microscopy (SXTM) [12] and scanning photoelectron microscopes (SPEM). Fig. 2 schematically summarizes the most relevant X-ray based imaging techniques able to provide chemical and electronic mapping, with nanometer spatial resolution, of surfaces of heterogeneous samples.

In the scanning X-ray photoelectron microscopy approach, X-ray photon optics focus the incident photon beam onto the sample which is rastered across the beam. Detection of emitted photoelectrons at each illumination point enables us to build a chemically information rich image of the material. Scanning photoelectron microscopy (SPEM) has

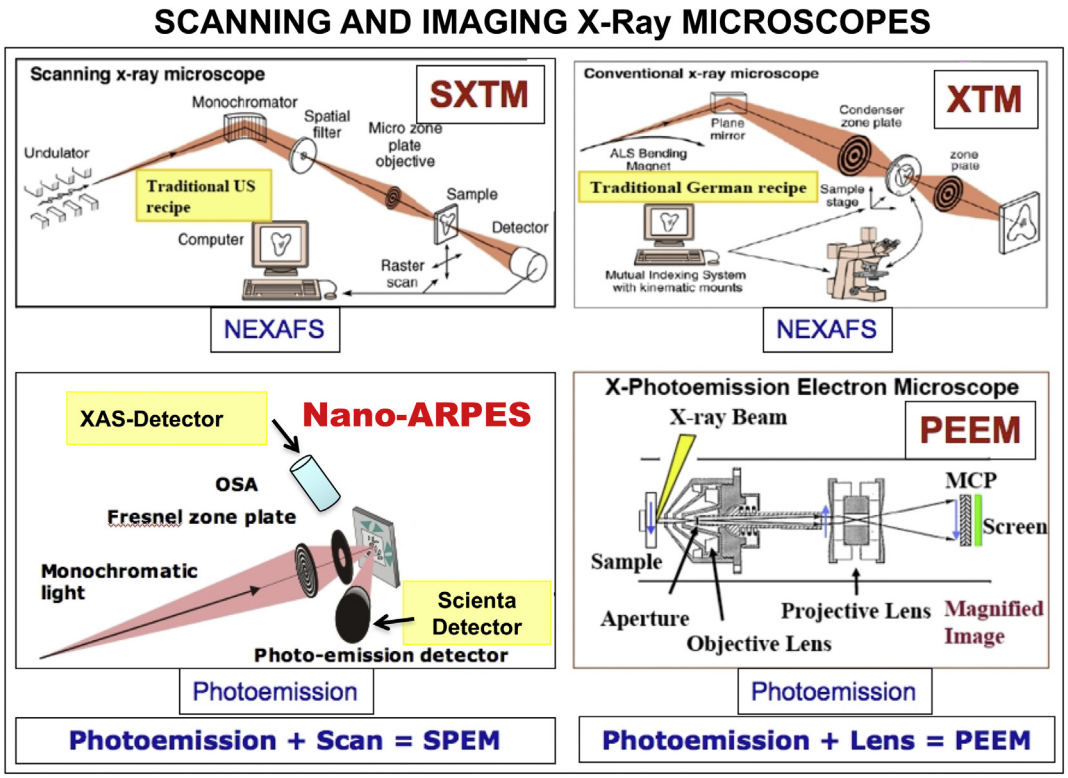

Fig. 2. Schematic representation of the more developed X-ray imaging techniques. The figure shows the layout of Scanning Transmission X-ray Microscope (SXTM), X-ray Transmission Microscope (XTM), Photoemission Electron Microscopy (PEEM), Scanning Photoelectron Microscopy (SPEM) and nano Angle Resolved Photoelectron Spectroscopy (nanoARPES).

been almost exclusively been used to record core levels (CLs) and their chemical shift which is directly related to the oxidation state of the elemental components of the analyte. The use of SPEM to investigate the valence band electronic states is challenging because the valence states' cross section decreases above 250 eV photon energies.

A major area of focus is the impact of heterogeneities and confinement on the delocalized or partially localized electronic states of the valence band of surfaces and subsurface areas of advanced materials. This requires a thorough understanding of electronic structures whose electronic states (binding energy < 20 eV) are directly responsible for the chemical bonds, reactivity, electrical transport as well as the thermal and mechanical properties of solid matter.

In addition to a rich set of classical nano- and micro-spectroscopic imaging techniques using X-ray as exciting probes (i.e. SXTM, XTM, PEEM, SPEM), new important developments have been reported in infrared imagery [10–16]. Effectively, the atomic force microscope (AFM) tip has been combined with infrared micro-spectroscopy producing a new type of imagery with chemical information at nanometer resolution. This new tool has been particularly successful in the study of biological materials [17–19]. Most importantly, angle resolved photoemission spectroscopy on nano-scale (nanoARPES) with a very high energy, angular and lateral resolution has been demonstrated as one of the most powerful and innovative techniques [20,21], able to characterize even tiny electronic features of small objects and heterogeneous surfaces. However, the implementation of nanoARPES in the low excitation photon energy range ($h\nu < 150$ eV) has long been considered impracticable due to the demanding steric restrictions associated with the conventional ARPES technique. In particular, the construction of a typical synchrotron beamline (BL), where the nanometer lateral resolution could be combined with the precise high energy and reciprocal space resolution of the ARPES technique, has been considered by many experts fully unreasonable for a long time. These reserves were based on extremely demanding requirements concerning the angular and spatial degrees of freedom associated with typical ARPES geometry detection and the demanding utilization of small and fragile Fresnel zone plates to focus the X-ray beams.

The accessibility of third generation synchrotron soft X-ray radiation facilities with new low-emittance SR storage rings that come equipped with long insertion devices and accurate electron orbits control has contributed to the rapid development of microspectroscopy. The ultra-high brightness of these sources is suitable for demanding techniques, like ARPES and scanning photoemission microscopy. This fruitful combination is able to register the dispersive energy-momentum spectrum (by angular resolved photoemission) on micro- and nanosamples as well as performing “electronic imaging” by recording the valence band states with high energy, angular and spatial resolution.

4. Recent progress in instruments for beamlines

The most powerful spectroscopic techniques are implemented in large installations using synchrotron radiation sources. Typical beamlines effectively integrate one or more insertion devices with high transmission beamline optics, see Fig. 3. These photon sources, frequently in a tandem configuration, are installed in medium straight sections of the storage rings and commonly provide both linearly and circularly polarized X-rays. The design of the beamline (BL) optics insures a homogeneous and coherent illumination of the focalization lens. This new generation of synchrotron-based beamlines combines nanofocalization of the X-ray source with efficient monochromators, which provide unique capabilities of lateral resolution with high-energy monochromaticity. These two properties have been revealed to be mandatory for the current successful evolution of spectroscopic techniques in surface science and in the characterization of advanced materials in general.

These powerful photon sources have been completed with advanced nanopositioning manipulators, with a multi-axis sample handling abilities. Furthermore, this type of setup is fully compatible with high energy and angular resolution electron analyzers. These efficient photoelectron analyzers are currently available in the market and enable precise recordings of high-resolution core levels, chemical shifts, resonant photoemission determinations as well as photoelectron diffraction experiments. These constitute a powerful battery of characterization techniques, frequently with different depth analysis, which can provide chemical and electronic information of the surface and subsurface area of a wide variety of materials. In fact, metals, semiconductors, and even insulators can be studied spectroscopically with high lateral and energy resolution. Importantly, in these setups, precise in-vacuum piezo movers with their corresponding encoders allow not only the scanning and precise positioning of tiny samples, but also a fast and highly reproducible (less than a few micrometers) alignment of the instrument with respect to the photon beam and the analyzer focus in a short period of time.

The BLs devoted to micro-space and nano-imagery require extremely stable operation conditions for the synchrotron radiation sources. They generally operate in top-mode, which keeps the electron current in the storage ring constant at a given (rather high) injected current in the rings, i.e. 400 mA, thus ensuring a constant heat load and

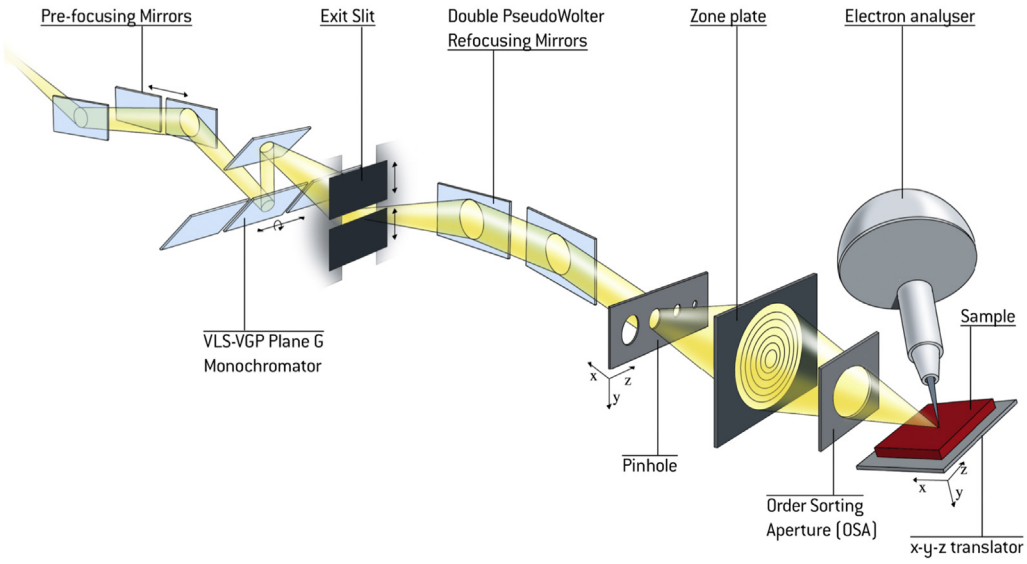

Fig. 3. Schematic representation of the basic components of a typical nanoARPES beamline. The first pre-focusing mirrors collimate the undulator beam to a plane grating monochromator with two gratings that can be exchanged by remote control. The second set of mirrors, or pseudo Wolter post-localization mirrors, refocuses the beam alternatively onto the sample or the pinhole, depending on whether a micro- or a nanometer spot size is required. The Fresnel zone plate (FZP) focusing system is also included in the nanoARPES end-station, together with an order selection aperture (OSA) placed between the FZP and the sample, in order to suppress unwanted diffraction orders. Reproduced with permission from Ref. [22].

consequently minimal thermal drifts within the storage ring and associated optics of the beamlines. Taking advantage of very efficient plane-grating monochromators (PGM) combined with Varied Linear Spacing (VLS) gratings, the last generation of soft X-ray BLs combine a high resolving power, an excellent harmonic rejection ratio and a high photon flux throughout the whole working energy range, which is particularly compatible with an extremely demanding focalization lens like FZPs. Typically, the photon flux on a sample is 6.4×10^{12} photons/s/0.01% BW working in micro-spot mode, and 5.4×10^{10} photons/s/0.01% BW for nano-spot experiments, with a standard resolving power of 32,000 at 67 eV photon energy.

The experimental end-stations are equipped with an analysis chamber containing a microscope, a preparation chamber with gas lines and a fast entry chamber, which allows a fast sample transfer from atmospheric to ultra-high vacuum conditions. The hutch accommodates the pinhole chamber and the analysis chamber that contains the electron analyzer and nano-spot focusing optics. To ensure a precise nanometer scan of the sample, both the thermal drift and the mechanical vibrations are minimized by an interferometric control. The thermal variation is stabilized to be lower than 0.1 °C and the mechanical vibrations are minimized to have only spurious displacements, which are compensated by the interferometric system.

The main difference between a scanning X-ray microscope and other conventional spectroscopic instruments, in particular a nanoARPES microscope or *k*-microscope, is that the specimens are mounted on a high-precision plate that ensures their nanoscale positioning in the *x*, *y* and *z* directions. The polar angle (Θ) and the azimuthal angle (Ψ) can also be automatically scanned over a 90° range. Finally, the soft X-ray beam, with controlled linear or circular polarization, can be focused to about 30 nm (or better), depending on the quality of the FZP lenses used. In general, the *k*-microscopes currently available have two operating modes: spectroscopic analysis with nano-spot and spectroscopic mapping.

To ensure the lateral nanometer resolution, *k*-microscopes are equipped with a continuous interferometric control of the samples position with respect to the FZPs, which prevents undesirable distortions of the recorded images. Thus, the accurate real-time recording of the X-ray spot location on the sample by interferometry is automatically converted to a digital signal that control, by a feedback closed-loop, the scanning positioning of the specimen [23].

5. Nano-positioning and focalization of scanning microscopes

In a scanning X-ray microscope, a sample is illuminated and scanned by a small well-collimated X-ray spot extracted from the synchrotron radiation ring, thus creating an image one pixel at a time. As only a spot of nanometer size on the sample is illuminated, several excitation particles or light produced by this illumination can be detected with high spatial resolution. Effectively, *k*-microscopes can utilize several

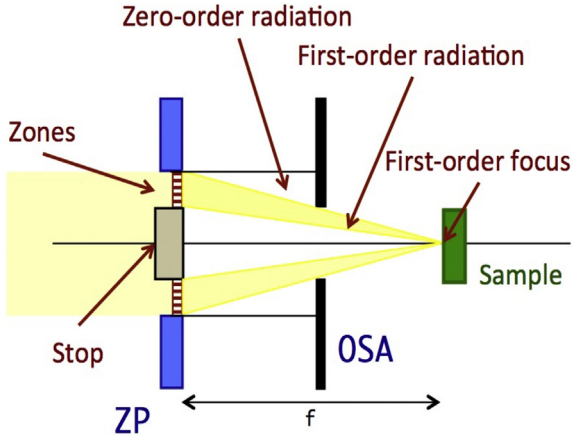

Fig. 5. Disposition of the focusing scheme of ANTARES (A New Tailored Angle REsolved Spectroscopies) microscope, composed by the FZP plate and OSA.

signals that can be detected and synchronized with the spatial scanning.

A high precision three-axis *x*, *y* and *z* piezoelectric stage is used for fine motion, typically a maximum range of 300 μm in each direction with a precision of 1 nm. Generally, this *x*, *y* and *z* piezo stage is mounted on top of a second *x*, *y* and *z* stepping motor stage that provides motion in excess of several millimeters, in order to ensure coarse positioning of the samples. Besides lateral motions, polar (θ) and azimuthal (φ) angular step motors are also mounted in this coarse top stage in order to be able to select the azimuth of the samples and also to change the incident photon angle as well as the exit angle of the excited photoelectrons, see Fig. 4.

In order to focus on the X-ray photon, a variable line-spacing circular diffraction is utilized, denominated the Fresnel zone plate (FZP) lens. Moreover, unwanted diffraction orders that would decrease the available signal-to-background ratio are suppressed by the central stop of the FZP. Also, a smaller pinhole, the order selection aperture (OSA), is situated between the zone plate and the sample at about 0.75 times the zone-plate-to-sample distance. The OSA ensures that only the first diffraction order of the FZP is able to illuminate the sample after being transmitted by the FZP (see Fig. 5). Careful transverse and longitudinal alignment of the OSA with the zone plate is an essential aspect of tuning and operating a scanning X-ray microscope. The alignment determines the imaging properties of the microscope and the higher-order spectral contamination that may pass the zone-plate/OSA setup.

The spatial resolution of the obtained images is determined by the size of the outermost zone width Δr at a given wavelength of the incident X-rays, following the equation; $SR = \lambda/(2\Delta r)$. For fully coherent illumination, plane-waves or point sources depend on the size of the central stop relative to the size of the zone plate and ranges from 0.9 Δr to 1.22 Δr [21]. In practice, a finite source is used for illumination, and

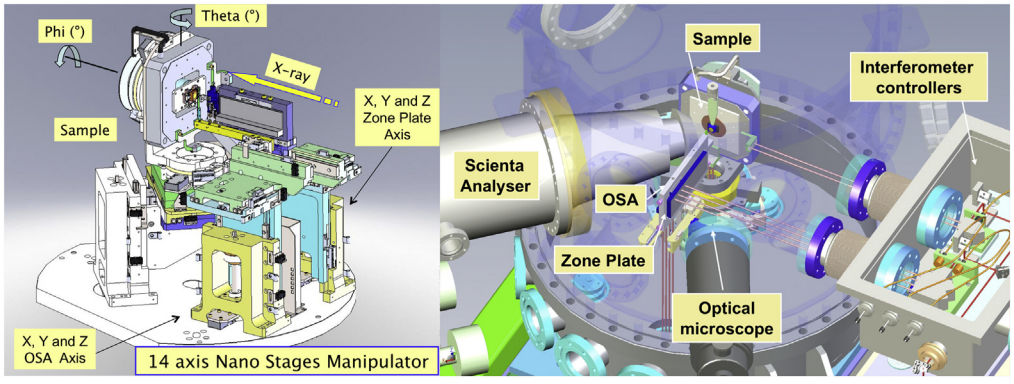

Fig. 4. Schematic description of typical scanning microscopes main components.

the diffraction pattern is convolved with the de-magnified finite source to obtain the actual point-spread function of the X-ray scanning microscope. In order to achieve adequate performance the FZPs have to be placed with an absolute accuracy of about 0.3 Δr [21]. The best achievable spatial resolution depends on the capabilities of the zone-plate-fabrication technology and on the degree of coherence of the illuminating beam. Zone plates with outermost zone widths as small as 20 to 25 nm are currently being fabricated and some are already available. However, their cost is an exponential function of their spatial resolution.

Fresnel zone plates are achromatic focalizing lenses with a variable focal length depending on the photon energy. Thus, every time that the incident energy should be changed, the X-ray scanning microscope has to be refocused synchronously with the photon energy changes. Unfortunately, refocusing stages exhibit transverse spurious motions, which are commonly referred to as run-out motions, of the order of several hundreds of nanometers, during a given translation. If these movements are not controlled, they will dramatically affect the quality of the recorded images. In fact, the sample portion illuminated change during the registration producing a "blurring" of features and a clear degradation of the image contrast. In order to achieve the submicron spatial resolution, these undesired motions as well as uncontrolled vibration and dilation of the scanning stages should be precisely measured and automatically compensated, almost continuously. This nano-positioning control is accomplished by a complete ad-hoc interferometer system.

In X-ray scanning microscopes, due to the numerous nano-positioning motors, encoders, several detectors, optical beamline components and other individual devices, manual operation of the beamline becomes unfeasible. Most of the instrumentation utilized in these types of BLs should have their counterpart as virtual devices, which permit their automatic control via a connection to large framework bus software. The programming of these devices is not user friendly and therefore a powerful interface is generally developed, which integrates all scientific applications needed for the end users as well as the control and alignment of all the beamline components.

6. New trends in surface science research

In this section, we will describe some scientific areas that have shown a strong increase of activity in connection with surface science studies and spectroscopic imaging. Many small domain materials have recently been synthesized. Hence, micro-nanoimaging techniques are critical to characterize their electronic and chemical properties. Moreover, recent discoveries, particularly in materials with electronic applications, have demonstrated that metals and semiconductors present a wide variety of interesting properties when only a few atomic layers are utilized. For these materials where all the atoms are at the surface, the only way to characterize their properties is using typical surface science techniques combined with high lateral spatial resolution. In the next subsection, we will introduce the most remarkable materials where the surface science community has shown particular interest.

Graphene, an isolated single atomic layer of graphite, is an ideal two-dimensional system. This new electronic system exhibits a large number of unique transport properties. An outstanding number of studies have been dedicated to this material and its derivatives. Mono- and multilayer graphene with and without doping and functionalization have been studied using Raman, IR, diffraction, transmission electron microscopy and many other techniques. Excellent ARPES and nano-ARPES studies have given insight on the relation between CLs and reactivity. Fig. 6 describes different types of graphene commonly used in these studies. They are usually, (1) single and multilayer graphene epitaxially and non-epitaxially grown on silicon and carbon-terminated single-crystal silicon carbide, (2) graphene obtained by CVD (chemical vapor deposition) on copper foils, and (3) exfoliated graphene and transported graphene being part of artificial heterostructures.

6.1. Graphene grown on SiC single crystals

Graphene is a single layer of carbon atoms arranged in a hexagonal honeycomb structure. This fascinating material is known to host very peculiar charge carriers (electrons or holes), called "Dirac massless fermions," which generate outstanding and promising transport properties. When two graphene layers are stacked together, the system differs drastically from monolayer graphene. By introducing a rotation (twist) angle of several degrees between the two graphene layers, scientists are now unravelling additional and intriguing electronic properties.

Figs. 7 and 8 show several graphene layers grown on a SiC single crystal. The graphene growth was carried out on the silicon- and carbon- terminated SiC crystals. In the first case, the graphene is epitaxially mono-oriented with large terraces. Graphene films grown on the C-plane of the SiC(0001) crystal, however, is composed by monocrystalline islands of different size with a large variety of the azimuthal orientations. The ARPES and nanoARPES data show, respectively, the remarkable different electronic properties of the graphene grown on these two different substrates [24,25].

Strictly speaking, graphene is only a single sheet of C atoms. The electronic properties of graphene change when several layers are stacked on top of each other. Currently, there are different experimental and theoretical models on the stacking of multilayer graphene namely; AB stacking, AA stacking, ABC (rhombohedral) stacking and rotated graphene layers. In AB stacking, the two adjacent layers are shifted exactly as in bulk graphite whereas in AA stacking, the carbon atoms of two adjacent layers have exactly the same lateral positions.

In ABC stacking, each layer is laterally shifted with respect to the layer below by a third of a diagonal of the lattice unit cell, while rotated graphene layers are stacked in such a way that the angles of rotation between consecutive graphene layers deviate from the AB stacking.

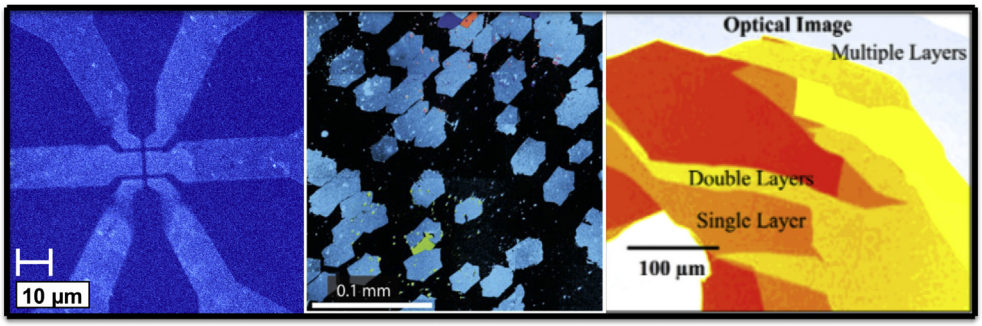

Fig. 6. Left panel shows epitaxial graphene on a SiC Si face connected with gold lines for transport measurements, middle panel depicts monocrystalline large graphene islands grown by CVD on copper foil, and the right panel shows exfoliated single- double- and multi-layer graphene on SiO_2.

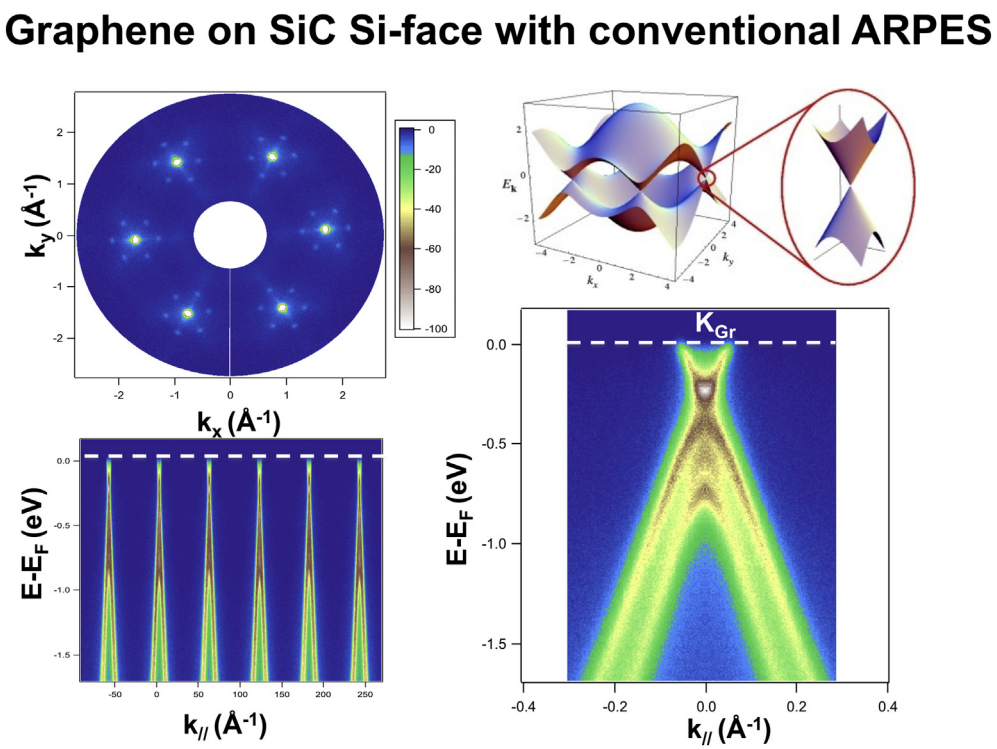

Fig. 7. Top left panel shows the Fermi surface of graphene on Si-terminated SiC (k_x: momentum of the electrons in the solid in X axis of the crystal; k_y: momentum of the electrons in the solid in Y axis of the crystal); top right panel depicts the theoretical electronic band structure of graphene; bottom left panel the azimuthal cut of the Fermi surface of the top left panel graph; and bottom right panel represents the binding energy with respect to the Fermi level ($E-E_F$) as a function of the momentum of the electrons in the solid parallel to the surface ($k_{//}$).

Graphene grown on the two polar faces (Si-face and C-face) of SiC have different structural and electronic properties (Figs. 7 and 8). The orientation dependence of graphene relative to the underlying SiC and graphene depends on the considered face, as observed for example in their low-energy electron diffraction (LEED) pattern. Graphene spots on the Si-face appear sharp and manifest the constant AB (Bernal) stacking of the carbon layers. On the C-face, they are smeared out into continuous diffraction rings (although with preferred rotation angles), which implies contributions from either rotated adjacent layers and/or islands of different azimuthal directions.

Fig. 8 shows in detail the type of stacking of graphene layers on the C-face of SiC by studying the electronic structure of multilayer graphene imaging the same region of the surface using both nanoARPES and nano-CL imaging on the same area of the samples. By probing the same region of the sample, it was possible to distinguish two different types of graphene islands. The islands have radically different coverage and orientation. The size, distribution, and register of the substrate for each type of island have been determined. Most interestingly, it was evidenced that multilayer graphene islands grown on C-face SiC have the same Bernal staking as when graphene is grown on Si-face SiC crystals. However, in the first case, films are composed of islands with different orientation and thicknesses, while in the second case only one orientation is obtained.

Topological insulator (TI) is a new state of matter. These materials are characterized by a full insulating gap in the bulk and gapless spin-resolved surface states, in which the spin of the electrons is locked perpendicular to its momentum by the strong spin-orbit interaction. These helical spin properties of Dirac fermions in surface states have made them relevant for exotic new physics, and applications on improved spintronic devices and potentially useful for quantum computing. In three-dimensional (3D) TIs, the topological surface states have been mainly studied by ARPES and nanoARPES [11], scanning tunneling microscopy [11] and electrical transport measurements including two-dimensional (2D) weak antilocalization, Shubnikov-de Haas or quantum Hall effect. [11] For topological nano-objects, see Fig. 9, nanoARPES arises as the unique tool able to tackle electronic structure.

6.2. Transition metal dichalcogenides

Recent advances in fabrication of ultrathin layered materials down to unit cell thickness (monolayers) have enabled explorations of new low-dimensional physics, as exemplified by massless Dirac fermions and anomalous quantum Hall effects observed in monolayer graphene. Layered transition metal dichalcogenides represent another class of materials, in which d-electron interactions give rise to new physical phenomena. MoS_2 and derived materials are prototypical transition metal chalcogenide materials. In MoS_2, covalently bonded S-Mo-S sheets are bound by weak van der Waals forces to form the 3D compound. In its bulk form, MoS_2 is a semiconductor with an indirect bandgap of about 1 eV and it has been exploited for photovoltaic and photocatalytic applications due to its strong absorption in the solar spectrum region. Quantum confinement effects on the electronic structure and optical properties of MoS_2 have been previously observed in MoS_2 thin films as well as in MoS_2 nanoplates and nanotubes. Recently many academic and industrial research groups have dedicated a lot of effort to deeply characterize the synthesis, structural, electronic and chemical properties of a wide variety of 2D materials.

6.3. van der Waals heterostructures: MoS_2/graphene interface

Research on graphene and other two-dimensional atomic crystals is intense and is likely to remain one of the leading topics in condensed matter physics and materials science for many years. Looking beyond this field, isolated atomic planes can also be reassembled into designer heterostructures made layer-by-layer in a precisely chosen sequence. See Figs. 10 and 11.

The first, already remarkably complex, such heterostructures (often referred to as ‘van der Waals’) have recently been fabricated and investigated, revealing unusual properties and new phenomena. Here, we review this emerging research area and identify possible future directions. With steady improvement in fabrication techniques and using graphene's springboard, van der Waals heterostructures should come into a large field of their own.

The potential applications of van der Waals heterostructures,

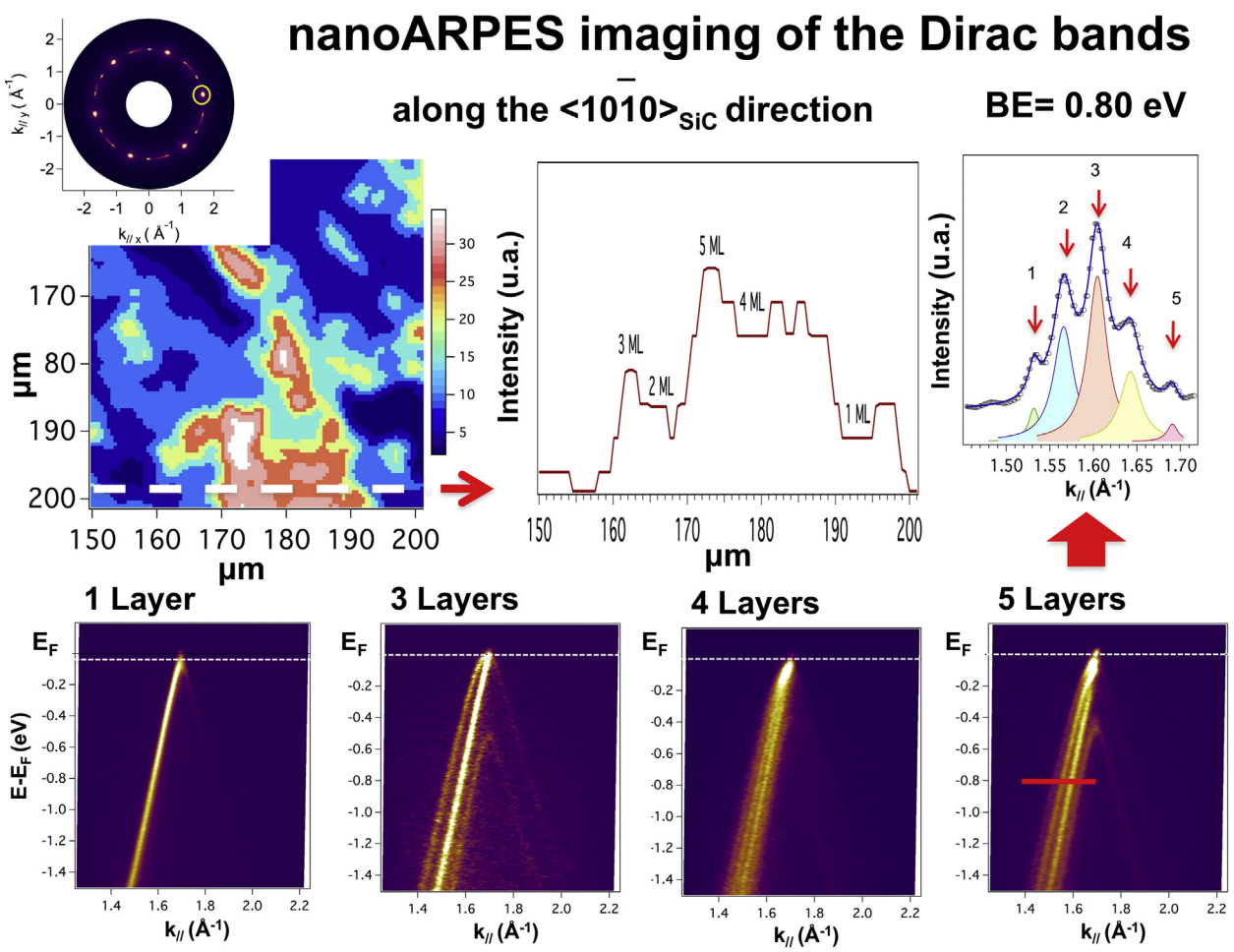

Fig. 8. Top left panel show a two-dimensional nanoARPES image of the measured integrated intensity of the graphene π-band. Lower panels show single point nanoARPES spectra of individual graphene islands indicated in the nanoARPES image. Islands of multilayer coexist with mono-, bi-, and tri-layer graphene in two principal substrate directions. Most of the mono-crystalline islands are a few micrometers and some of them are of sub-micrometer size, depending on in-plane orientation.

including the graphene/MoS_2 interface, have been recently reported in field effect transistor devices or for energy harvesting materials, [26] demonstrating the practical potential for such heterostructures. Hence, the need for better understanding of the electronic properties interfaces is unambiguous. The heterostructure can be realized by transferring the graphene on top of the MoS_2. Graphene films have been previously grown by chemical vapor deposition (CVD) on copper foils.

Only high-spatial resolution ARPES is able to combine multi- and single-island imaging to record the Fermi surface topology of the heterostructure and the electronic band dispersion along the high symmetry directions in reciprocal space. The first results, reported by Coy Diaz et al. [27], uncover the low energy electronic dynamics of the system down to individual pristine graphene islands in contact with MoS_2 surfaces. Thus shedding light on fundamental features like layer doping, gap-size and Fermi velocity, as well as interface hybridization of the graphene/$MoSe_2$ interfaces and heterostructures [28]. Most importantly, while the Dirac cone of graphene remains intact and no significant charge transfer doping has been detected, the formation of band gaps was observed in the π -band of graphene, away from the Fermi-level, due to hybridization with states from the MoS_2 substrate.

6.4. Silicene, phosphorene, germanene and many others

The outstanding properties of graphene and the success of its preparation, from small flakes by mechanical exfoliation to large (centimeter in size) sheets upon deposition on polycrystalline copper foils,

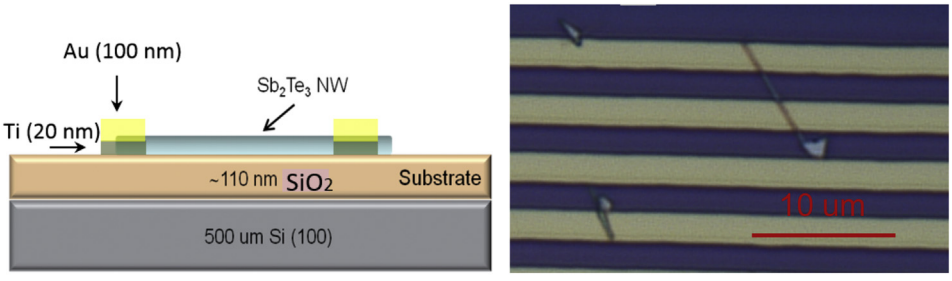

Fig. 9. Left panel shows a topological Sn_2Te_3 nanowire on a SiO_2 substrate patterned with gold; right panel, a SiO_2 substrate patterned with gold.

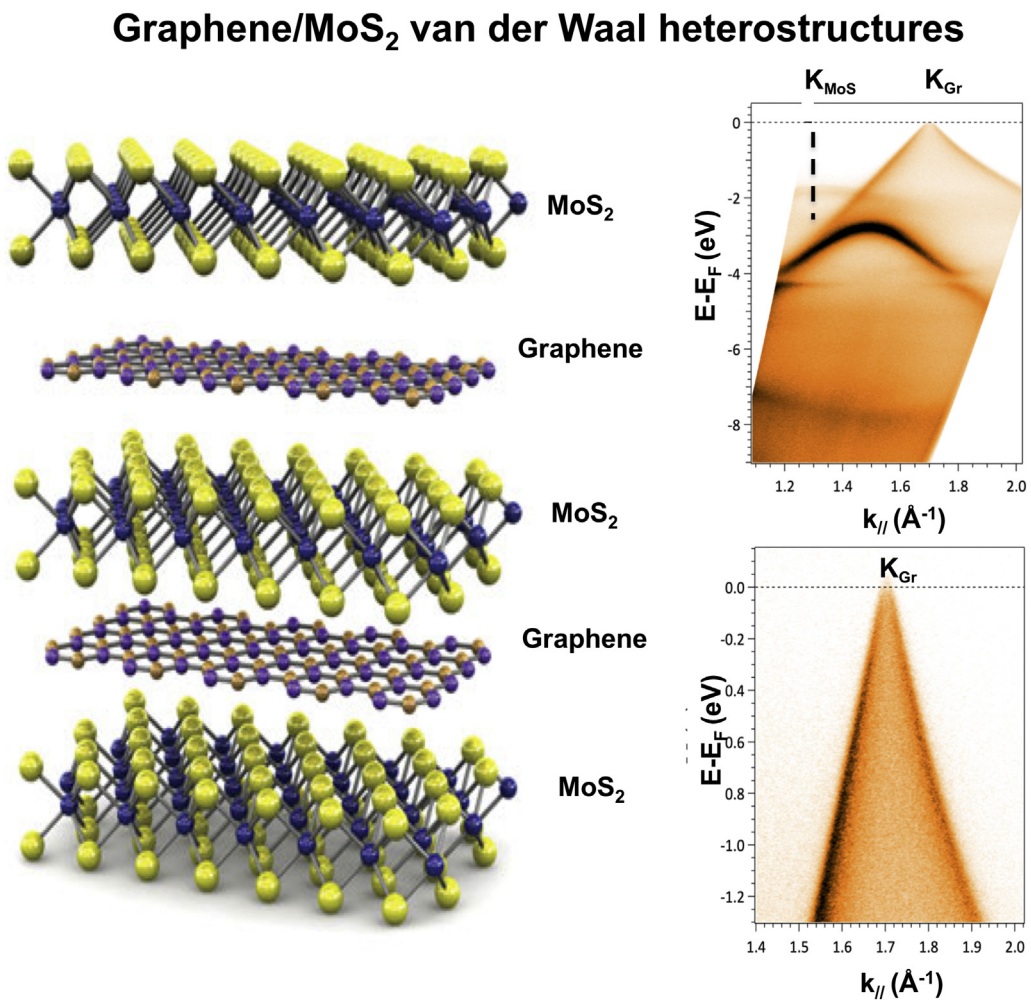

Fig. 10. Artificial heterostructures. The Dirac cone of the graphene transferred on the MoS_2 as measured by nanoARPES. The top right panel shows the upper valence bands of MoS_2 covered by one layer of graphene.

have generated a strong interest for its hypothetical silicon counterpart coined "silicene," or the phosphorous equivalent "phosphorene," that are a one-atom thick silicon or phosphorous sheet arranged in a honeycomb lattice, respectively (see Fig. 12). Theory predicts freestanding silicene sheets and ribbons to be stable either in a flat or in a low puckered configuration. In both cases they would present basically the same electronic properties of graphene. The predicted electronic structure of silicene presents π and π* bands, which form Dirac cones at the Brillouin zone corners. Consequently, as in graphene, the charge carriers in silicene behave as massless relativistic particles. Therefore, all graphene expectations, such as high-speed electronic nanometric devices based on ballistic transport at room temperature, can be transferred to this innovative material with the crucial advantage of easily fitting into the silicon-based electronics industry. The electronic properties of silicene are a hallmark of this promising material has been theoretically predicted and measured using ARPES. However, regarding full interpretation of the experimental results of these types of 2D materials results using different theoretic approaches is still under active debate [23,29].

6.5. Nanomechanical systems for microelectronic

Microelectromechanical (MEMS) and Nanoelectromechanical systems (NEMS) are drawing interest from both technical and scientific communities because of their large versatility. Due to their small size, they have extremely small mass, very high force sensitivity and extremely high resonance frequencies with high quality factors, much higher than in any equivalent electrical circuit. Consequently, these attributes make NEMS suitable for a multitude of technological applications such as ultrafast sensors, actuators and signal processing components. The spectroscopic imaging techniques presented here are particularly useful to face many of the challenging issues related to the realization and optimization of MEMS and NEMS. In effect, nano-chemical and electronic imaging of these pattered devices using nanoCL and nanoARPES can address migration, diffusion, corrosion in contact points, and many other aspects that are critical determining the stability and performance of advanced devices.

6.6. Correlated systems and superconductivity

Central to many current questions in condensed matter, the correlations induced by electronic interactions give rise to numerous exotic materials properties, which become more relevant when the dimensionality is low. Certainly, 2D electron gases at oxide surfaces as $SrTiO_3$ are typical examples of correlation effects manifested under particular conditions at the surfaces of massive crystals. Many experimental ARPES and nanoARPES determinations together, followed by theoretical studies, address the properties of strongly correlated electron systems and the new states induced by correlations: heavy-fermion compounds, non-conventional superconductors, topological insulators, low dimensional systems, charge-ordered systems, doped diamond and doped silicon, etc. Furthermore, relevant goals are associated with

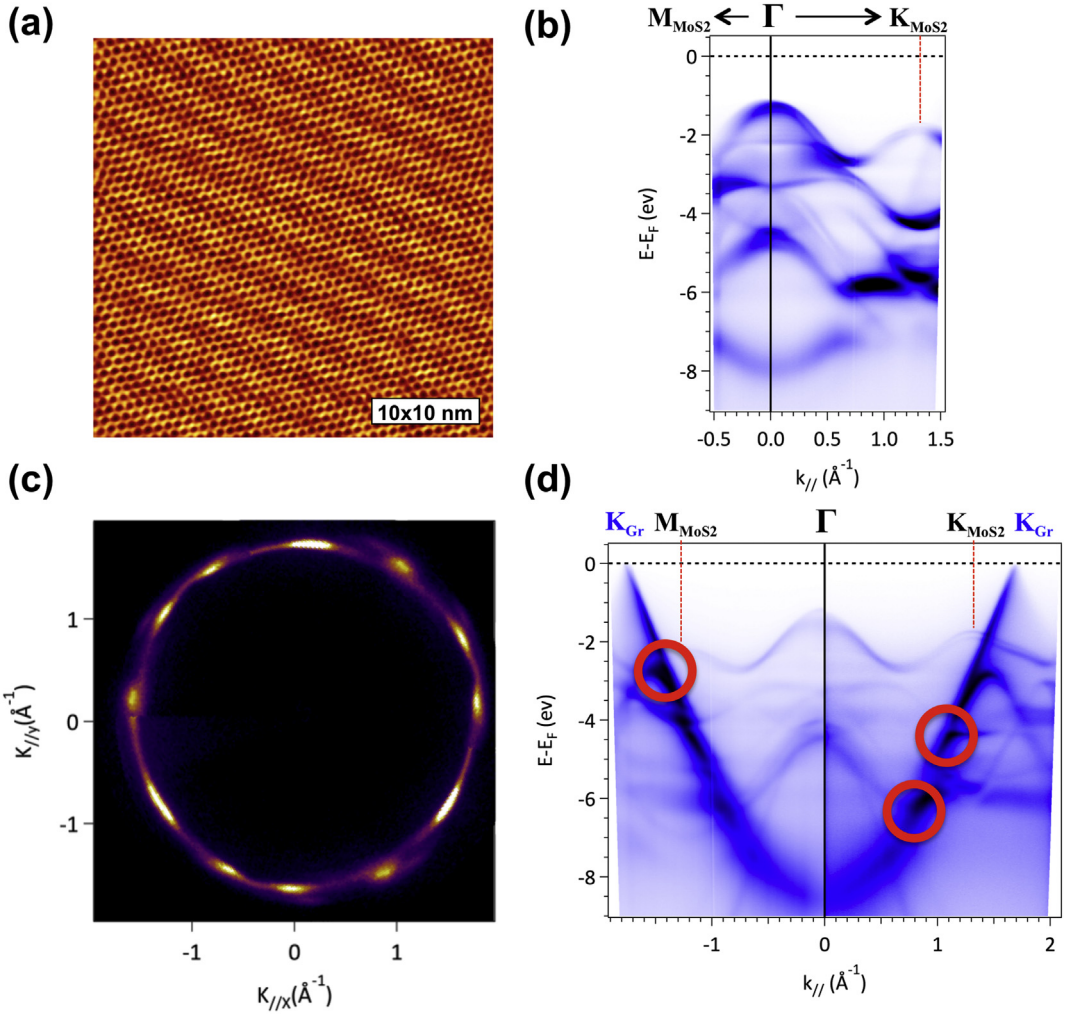

Fig. 11. Artificial heterostructure of graphene on MoS_2 single crystals (a) STM image of the surface of the heterostructure, (b) the Fermi surface showing that the graphene states at the K point of the reciprocal space of graphene determine the states at the Fermi level. Moreover, the symmetry of the Fermi surface topology indicates that the graphene layer is composed of islands of different orientation. Panels (c) and (d) show the electronic structure of a MoS_2 single crystal and graphene/MoS_2 heterostructure, respectively. Reproduced with permission from Ref. [27].

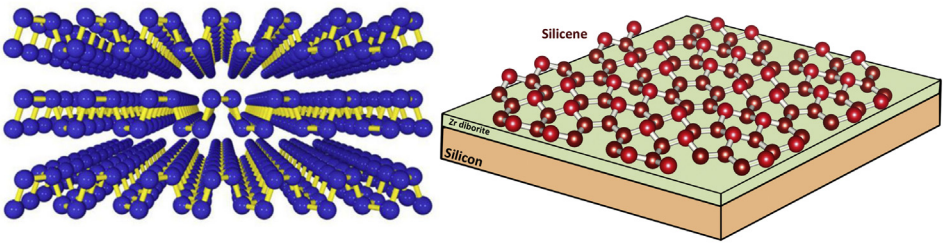

Fig. 12. Left panel shows a diagram of the recently discovered phosphorene structure similar to graphene. Right panel illustrates a typical representation of the silicene grown on $ZrBr_2(0001)$.

understanding of the coupling between magnetic and electronic instabilities and the influence of disorder and confinement on the electronic structure. Fundamental research on the mechanisms of superconductivity is a major strength of many academic surface science research laboratories. A major concern is non-conventional superconductivity and the role of disorder and defects at the surface and bulk as well as the origin of orbital currents related to the symmetry of the order parameter.

6.7. Nanostructures for energy

Electricity offers flexibility, efficiency, and easy end-usage, while avoiding carbon emissions at the industrial or domestic appliance level. An improved control and management of electricity is needed to increase the efficiency and reliability of societies. The breakthroughs that can be expected are linked to progress in materials for its production, transport conversion, and energy storage, where energy storage remains the weakest link. The main strategies developed by the surface science community aims at overcoming new technological barriers by designing components, devices and systems which exploit physical

principles and novel materials. The innovative synergy involves technological advances developed by academics and industrial partners, through the auspices of national and international funding agencies. In the domain of nano-photonics for energy, nanotechnology provides a key to boost the performance of light conversion, with nanoparticles and nanostructures improving both collection and conversion, together with providing better thermal storage and transport. They open new paths for a variety of applications including energy generation and harvesting, lasers and light emitting diodes (LED) [30,31].

6.8. Nanostructures for biological systems

Measuring, manipulating and modifying cells are the three pillars of the bio-physics activity in many laboratories. Collaboration among chemistry, biology and physical research is required for the development of a wide variety of projects. By developing original tools and studying problems, the aim of this research is to tackle fundamental issues in biology and biophysics. This multidisciplinary research carried out at many laboratories is just starting to be developed. Even if this field is quite varied, the primary interest has been shown to be centered on the interaction of nanoparticles and pharmacological drugs with living matter [32,33]. One aspect of this activity is dedicated to the development of new imaging of nanoparticles before and after being built into different biomaterials [34,35]. The emergence of this domain of research has been made possible by existing skills in chemical imaging, in material sciences, and chemistry and surface science research. For instance, the development of ambient pressure photoemission (APPES) can overcome the problem related to preparation of nanoparticles solutions, thus reducing artifacts and providing information on surface chemistry of bio-nanomaterials in almost *real* conditions [36–38]. All these developments strongly benefit from each other to build a multidisciplinary approach to study fundamental issues in biology such as cell thermodynamics, cell mechanics or neuronal communication.

6.9. Perspectives in surface science research

The current research in surface science is moving out of laboratories, increasing its influence in industries ensuring stronger and more stable materials. Many surface science goals are merely viewed as a way to make stronger and lighter planes, racing bikes, intelligent clothing, and many others applications. But the future of surface science promises to do so much more. A more realistic view is that it will leave virtually no aspect of life untouched and is expected to result in widespread use by 2025. Mass applications are likely to have great impact particularly in industry, medicine, new computing systems, and sustainability. The next generation 2D materials like graphene, silicene and others will lead to even lighter, but stronger structures than has been made possible by carbon fibers and will be used increasingly in many new products, which need close and precise surface science characterization. One big challenge is how to produce advanced materials, making them affordable by easily controlling their production and stability. The only way to obtain this goal is by knowing the atomic structure and mechanisms at the surface and their differences with respect to the corresponding bulk material properties. This new knowledge will impact grand challenge problems such as food, water, energy, and environment. Consequently, it is certain that these new areas of research with be enabled by the activity in surface science field [39].

7. Probing nanostructured materials by scanning probe microscopies

For over three decades, nanometer-sized structures have played an enormous role in cutting-edge developments in the natural sciences as well as a central role in exciting new technologies. The dominance of this field can be linked to a few seminal developments: The emergence of scanning tunneling microscopy (STM) and its successor atomic-force microscopy (AFM) as well as other scanning probe microscopies (SPM) in the 1980s allowed atomic-scale imaging as well as probing of a variety of physical properties on the nanometer scale and targeted manipulation of individual atoms. Nearly concurrently, the definitive identification and controlled synthesis of small and low-dimensional entities – fullerenes ($C_{60,}$ mid 1980s), carbon nanotubes (CNT, 1990s), and graphene (Gr, 2000s) – led to their exploitation in a flurry of activity. Still, SPM and low-dimensional carbon structures or their inorganic analogs can be considered as the two fundamentals of nanoscience which – frequently in combination with each other – drive emerging technologies. In the following, we will present a selection of recent SPM achievements on imaging and manipulation at the atomic scale, photoelectrical characterization on the nanometer scale, and studies of graphene supported nanostructures. Finally, we demonstrate how nanoscience is even entering research and applications in long-established, “old” industries like petroleum engineering or paper manufacturing.

7.1. SPM on the atomic and molecular scale

Starting with the pioneering work by Eigler et al. in 1990 [40], SPM has been used in countless cases to manipulate single atoms, demonstrating the potential for SPM-based data storage. Liquid helium temperatures, ultra-high vacuum (UHV), and very long fabrication/readout times have prevented realistic applications so far. Fig. 13 demonstrates

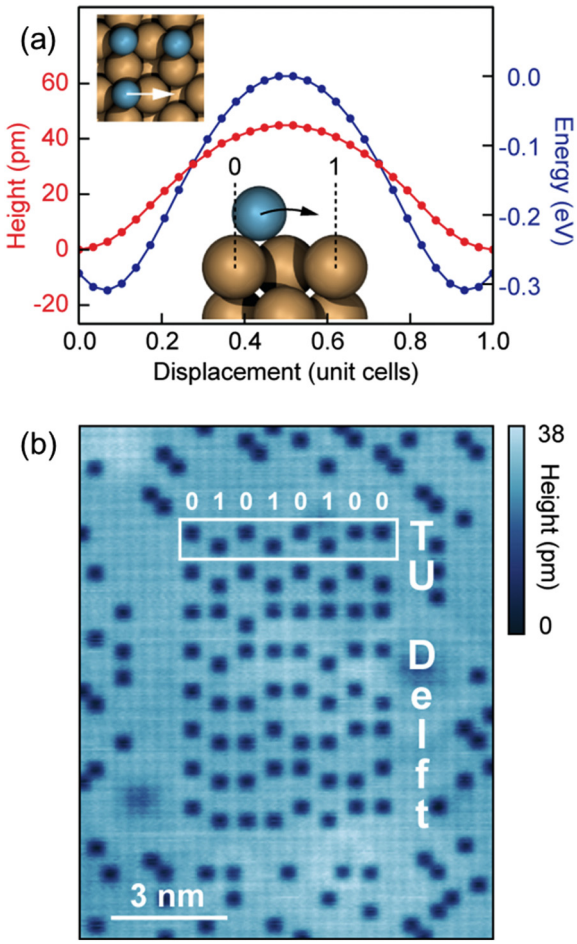

Fig. 13. (a) Height pathway and corresponding potential energy diagram obtained by DFT for a Cl atom jump into a vacancy of Cl (2 × 2) overlayer on Cu (100). (b) STM image of 8 written bytes illustrating the data encoding principle using ASCII code. The vacancies appear dark. Adapted from Ref. [41].

that these limitations can be – at least partly – overcome utilizing an automatized algorithm of STM-based manipulation of vacancies in a c (2 × 2) reconstructed chlorine over-layer on a Cu(001) surface [41]. Density functional theory (DFT) calculations (Fig. 13(a)) reveal that an energy of 0.3 eV is needed to move a Cl atom to a vacancy in the superstructure. Automated STM-manipulation allows controlled movement over this barrier to efficiently move the vacancies for data storage (Fig. 13(b)). Thus, larger data patterns, stable to 77 K are produced while enabling enhanced reading speeds. The procedure results in a record-high areal storage density of about 3000 Tbits/cm^2.

Besides pushing atoms around on surfaces, the STM tip can sort different molecules and even induce and/or probe chemical reactions at the molecular level. STM-assisted manipulation of left- and right handed chiral molecules enabled the performance of an experiment at the nanoscale first shown macroscopically by Pasteur in the 19th century [42]. These experiments required resolution showing the molecular internal structure to identify the chirality of the molecules. There, fine control of molecular interactions was exploited to image and manipulate the molecules: helical molecules could be pulled apart or pushed together using an H-modified STM tip. This tip does not attract the surface molecules strongly and thus allows application of repulsive forces for the manipulations. However, the modified tip degraded the resolution due to convolution effects. Upon removal of the H atom, high-resolution images were obtained, providing a clear view of the chiral structures. It was shown that molecules of opposite chirality bind one-another, while those of identical chirality do not. In the context of the 2016 Nobel Prize in Chemistry for the design and synthesis of molecular machines, it should be noted that the STM can induce conformational changes (i.e., tune the chirality) of the four rotors in car-like, rotary molecular machines through inelastic electron tunneling, thus propelling the molecule unidirectionally across a surface [43].

Ultra-high resolution non-contact AFM with carbon monoxide functionalized probe tips (Fig. 14(a) continues to provide structural insights into organic molecules and their reactions. Fig. 14(b–d) present beautiful, high-resolution images of 2D polycyclic aromatic hydrocarbon molecules, revealing clearly the individual carbon-carbon bond-order [44]. Combining such exquisite images with careful experiment design also allows investigating reactions in real-time. A carefully designed ultrathin insulating substrate allowed stabilization and imaging of an elusive reaction intermediate (aryne) in the dehalogenation of polyaromatic halides [45].

In addition to imaging and manipulation of atoms and molecules, SPM techniques enable detection of physical properties at the nanometer scale. For instance, spin-polarized STM operating in UHV at low temperatures with external magnetic fields reveals magnetism at the atomic scale as has been recently demonstrated for the long-range magnetic coupling between organic–metal hybrids mediated by a nanoskyrmion lattice of an Fe monolayer on Ir(111). There, the magnetization vectors of the individual Fe atoms could be resolved individually as well as the magnetic coupling of the organic-ferromagnetic units [46].

7.2. SPM based photoelectrical characterization of semiconductor nanostructures

The power of SPM-based characterization lies largely in the power to acquire multi-faceted insights into the physical properties of nanostructures including electrical, optical, magnetic, mechanical, and thermal properties. Furthermore, combined effects like piezoelectricity – via piezoresponse force microscopy – or photoconductivity – via photoconductive atomic-force microscopy (PC-AFM) or photo-assisted Kelvin probe force microscopy (PA-KPFM) – are now widely applied. One example of this is the recent efforts to measure photocurrents of lying-down and upright semiconductor nanowires (NWs) for photovoltaic applications. Gallium oxide flakes and gallium oxide wires on Kapton substrates were irradiated with charged particles and UV light, and the resulting current collected using silver ink for contacts [47]. In-situ results obtained for radiation induced conductivity (RIC), as persistent photoconductivity (PPC) and persistent ion-conductivity (PIC), suggest that defects created during the irradiation modify the electrical properties. Moreover, a correlation between the density of defects and optical properties was demonstrated [47].

Real-time detection of photo-response by SPM requires simultaneous irradiation of the nanostructures during electrical characterization with conductive AFM (C-AFM) or Kelvin probe force microscopy (KPFM). For opaque samples, the nanostructures have to be illuminated either from the side or – when using special probes with the tip optically accessible at the very end of the cantilever – from the top via the illumination system of the optical microscope of the SPM [48]. A particularly challenging example is photoconductive AFM inspection – which requires contact mode measurement – of delicate samples such as vertically aligned NWs, without breaking them. For ZnO NWs, persistent photoconductivity – after switching off the light source – can be observed. In addition, current voltage curves under irradiation by monochromatic light revealed photocurrent excitation at only 3.1 eV photon energy; which is at least 100 meV lower than the band-gap energy determined from photoluminescence experiments [48] suggesting that the observed photo-response originates preferentially from photo-excitation of charge carriers localized at defect states. In Fig. 15, PA-KPFM results of Si NW based radial junction (RJ) solar cells are summarized. Fig. 15(a) illustrates the structure of these NWs (for details see Ref. [49]). Fig. 15(b–d) presents topography and corresponding PA-KPFM under illumination and in the dark. Analysis of these data revealed that the surface potential shift due to orange-light (592 nm) illumination increased from about 40 mV to 50 mV as the NW height increased from 700 nm to 1.4 μm [49].

SPM techniques also allow the study of complex molecular mechanisms of bio-molecules. Although principles and importance of

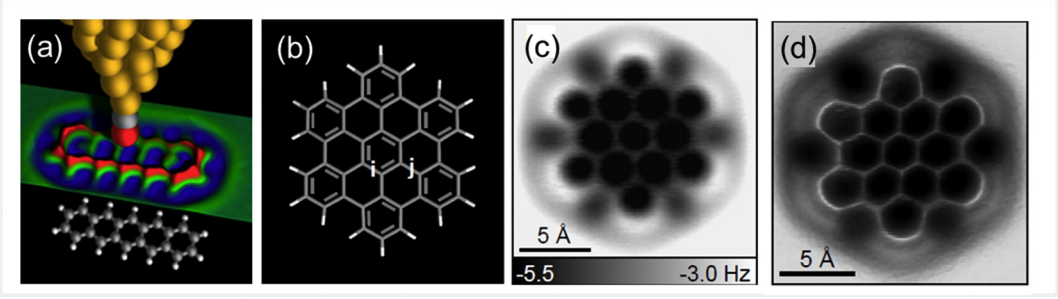

Fig. 14. (a) Scheme of sub-molecular resolution, noncontact imaging of pentacene (molecular model in the bottom) by a CO-functionalized AFM tip [44]. The oxygen atom is facing the molecule. (b)–(d) Bond-order discrimination of hexabenzocoronene using the functionalized tip presented in (a). Molecular model of hexabenzocoronene (b). Constant-height AFM images at 0.37 nm and 0.35 nm, respectively (c, d). The bonds denoted by "*i*" are of larger bond order and appear brighter (c) and shorter (d) in the AFM images than the bonds denoted by "*j*" (for details see Ref. [44]). Figure adapted from Ref. [44].

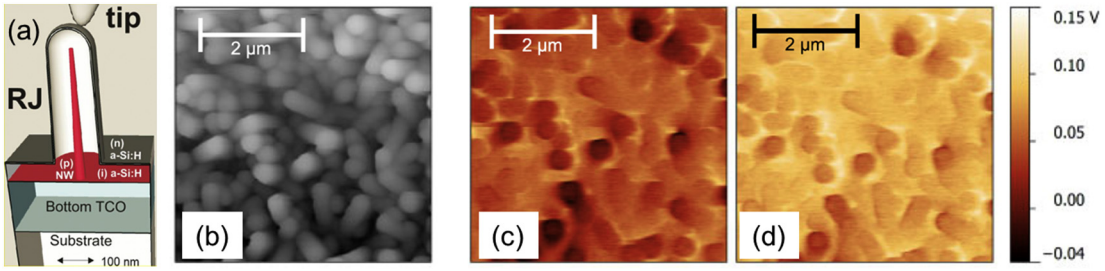

Fig. 15. (a) Scheme of inspecting by KPFM an upright standing radial junction Si solar cell composed of a 10 nm diameter crystalline Si NW in the center surrounded by a 40 nm thick amorphous Si-H layer followed by a few nanometer thick heavily n-doped amorphous Si-H layer [49]. (b) Topography of RJ solar cell shown as height signal of the AFM (z-scale: 2 μm). (c) Corresponding surface potential signals under illumination by orange light (592 nm) and (d) in darkness. Figure adapted from Ref. [49].

electron and charge-transport in proteins are well known, only recently have nanoscale measurements allowed probing this activity at the (sub) molecular level. The membrane protein Bacteriorhodopsin (BR) has the unique capability to utilize visible light to pump protons across the cell membrane. This is done by initial absorption of green light by the chromophore retinal (embedded in the heart of the protein), leading to a series of intermediate states culminating in the proton transfer. Interestingly, electrons are transported in similar fashion across this protein [50]. This activity is highly sensitive to environmental conditions such as pressure, humidity, and, of course, light. Fig. 16 shows the effective low-voltage resistance of BR molecules as a function of pressure applied by the probe. Two pressure regimes are observed: a low-force regime of high slope with reversible behavior and a higher-force regime of low slope with irreversible behavior. A strong dependence on green light was observed at the lower, but not the higher pressures. The calculated pressure at the transition force corresponds to pressure required to reconfigure the hydration shell of the molecule, implicating the role of water in electron conduction. Experiments at varying humidity verified this conjecture.

7.3. Two-dimensional materials and nanostructures thereon

The ground breaking experiments on Gr by Geim and Novoselov initiated a boom on research of similar 2D materials that can either be peeled off from the > 3000 existing layered bulk (van der Waals—vdW) materials or can be grown exclusively on solid surfaces [51]. There are now at least four families of these vdW materials (graphene family including silicene, germanene, stanene, and hexagonal boron nitride (hBN); black phosphorous family; transition metal dichalcogenides; and III-V 2D materials) which cover the entire range of electric conductivity from insulators, via semiconductors, semimetals, and metals to superconductors which can be stacked on top of each other forming hybrids [52]. As an example of such - until recently - completely unknown or neglected materials, a 2D hafnium layer (hafnene) prepared in UHV on an Ir(111) surface [53] is presented in Fig. 17. STM and low-energy electron diffraction (LEED) (Fig. 17(a)) as well as DFT calculations (Fig. 17(b–d)) clearly reveal the honeycomb lattice with directional bonding between adjacent Hf atoms analogous to carbon-carbon bonds in graphene [53]. Moreover, band structure calculations predict ferromagnetism for a free-standing hafnene layer making such transition metal honeycomb layers interesting objects broadening the scope of 2D materials [53].

Tailoring the physical properties of 2D materials by nanostructuring is a recent and strong research field where ion irradiation is frequently employed. In the following, an example of nanostructure formation by Xe^+ irradiation of Ir(111) supported Gr is presented [54]. Fig. 18 shows STM and LEED results of Gr/Ir(111) bombarded with 500 eV Xe^+ under normal incidence at room temperature and at subsequent annealing steps in UHV. After ion irradiation, the sample surface shows a rather damaged Gr sheet with small protrusions of 0.3 to 0.5 nm height (Fig. 18(a)). The protrusions are mainly assigned to Xe atoms trapped under the Gr [54]. Upon annealing to 1000 K, most of these protrusions disappear and flat bulges of 0.35 nm height appear, as well as taller, curved blisters (see cross-section in Fig. 18(b)). Also, vacancy islands (dark in the STM topography) are present. The flat bulges are due to monolayer Xe platelets that form at the interface between Gr and Ir. When these bulges grow larger they transform into blisters. After annealing to 1300 K, fewer but larger blisters remain – trapping high-pressure Xe nanostructures underneath – (Fig. 18(c)). The remaining flat areas show an intact Gr film with characteristic moiré pattern (inset in the STM image of Fig. 18(c)). These blisters might enable confined reactions in pressurized nanocavities [54].

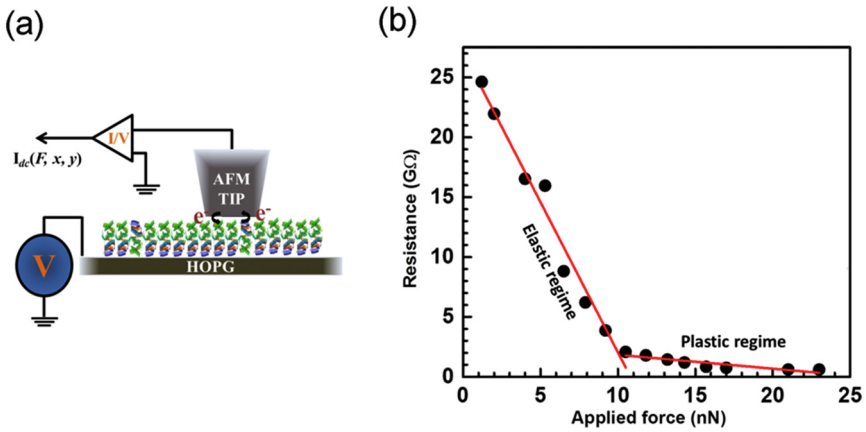

Fig. 16. (a) Experimental scheme for measuring conductance of the BR molecules by C-AFM. (b) Dependence of low-voltage current on the applied normal force. Reprinted with permission (Ref. [50]), 2014, American Chemical Society.

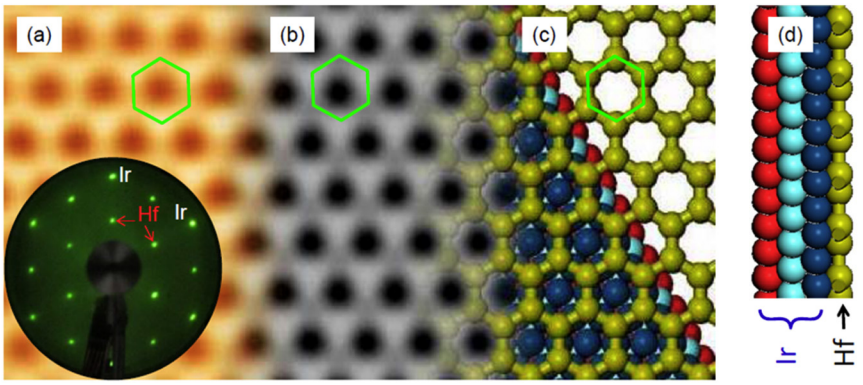

Fig. 17. (a) Atomically resolved experimental STM image (−1.5 V, 0.1 nA) and corresponding LEED pattern obtained at 70 eV electron energy showing a (2 × 2) superstructure of Hf deposited at room temperature on Ir(111) after subsequent annealing at 673 K. (b) Simulated STM image (−1.5 V) using the DFT results for a planar Hf layer on three Ir(111) layers presented in (c) as top view and (d) as side view. The Hf honeycomb is highlighted in (a–c) by a green hexagon. Figure adapted from Ref. [53].

Finally, it should be stated that 2D materials boast the attractive possibility to host arrays of multi-component nanostructures. One useful example is the technologically important role of graphene as a transparent and conductive electrode where the flexibility of Gr comes into play. For cases such as the growth of aromatic rod-like molecules like oligophenylenes and acenes, one can expect that the molecules grow with their long axis parallel to the Gr substrate. When these molecules form the active component in organic solar cells or organic light-emitting diodes, this would be the desired molecular orientation to enable charge carrier transport perpendicular to the electrode surfaces. For the model molecule para-hexaphenyl (6P) on differently prepared Gr substrates, it has been demonstrated that crystalline nanoneedles composed of molecules parallel to the surface can be grown [55]. Fig. 19 displays such Gr-6P constructs: In Fig. 19(a), for 6P grown at 363 K on exfoliated Gr flakes transferred to silicon oxide, needles a few tens of nm high and < 100 nm wide are formed, with lengths extending to over several μm. These needles are predominantly straight and follow preferential directions as is shown in Fig. 19(b) for a larger ensemble of needles. The discrete relative orientation angles between needles of mainly 60°, but also 23°, 30°, and 90° can be related to the crystallography of the Gr substrate [55]. Sometimes, the needles appear curved (white arrows in Fig. 19(a)), however, this is due to the formation of chains of short, straight segments expressing the different possible orientations. Besides electrically conductive Gr, using insulating, ultrathin hBN as a substrate for organic semiconductor molecules offers the possibility of realizing a flexible dielectric for organic field-effect transistors. Fig. 19(c, d) demonstrates that well oriented, straight 6P nanoneedles also grow on mechanically exfoliated hBN flakes, where the formation of a (−629) contact plane with hBN results in a ± 5° deviation of the needle axis from the zigzag-directions of the hBN substrate [56].

7.4. Nanoscience providing new insights into old industries

Finally, examples are presented how modern nanoscience can yield fundamental new insights in well-established large-scale industries. Closing the circle with atomic-resolution SPM imaging mentioned in the beginning of this section, we first refer to molecular structure investigations of asphaltenes in crude oil or of coal-derived ones [57]. A combination of AFM and molecular orbital imaging by STM revealed the molecular structures of 100 different asphaltene molecules. The technique can allow characterizing and identifying the formation process of an economically important raw material. A similarly important raw material is bitumen, a byproduct of crude oil refining and extensively used, e.g., as the binding agent in asphalt concrete for road construction. Fig. 20 presents an example of how AFM based adhesion measurements can provide a link between chemical and mechanical properties of bitumen [58]. The AFM image in Fig. 20(a) reveals the topography of a solution-cast sample of a specific asphalt binder which consists of two different domains having micrometer dimensions with a slight height difference. Force-distance curves of these two domain types (Fig. 20(b)) revealed higher adhesion forces (lowest point of the retraction curves), higher maximum attractive forces (lowest point of the approaching curves), and higher dissipated energy (hysteresis between approach and retraction) for raised areas compared to that of the recessed ones. The combination of such adhesion measurements with other AFM testing methods can provide molecular insights into the binding properties of bitumen and related petroleum products.

Fig. 21 demonstrates another application of AFM-based force-distance curves; here to determine the binding strength in joints of individual cellulose fibers [59] which form the fundamental contribution to the strength of the natural product paper, which has been used by mankind for millennia. The technique (Fig. 21(a)) – in conjunction with

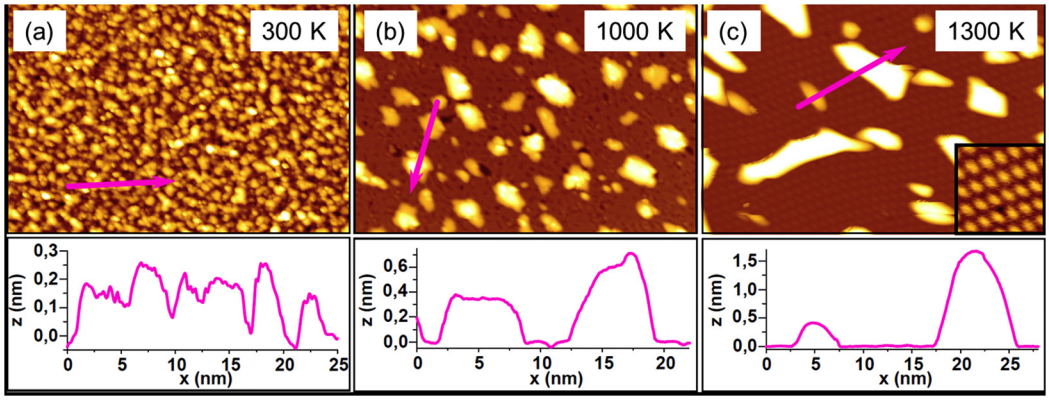

Fig. 18. (a) 60 nm × 90 nm STM topographies of 500 eV Xe^+ irradiated Gr/Ir(111) at room temperature, and after subsequently annealing to (b) 1000 K and (c) 1300 K. Inset in (c): High-resolution image of the intact Gr. In the bottom panel, corresponding height profiles along the arrows indicated in the topographies are shown. Figure adapted from Ref. [54].

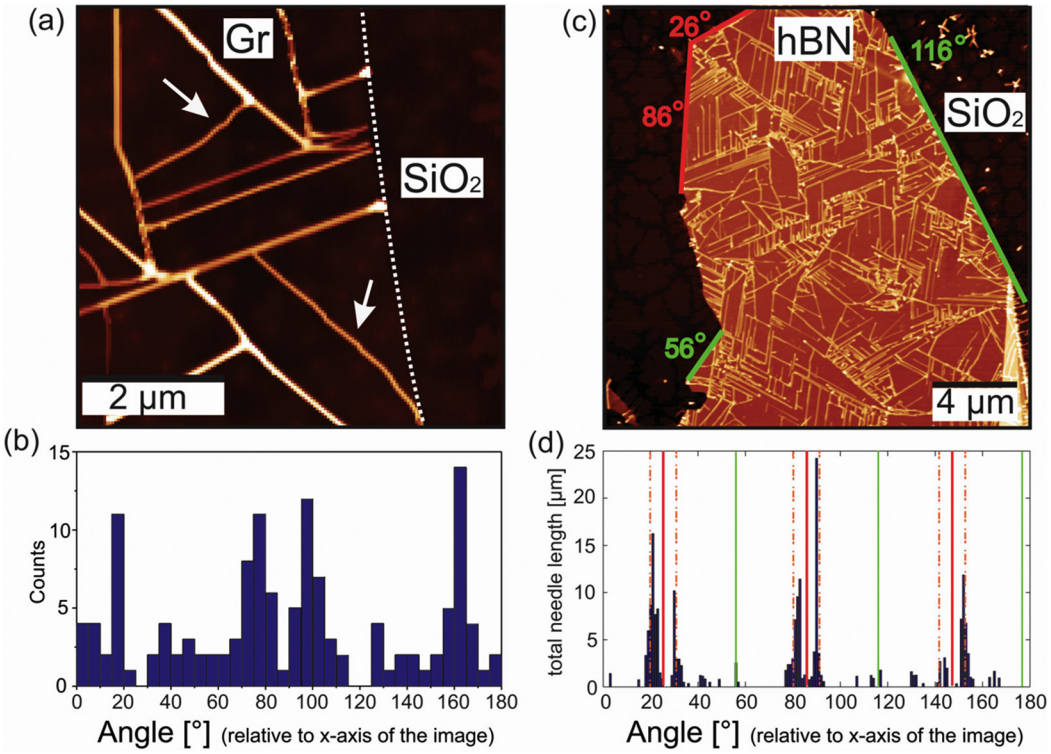

Fig. 19. (a) 5 μm × 5 μm AFM image of 6P deposited by hot-wall epitaxy (HWE) at 363 K onto exfoliated single-layer Gr/SiO_2. z-scale: 40 nm. 6P needles grow only on top of Gr and terminate the edge of the Gr flake which is indicated by the dashed line. (b) Corresponding distribution of the needle orientation with respect to the x-axis of the image (0°) for 6P needles grown on Gr. [49] (c) 20 μm × 20 μm of 6P HWE deposited at 363 K on an 18 nm thick exfoliated hBN flake on SiO_2 and (d) corresponding total needle length distribution. The red lines in (c, d) mark zigzag and armchair directions of the hBN, respectively. Figure adapted from Ref. [56].

AFM inspection of the formerly bonded area of the fibers after rupture (Fig. 21(b)) – clearly showed that the increased binding strength in paper made from refined pulp is mainly due to mechanical interlocking of dangling fibrils and fibril bundles (Fig. 21(c–d)) [60]. These findings obtained by modern scanning probe techniques therefore contribute to improvements in the strength of packaging paper in a 400 Mt per year global industry, with simultaneous decrease in energy input and environmental impact.

8. Surface engineering

Surface Engineering (SE) is the science and technology of improving the surface properties of materials for protection in demanding contact conditions and aggressive environments. SE also encompasses engineering new multi-functional surface properties, such as electrical, optical, thermal, chemical, and biochemical properties. It involves multiple or hybrid processes which include substrate modification and deposition of overlayers in complex architectures. These processes

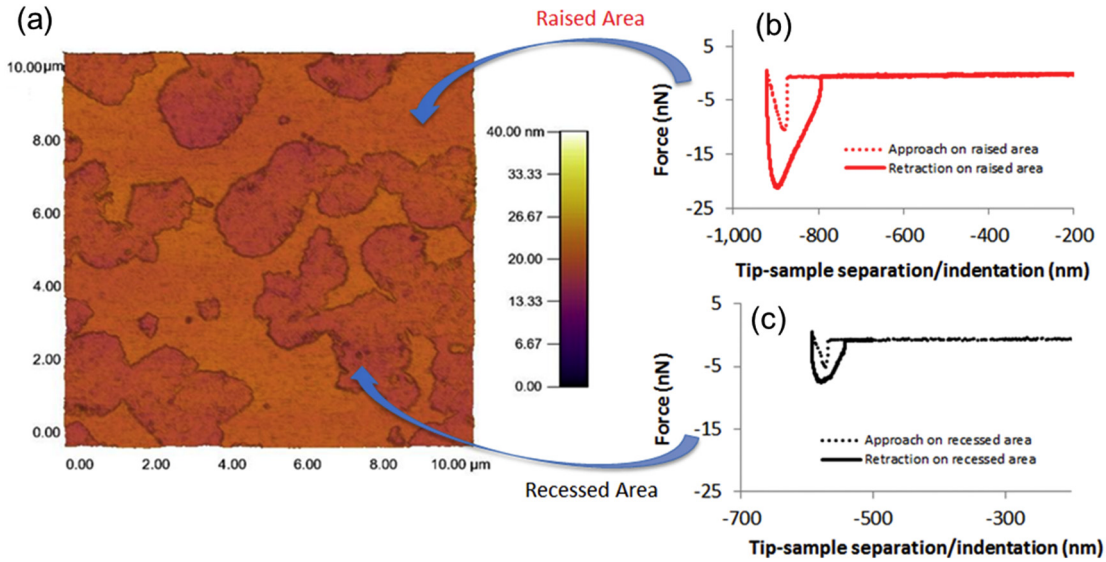

Fig. 20. (a) Topography image of an asphalt binder showing micrometer sized raised and recessed areas. (b) Approach (dotted line) and retraction (solid line) force vs. separation curves acquired on raised areas of the topographic image as shown in (a). (c) Corresponding force-distance curve recorded on a recessed area. Figure adapted from Ref. [58].

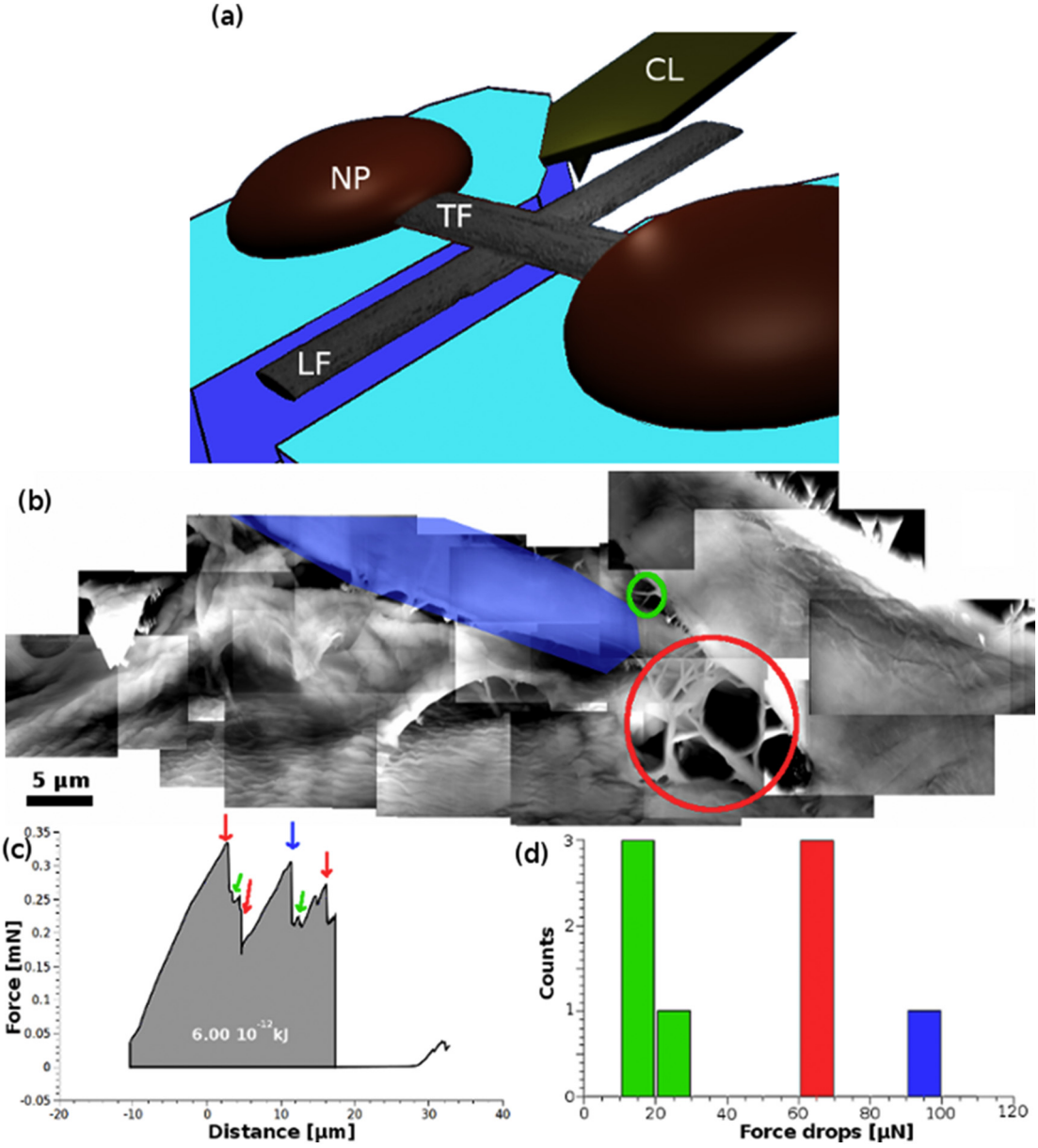

Fig. 21. (a) Principle of an AFM based joint strength measurement between single cellulose fibers in paper [59]: A stiff cantilever is approached near the joint to rupture the dangling lower fiber (LF) from the top fiber (TF) which is fixed by nail polish (NP). (b) AFM topography image reconstruction of the formerly bonded area of a fiber-fiber fiber joint from 2000 revolutions refined pulp. Circles denote single fibrils (green) and fibril bundles (red). The blue shaded area marks a delaminated cell wall [60]. (c) Corresponding force-distance curve of the ruptured bond shown in (b) representing the different strong force discontinuities that originate from interlocked fibrils (small force drops, green) and fibril bundles (intermediate force drops, red) as well as from cell delamination (large, blue). (d) Classification of force drops observed in (c). The observed events correlate to the number of bridging elements found in (b). Figure adapted from Ref. [59]. (For interpretation of the references to color in this figure legend, the reader is referred to the web version of this article.)

enhance adhesion and optimize composition or microstructure to enhance protective properties coupled with other functionality. The substrates may be of complex shapes, like metal-cutting tools and automotive or aerospace components, and range in size from micrometers, such as in MEMS or NEMS (micro- or nano-electromechanical systems) devices, to meters, such as in architectural glass. The applications are wide-ranging, and include, for example, control of friction, wear-resistance, corrosion-resistance, thermal-barrier coatings, decorative coatings, bioimplants, antimicrobial layers, web-coatings, and thin films with engineered electrical and optical responses. Areas of scientific interest range from first-principle atomistic studies of new materials, which are both hard and ductile, (i.e., tough), to scientific and technological advances in synthesis methods, structural and chemical characterization techniques, property measurements, and performance characterization of surface-engineered parts. Here, we highlight a few selected SE advances from the past three years.

Alling et al. [61] performed a screening study of the mixing thermodynamics and age-hardening potential of 45 $M^{1}_{(1-x)}M_{2x}B_2$ alloys with components $M^{i}B_2$ (M^{i} = Mg, Al, Sc, Y, Ti, Zr, Hf, V, Nb, and Ta). All alloys have the AlB_2 type structure. The mixing trends are explained based upon analysis of the volume misfit of the two components $M^{1}B_2$ and $M^{2}B_2$ and the electronic structure analysis of selected model system. The authors conclude that metastable $Al_{1-x}Ti_xB_2$ alloys have a strong thermodynamic driving force for isostructural clustering combined with a small lattice mismatch and a high bulk modulus. The combination of properties qualifies them for thin film age hardening applications, i.e. increased hardness at elevated temperature. Over-stoichiometric $Al_{0.29}Ti_{0.71}B_3$ nanostructures have been deposited by

magnetron sputtering and exhibit an increase in hardness from 32 GPa in the as-deposited state to 37 GPa after annealing at 1000 °C in vacuum [62].

Bolvardi et al. [63] carried out a systematic ab initio study of the electronic structure and mechanical properties of X_2BC (X = Mo, Ti, V, Zr, Nb, Hf, Ta and W) alloys. The authors report negative formation enthalpy for all compounds with respect to the elements, indicating the possibility of synthesizing them and demonstrate that X_2BC compounds with X = Ta, Mo and W exhibit an unusual combination of high stiffness and moderate ductility and are therefore promising candidates as protective coatings. As the average valence electron concentration (VEC) per atom is increased by substitution of the transition metal (TM) X, the six very strong bonds between the TM and carbon shift to lower energies relative to the Fermi level, thereby increasing the bulk modulus to values of up to 350 GPa, which corresponds to 93% of the value reported for c-BN. Systems with higher VEC appear to be ductile as inferred from both a more positive Cauchy pressure and a larger bulk-to-shear modulus ratio (B/G). The more ductile behavior is a result of the more delocalized interatomic interactions due to larger orbital overlap in smaller unit cells.

After their first report [64] on the high-temperature (900 °C) deposition of Mo_2BC coatings by combinatorial DC magnetron sputtering, the Aachen group developed a low-temperature (380 °C) synthesis process using HIPIMS (high-power impulse magnetron sputtering) [65]. In a recent paper [66], the authors evaluated crack formation in nanocrystalline Mo_2BC coatings deposited on Cu substrates, subjected to uniaxial tensile loading with bench-mark reference coatings of TiAlN, Al_2O_3 and Mo. Films, 3-μm-thick, were deposited by bipolar pulsed magnetron sputtering on Cu foil, 700-μm-thick, with a dog-bone shape (Fig. 22). The samples were deformed to different strain levels and the crack density was determined by scanning electron microscopy; the results are presented in (Fig. 22(b)). The first Mo_2BC cracks are discernable by SEM at tensile strains exceeding 5.4%. For strains of ~11%, the crack densities for coatings of Mo, TiAlN, and Al_2O_3 are 2.5, 5.0 and 1.9 times larger, respectively, than that of Mo_2BC. These results validate the initial DFT calculations where Mo_2BC coatings were predicted to exhibit unusually high stiffness combined with moderately ductile behavior. Hence, these coatings are promising candidates for utilization in cold-forming applications.

Vlček et al. [67] employed reactive gas pulsing to achieve high-rate (hundreds nm/min) HIPIMS of stoichiometric TM oxides. Consequently [68] the authors expanded the technique to achieve unprecedented control over the composition of sputter-deposited TM oxynitrides thus overcoming the difference in reactivity of O_2 and N_2. It was demonstrated [69] that due to the much stronger reactivity of oxygen compared to nitrogen, only a few percent of oxygen in the gas mixture is sufficient to deposit pure oxide films during reactive sputtering of O_2 + N_2 mixtures. Rezek et al. [68] combined the reactive gas pulsing (Fig. 23(a)) with an injection of the reactive gas (O_2 + N_2) into the most intense zone of a HIPIMS discharge (20 mm above the race track, through 1 mm orifices directed to the target; (b). The plasma density was further enhanced by using a short duty cycle of 2.5%. The high degree of dissociation of both O_2 and N_2 results in high reactivity for both atomic O and N. In this way the authors prepared Ta-O-N films of smoothly controlled compositions (Fig. 23(c)) with deposition rates of 97 nm/min to 190 nm/min. Recent investigations have shown that the deposition rate can be further enhanced by orienting the reactive gas inlet to the substrate, up to 120 nm/min (ZrO_2) [70] to 345 nm/min (HfO_2) [71].

It was realized early in the development of HIPIMS [72] that there is a time separation between the Ar-ion and metal-ion-dominated fluxes incident at the substrate which opens the possibility for selecting one or the other components for ion-assisted film growth using a synchronized pulsed bias voltage. Recently, Greczynski et al. systematically explored this approach using pseudobinary TiN-based model systems TiMeN (Me = Al, Si, and Ta). The experiments were carried out in a hybrid configuration with one target powered by HIPIMS, the other operated in DCMS (direct-current magnetron sputtering) [73] mode in order to probe the effects of both metal versus rare-gas ion irradiation and the type of metal ion used (Ti vs Me). The latter was possible due to the large difference in the ionization degree of sputtered flux between DCMS and HIPIMS which allows for selection of metal-ion irradiation in the co-sputtering setup. The authors initially employed the metastable NaCl-structure $Ti_{0.39}Al_{0.61}N$ as a model system to demonstrate that switching from Ar^+ to Al^+ dominated bombardment eliminates phase separation, minimizes renucleation during growth, reduces the high concentration of residual point defects, and thus results in dense, single-phase, essentially stress-free films [74].

For the metastable alloys, TiAlN [75] and TiSiN [76], mechanical properties are shown to be determined by the average metal-ion momentum $\langle p_d \rangle$ transferred per deposited atom. Irradiation with lighter metal-ions (Me = Al^+ or Si^+ during Me-HIPIMS/Ti-DCMS) produces fully-dense single-phase cubic $Ti_{1-x}(Me)_xN$ films with low stresses. In contrast, the use of higher-mass Ti^+/Ti^{2+} yields $\langle p_d \rangle$ values which exceed the threshold necessary for phase segregation even at very low substrate bias values, and results in second-phase w-AlN or a-SiN_x precipitation.

Greczynski et al. [77] demonstrate a new process for obtaining fully-dense refractory ceramic thin films without external substrate heating. Heavy Ta metal-ion bombardment is used to obtain $Ti_{(1-x)}Ta_xN$ layers with high hardness and elastic modulus, and lowered residual stress. Model $Ti_{0.92}Ta_{0.08}N$ alloy films were grown by Ta-HIPIMS/Ti-DCMS at T_s < 120 °C with a bias voltage V_s = 160 V synchronized to the Ta^+/Ta^{2+} portions of the HIPIMS pulses. Because of heavy-metal–ion bombardment, the intercolumnar and intracolumnar porosity, typical of low-temperature refractory ceramic film growth, is eliminated (see Fig. 24) due to efficient near-surface atomic mixing. Film surfaces are smoother and hardness is 330% higher than that for

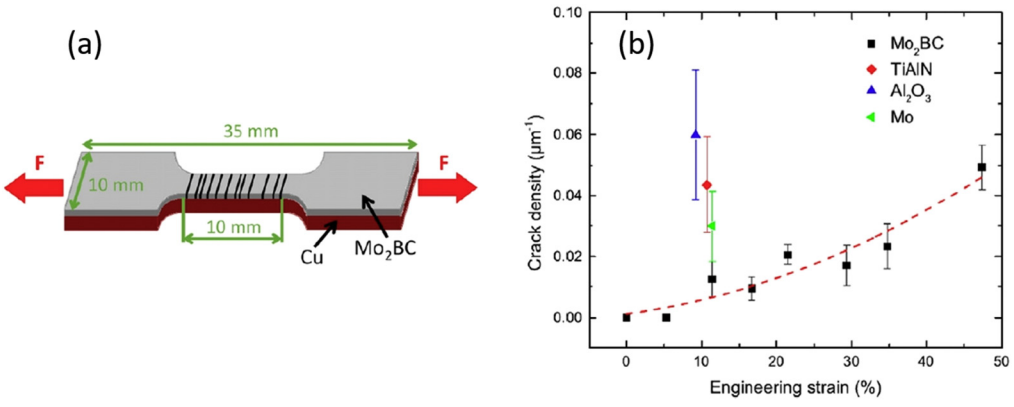

Fig. 22. (a) Schematic of a dog-bone-shaped Cu foil substrate with 3-μm-thick Mo_2BC coating which, after straining to a known level is evaluated by SEM to determine the crack density; (b) Crack density as a function Mo_2BC sample tensile strain compared to crack densities in TiAlN, Al_2O_3, and Mo coatings strained at ~11%. From reference [66].

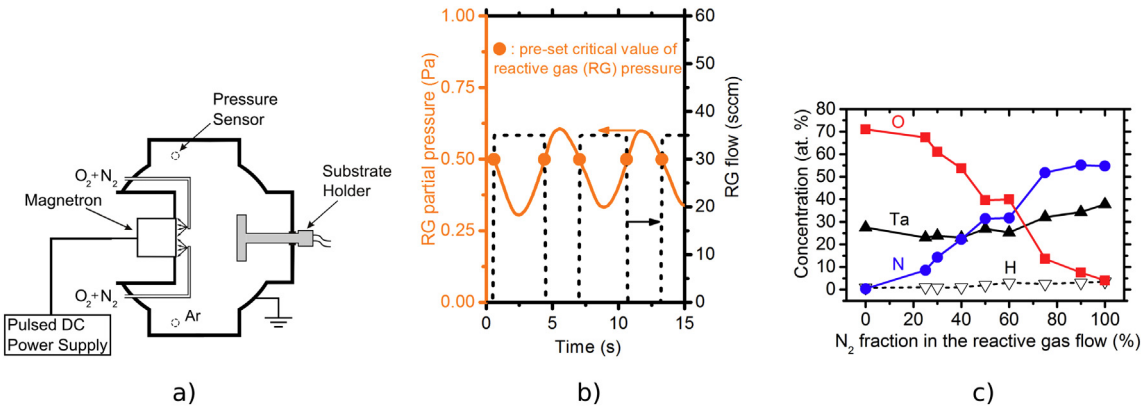

Fig. 23. (a) Schematic diagram of the HIPIMS deposition system with two inlets of reactive gases in front of the target. The positions of the pressure sensor and the Ar inlet in the back side of the vacuum chamber are also shown; (b) Reactive gas (RG) partial pressure (left abscissa) controlling the duration of pulses of the total flow rate (right abscissa) of reactive gases during a reactive sputter deposition of Ta-O-N. The pre-selected critical value of RG partial pressure = 0.5 Pa determining the switching-on or switching-off of the total flow rate of reactive gases of 35 sccm is marked by dots; (c) Elemental composition of Ta-O-N films prepared at various nitrogen fractions in the total flow rate of O_2 + N_2 reactive gas mixture. From reference [68].

reference DCMS TiN (V_s = 10 V) layers, while the residual stress remains low (Fig. 25).

Overall, Greczynski and coworkers demonstrated that using synchronous bias to select the metal-rich portion of the HIPIMS ion flux provides a new dimension for ion-assisted growth in which momentum can be tuned by selection of the metal ion in the hybrid cosputtering configuration and stresses can be reduced or even eliminated, depending on the film growth conditions, since the metal ion is a component of the film.

Recently, a cross-sectional X-ray nanodiffraction technique using a highly focused monochromatic synchrotron beams with a diameter down to 30 nm was introduced [78]. A lamella of the sample with a thickness L of ~10 μm to ~100 μm (Fig. 26) is scanned in cross-section and transmission diffraction data are collected using a two-dimensional (2D) detector. The collected data can be used to evaluate thin film cross-sectional evolution of phases, crystallographic texture, crystallite size and, applying appropriate X-ray elastic constants, also residual stresses [79]. The novel approach serves as an important tool to understand the correlations among cross-sectional thin film microstructure, and residual stresses, and gradients of functional properties on the other side [80]. Additionally, in-situ experiments coupled with indentation can be used to reveal stress concentrations and microstructural changes accompanying fracture [81].

As an illustration, in Fig. 27 we reproduce results from cross-sectional microstructural, chemical and strain analysis on a 2-μm-thick graded $Ti_xAl_{1-x}N$ film prepared using physical vapor deposition (PVD). An XTEM (cross-sectional transmission electron microscopy) micrograph in Fig. 27(a) shows a complex film microstructure film with small crystallites in the near-interface region and two regions with columnar crystallites which are separated by another nucleation zone at a depth of ≈0.6 μm. Quantitative energy-dispersive X-ray spectroscopy (EDS) performed in scanning transmission electron microscopy (STEM) mode shows gradual changes in TiN and AlN film depth concentrations (Fig. 27(b)). Debye-Scherrer rings collected using the 2D detector were used to evaluate radial distribution of diffraction intensity for the azimuthal angle δ range of (−10,10) degrees. A depth-resolved intensity plot in Fig. 27(c) shows a presence of cubic (a) and hexagonal (h) TiAlN phases with a threshold at the Al/Ti ratio of ≈ 0.7 and the depth of ≈ 0.6 μm. The cross-sectional changes in c- and h-TiAlN reflection morphologies correlate well with the film microstructural evolution (Fig. 27(a)). Broadening of c-TiN and h-TiAlN reflections at the depths of 2 and 0.6 μm, respectively, is caused by the presence of two nucleation zones with globular nano-crystallites. The decrease in the full-with of half maxima of the reflections with the increasing distance from the nucleation zones is caused by the formation of elongated V-shape crystallites.

The cross-sectional peak shift originates from the compositional changes (Fig. 27(b)) as well as from the variation of in-plane elastic strains (Fig. 27(d)). Within the two nucleation zones, the compressive strains are relatively high and further decrease as a result of the competitive grain growth.

9. Innovative microspheres for hydrogen storage

Many new aspects of thin film technology result from the need to harvest and store renewable energies. In this respect hydrogen plays a special role as an energy carrier. For decades, people have dreamed of vehicles powered by hydrogen and emitting only water. Depleting fossil fuels and exponentially rising CO_2 emissions also favor this alternative energy carrier [82].

Hydrogen has the highest energy density of all common fuels by weight. The lower heating value of hydrogen is 120 MJ/kg, while

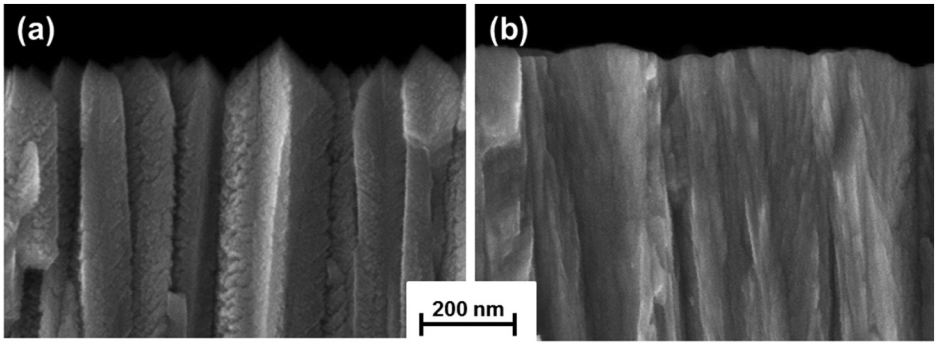

Fig. 24. Cross-sectional SEM images of an area near the top of (a) a 1.95-μm-thick DCMS TiN reference film grown on Si(001) with V_s = 10 V and (b) a 1.85-μm-thick Ta-HIPIMS/Ti-DCMS $Ti_{0.92}Ta_{0.08}N$ alloy layer grown on Si(001) with V_s = 160 V synchronized to the metal-ion-rich portions of HIPIMS pulses. In both cases, there is no external substrate heating (T_s < 120 °C) during film growth. From reference [77].

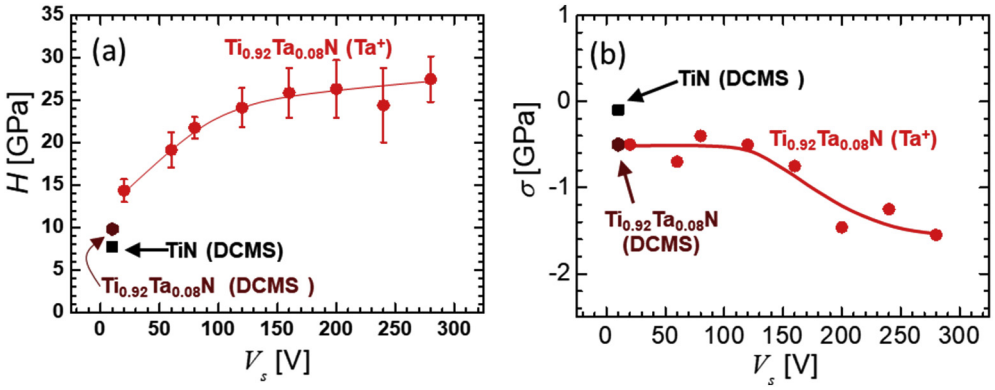

Fig. 25. (a) Hardness H and (b) residual stress σ of Ta-HIPIMS/Ti-DCMS $Ti_{0.92}Ta_{0.08}N$ films as a function of the applied substrate bias voltage V_s synchronized to the metal-ion-rich portions of HIPIMS pulses. Results are also shown for reference layers grown on Si(001) substrates: DCMS TiN deposited with $V_s = 10$ V (squares), and DCMS $Ti_{0.92}Ta_{0.08}N$ alloys grown at $T_s < 120$ °C with $V_s = 10$ V (diamonds). From reference [77].

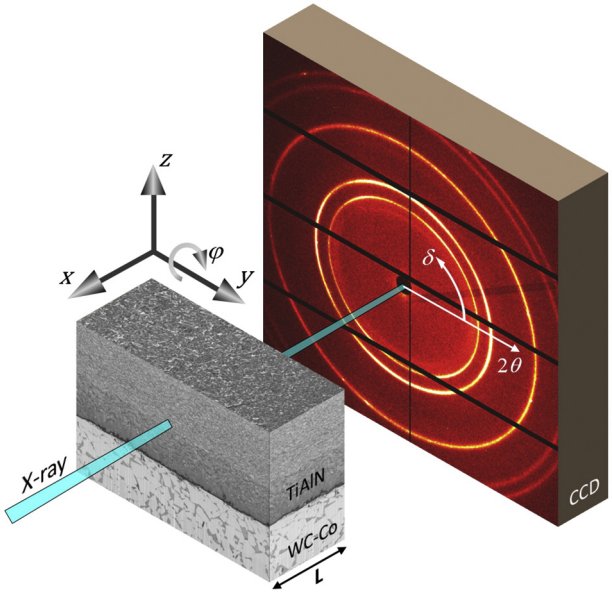

Fig. 26. A schematic setup of X-ray nanodiffraction experiment performed in transmission geometry on a section of a graded $Ti_xAl_{1x}N$ thin film on Si(100) with a thickness L of 30 μm. During the experiment, the sample is moved along the z axis and Debye-Scherrer rings are collected using 2D CCD detector. From reference [78].

gasoline has a specific energy of 42 MJ/kg [83]. In contrast to the gravimetric energy density, the volumetric energy density is very low: H_2 has a value of 10 MJ/m^3 at ambient conditions as compared to gasoline which has 32 GJ/m^3 [84,85].

The main parameters to characterize the efficiency of a hydrogen storage system are the gravimetric storage density γ_G and the volumetric storage density γ_V. As an example, for mobile applications the system targets for 2017 are $\gamma_G = 5.5$ wt% and $\gamma_V = 40$ kg/m^3 [86].

For a single storage system one of these storage densities may be high, but cases where both are high are rare. Therefore, hybrid systems combining the advantages of single components are a logical approach to this dilemma.

Hollow Glass Microspheres (HGMs) have a high gravimetric storage density and are relatively cheap compared to other storage solutions. No pressure vessel is needed for storing the spheres. However, they have a low volumetric storage density and need heating energy for the hydrogen releasing process.

Hydrolytic systems, where hydrogen and heat is released during a chemical reaction, on the other hand, have both high gravimetric and high volumetric storage density. Combining those two complementary systems is a potential solution to overcome the problematic issues of both approaches [87]. The heat generated by the hydride can be used for heating the HGMs and thus inducing the diffusion process of hydrogen out of the HGMs.

A hybrid system as described above can be constructed by commercially available HGMs [88] and Sodium Borohydride, $NaBH_4$. Hydrogen can be stored in the HGMs by filling them at elevated pressures and temperatures and the heat ΔQ generated from the chemical

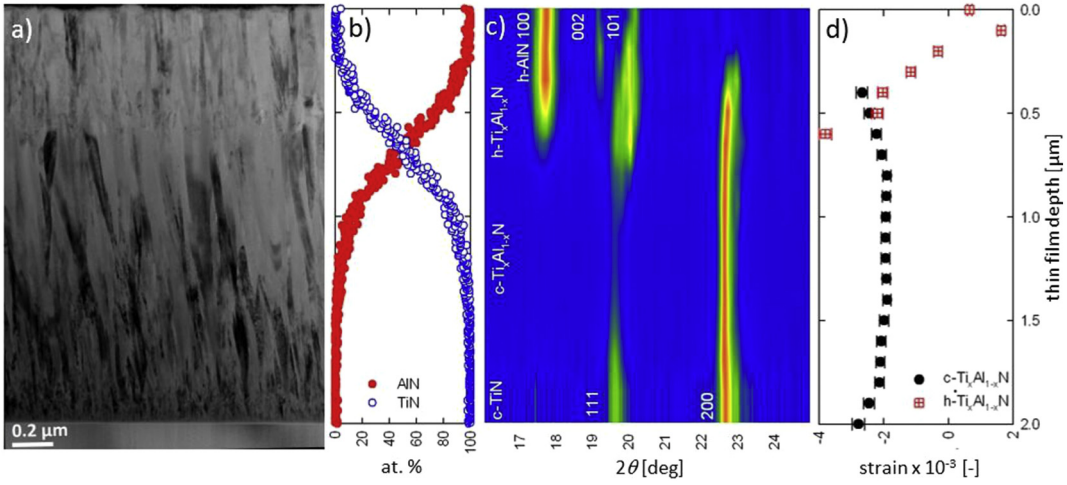

Fig. 27. (a) XTEM micrograph of the TiAlN sample revealing two nucleation regions, at depths of ~0.6 and ~2 μm and a columnar grain microstructure, (b) compositional gradients evaluated using EDS-STEM show depth distributions of AlN and TiN in the film. Changes in (c) the hexagonal morphology of $Ti_xAl_{1-x}N$ reflections and in (d) residual X-ray elastic strains within c- and h- $Ti_xAl_{1-x}N$ phases correlate with (a). From reference [80].

reaction.

$$NaBH_4 + 2H_2O \rightarrow NaBO_2 + 4H_2 + \Delta Q \quad (1)$$

can be utilized to release the Hydrogen stored in the microspheres.

To trigger the reaction given in (1), however, requires a catalyst which can be applied to the surface of the microspheres. Although liquid or gas phase-based processes allow for the uniform coating of granulates with average diameters ranging from 10 μm to several 100 μm, the choice of materials using these methods is limited. PVD processes like magnetron sputtering, on the other hand, offer the possibility of a free choice of materials by choosing non-reactive or reactive processing routes. The system geometry can be chosen freely, e. g. bottom up or top down, because the material sources remain in the solid state in the case of magnetron sputtering. If more than one source is used, then the deposited coatings will form compounded materials with gradient layers and multilayer systems becoming possible when the sources are operated independently. Nonetheless, the big limitations of PVD processes is their line-of-sight nature due to the large mean free path of the film forming particles, which is in the range of a few millimetre to several centimeter depending on the pressure in the deposition chamber [89]. Therefore, within an ensemble of particles, the beam of film forming atoms or ions is mostly blocked by adjacent granules. Deposition happens only on the particles which are exposed to the vapor beam on the surface of the powder. Therefore, it becomes clear that, if particles are to be coated by PVD methods, or magnetron sputtering, coating uniformity will require a method of efficient intermixing of the particles during the coating process.

This efficient particle intermixing has been developed by a customized deposition system which is described in detail in [90] and employs a rotating drum. The container is freely positioned on a circular plate which is tilted by a given angle. When the outer drum is rotated, the inner drum is lifted by small protrusions mounted on the outside of the drum until its centre of gravity wanders beyond the protrusion. Then the container moves over the tilted surface until it is stopped at the wall of the outer drum with an abrupt/concussive impact. This process is displayed in Fig. 28 [91].

If one assumes the mass of a single cubic particle (side length 50 μm, density 10 g/cm^3) to be approx. 1 μg, then for a lifting height of about $H = 5$ cm, upon neglecting the friction between container and plate, conservation of energy yields the speed of the container v to be approx. 0.1 m/s. Considering the time for stopping at the rim of the plate to be 0.1 s, then the inertial force exerted onto one particle by the abrupt stop can be calculated to be approximately 1 μN. Following the calculation given in [92] the force needed to separate one nm^2 of van der Waals bonded contact surfaces can be estimated to be about 10 nN–20 nN for Al with a surface tension $\sigma = 1.44$ J/m^2. Therefore, the inertial force exerted the particles should be more than sufficient to overcome the contact forces existing e. g. between the surfaces of two metal coated particles. On the other hand, these forces are low as compared to the Force needed to separate for instance an area of 50 μm × 50 μm at a yield strength of 100 MPa, which amounts to 0.25 N. So it can be expected that damage to the particles is unlikely, even if crack initiation is not considered here. The prototype described in Ref. [88] was scaled up and is now capable of coating up to 1 l of granulate particles. The upscaled version of the apparatus is displayed in Fig. 29.

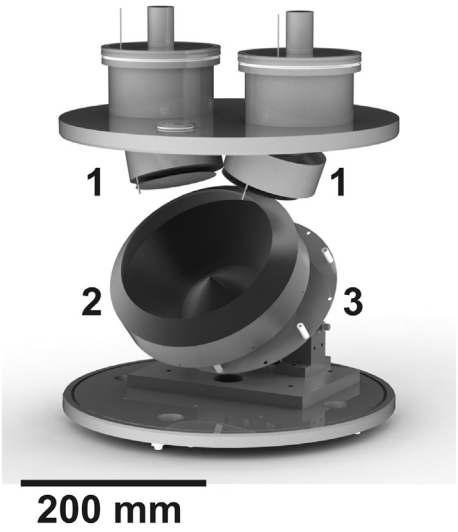

Fig. 29. Rendering of the upscaled deposition set-up: sputter sources, (2) powder container, (3) concussion plate.

Using the deposition set-up described before it was possible to uniformly apply several types of catalytic coatings to HGMs with an average diameter of approx. 50 μm and a wall strength of approx. 1 μm. The coating thickness was in the range of 1 nm to 5 nm, being fully sufficient to show pronounced catalytic effects, as will be shown later. A comparison of uncoated and coated microspheres is displayed in Fig. 30. The coating material is Pt with a thickness of approximately 2 nm.

Even the first qualitative impression suggests a high coating uniformity on single spheres. Quantitatively, the film thickness on single spheres can be evaluated by optical methods, since both the coating and the microspheres are transparent, which makes it possible to evaluate the thickness of the metallic layer according to Beer-Lambert law,

$$\frac{I_t}{I_0} = e^{-\alpha \cdot d} \quad (2)$$

where I_t and I_0 are the transmitted and the incident intensity of electromagnetic radiation, respectively, α is the extinction coefficient and d is the film thickness. Upon knowledge of α dependence on the wavelength, d can be calculated. This can be achieved by processing images acquired with a commercially flatbed scanner or with an optical microscope if the wavelengths for the RGB (Red, Green, Blue) channels of the respective device are known. Using this method, film thickness histograms of ensembles of coated spheres could be generated which show a width of approx. 0.5 nm at an average Pt thickness of 2 nm.

Finally, to test the catalytic properties of selected coatings, a set-up was constructed which evaluates the efficiency of the chemical reaction given in Eq. (1) in respect to hydrogen yield and temperature output. The experimental apparatus is displayed in Fig. 31 and consists of the following components: a three-necked flask was used as a reaction chamber where water was added to a mixture of $NaBH_4$-powder and coated HGMs. One port of the flask is used for a thermocouple for reaction temperature measurement, one port is connected to a dropping

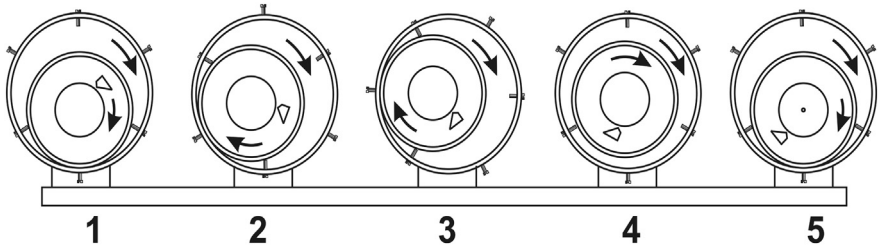

Fig. 28. Motion profile of the powder container (inner drum) on the concussion plate (outer drum), taken in simplified form from Ref. [91]. (1) Bottom position (2) container lifted by protrusion (3) topmost marginally stable position (4) center of gravity moves over protrusion, container starts to move over the protrusion towards the outer drum/concussion plate (5) container hits rim of outer drum with an abrupt/ concussive impact that serves to uniformly agitate the particle inside the inner drum.

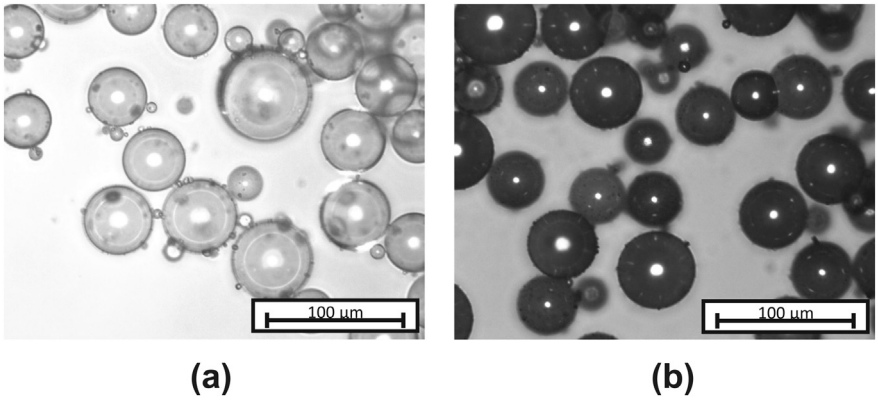

Fig. 30. Optical micrograph of (a) uncoated HGMs and (b) HGMs coated with approx. 2 nm Pt catalyst. The uniform discoloration upon coating indicates a high thickness uniformity on the singles spheres as well as on the visible ensemble.

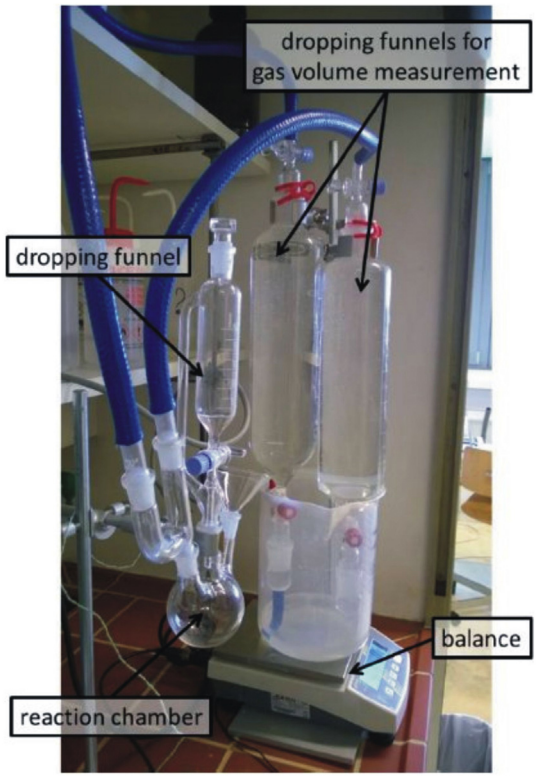

Fig. 31. Overview of the catalysis experiment. Hydrogen yield is measured by water displaced from the dropping funnels. For details see text.

funnel that was used to inject the water into the reaction chamber and one port is connected to a gas volume measurement unit by a hose (see Fig. 31).

The hydrogen gas volume was measured with two dropping funnels, each with a volume of ~1300 ml (scale 1000 ml) that were filled with water. Displaced water was measured in a beaker with a volume of 3000 ml and a balance (Kern PCB 6000 g ± 1 g) [93]. Before each test, the air was evacuated from the system with an aspirator so that the water inside the beaker was sucked into the dropping funnels until they were full (the pressure difference between inside and outside the system being the driving force). When hydrogen is released in the reaction chamber, its volume can be determined by measuring the mass of water in the beaker on the balance.

Typical data extracted from this experiment are displayed in Fig. 32.

During the whole reaction, hydrogen yield and temperature were monitored. The theoretical maxima given in Fig. 32 were calculated using reaction Eq. (1) and the weighed quantities of 0.81 g of $NaBH_4$ (Venpure™ SF powder, Rohm and Haas) and 0.81 g of catalyst coated hollow glass microspheres. Fig. 32 clearly shows an increased hydrogen release and temperature rise for the Pt coated microspheres, which is, however, still far away from the theoretical limits. In a second step, therefore, other catalysts were investigated and, finally different layer architectures were applied to allow for a re-use of catalytically coated HGMs. In a screening of other possible catalytic materials, Ruthenium (Ru) proved to exhibit excellent performance, as Fig. 33(a) shows.

Both, hydrogen yield (Fig. 33(a)) and temperature rise during the reaction were close to the theoretical limit within error bars. Nonetheless, when Ru was directly deposited onto the microspheres, after one use the catalyst was completely washed off from the spheres. Final investigations therefore were focused on applying different layer architectures to prevent this corrosive adhesion failure. To do so, the capability of the deposition device to operate different sources in reactive or non-reactive sputtering mode was exploited. First layers of pure Ti, pure TiO_2, co-sputtered TiO_2 and Ru or graded layers from TiO_2 via TiO to Ti were deposited by a variation of the oxygen flux into the chamber. On top of these so-designed support layers, a 0.2–0.6 nm thick Ru-top-layer was deposited for most samples. Detailed data in the samples are given in Table 1.

Fig. 33(b) shows the Hydrogen yield measured in the catalysis experiment measured for samples 1–4. While a purely metallic support layer (Sample 1, Ti) even leads to decreased performance, oxides co-deposited and graded base layers have an extremely positive effect. Sample 2 still lost catalytic performance after two subsequent experiments, but samples 3 and 4 could be recycled up to four times. The

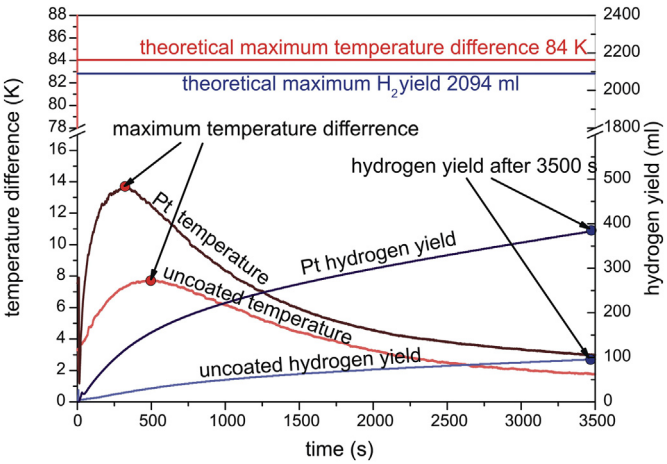

Fig. 32. Typical raw data extracted from the catalysis experiment; comparison of uncoated and Pt coated microspheres.

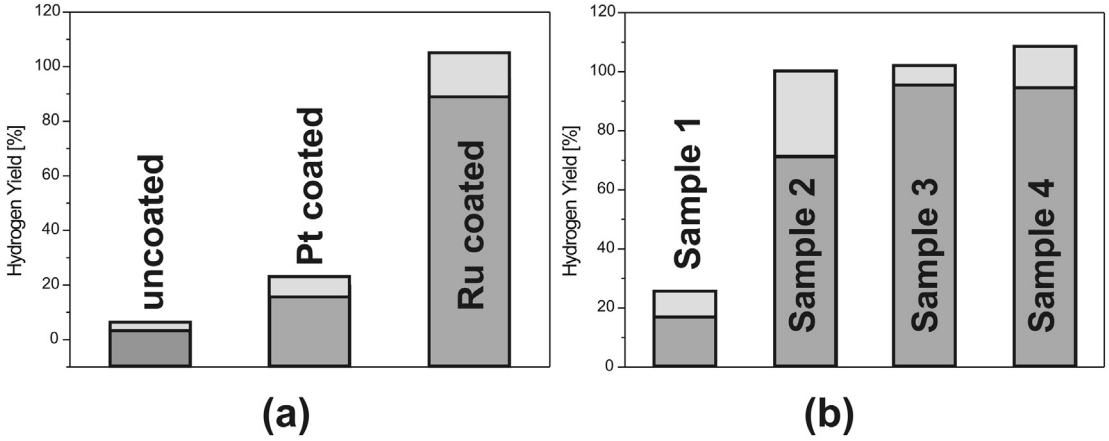

Fig. 33. Hydrogen yield of reaction Eq. (1) for differently coated HGMs: (a) Microspheres coated with different catalysts and (b) Ru on different supporting layers. For sample details see Table 1. Light grey regions in bar chart denote measurement uncertainty.

Table 1
Details of the film architecture of the base layers for HGMs coated with Ru based catalysts.

Sample number	Supporting layer architecture	Ru layer thickness
1	Ti (0.4 nm)	0.2 nm
2	TiO_2 (0.2 nm)	0.2 nm
3	TiO_2 (0.15 nm) co (TiO2&Ru) (0.55 nm)	No pure Ru top layer
4	TiO_2 (0.15 nm) TiO (0.2 nm) Ti (0.3 nm)	0.4 nm

reason why more repetitions were not possible was due to the gradual loss of material during extraction and re-insertion of the used spheres into the reaction chamber.

In conclusion, the presented deposition equipment makes it possible to apply homogenous coatings to granulates with average grain sizes from 10 μm to 100 μm and with different grain shapes. An application in the field of hydrogen storage was presented; however the method is also suitable for other applications where surface modification by thin layers is necessary. These could be related to materials science applications where surface modification of sintered powders would enable product branding. Here the surface modified particles would have unique markers enabling easy product identification in the market place. The method can also find applications in interdisciplinary fields like energy harvesting and storage, where a classical PVD technique may deliver solutions which serve as components in complex systems.

10. Challenges in nanocrystal-based electronic devices

Electronic materials based on nanocrystals (NCs) are able to provide novel materials with unprecedented and spectacular properties with applications in a wide field of areas ranging from solar cells, memory devices, thermos-electrics, spintronic devices or printable electronics [94]. Among a huge variety of semiconductor NCs investigated in the last decades, group-IV NCs have emerged as a natural way to extend, enhance and control the properties of their respective bulk electronic materials. The last two decades of an extensive research have shown that the growth and characterization techniques have to be redesigned to meet their very specific requirements.

The surface of NCs largely determines their electronic and optical properties. Si NCs are especially reactive in air, immediately forming an oxide cap. The NC surface is crucial for engineering the NCs interaction with air, solvents or solid matrices. Together with surface properties, other challenges include, but are not limited to, the control of the interface, defects and doping of NCs. Those properties are crucial for any electronic device application.

The use of semiconductor NCs instead of floating gate devices like in standard complementary metal-oxide-semiconductor (CMOS) field effect transistors and memory devices, makes charge storage less sensitive to common problems such as leakage current and dielectric breakdown [88]. Moreover, NCs offer significant breakthroughs in photovoltaics as they can overcome the thermodynamic efficiency limit of a conventional junction cell.

Ion beam assisted synthesis of semiconductor NCs has been extensively studied in the past years [94]. As ion implantation is used in current CMOS technology, it is desirable to use it for NC fabrication. In addition to NCs growth, ion implantation is also a promising technique for NC doping. However, several unresolved issues with NC doping limit the application of NCs in electronic devices. NC size, shape and distribution can be controlled by varying the implantation conditions (implantation energy and dose) and subsequent annealing. A huge effort has been devoted to the understanding of the energy loss process and defect formation in implanted materials. However, ion implantation introduces different (mostly electrically activated) defects in materials. It is also a well-known fact that Si-ion implantation of SiO_2 is characterized by the production of a large number of oxygen vacancies and other defects in the oxide matrix. These defects play a crucial role in the process as they enhance the NC formation and the formation of the sub-oxide interface states [95].

Recently, it was shown that in order to study donor doping by ion implantation and dependences of the photoluminescence (PL) intensity in such systems, it is crucial to understand and control the presence of defects. The effects of donors and defects to the PL of Si-NCs are strongly overlapping [96]. It was reported that a decrease in the density of interface related defects could be achieved by light phosphorus doping [97]. In addition, Crowe et al. [98] have shown that as phosphorus accumulates at the NC-oxide matrix interface it leads to passivation of the dangling bonds as observed by the luminescence enhancement.

Interface related defects play a significant role for semiconductor-based NCs that are embedded in other materials. Among all semiconductor NCs, Si NCs embedded in silicon dioxide (SiO_2) matrices have been most extensively studied. One of the first approaches to explore such systems, was to form multilayer structures by a reactive evaporation [99]. subsequently, a more advanced growth technique, magnetron co-sputtering, has replaced reactive evaporation by enabling better control of NCs' size, shape and distribution. In addition, magnetron co-sputtering has enabled new possibilities for novel electronic materials via variation of the sputtering time, composition of sputtered material, and the deposition temperature.

Since NCs embedded in an oxide matrix have a large interface area-

to-volume ratio, they show a high density of interface defects [100]. These interface defects are located at the substrate-oxide matrix interface and at the NC-oxide matrix interface. Unlike the other defects located in the oxide matrix, such as fixed and mobile oxide charges, interface-related defects are in electrical communication with the underlying substrate [99]. Those defects act as traps for charge carriers and therefore largely affect the charge transport properties of such materials and, as a result, limit the NCs' applications in novel electronic devices.

Different electrical characterization techniques are currently used for studying the charge transport properties of embedded NCs. Among all methods the most common is the current-voltage (I-V) measurement. The other widely used techniques for describing the charge transport properties are different conductivity mechanisms such as direct tunneling (DT), trap-assisted tunneling (TAT), Fowler-Nordheim tunneling (FN), Poole-Frenkel (PF) conduction and space charged limited current (SCLC) [101]. It has been shown that transport properties are affected by the NC's size and space distribution. In particular, Zhou et al. [102] have studied the influence of the Si-NC's diameter on charge transport, and explained the influence by the percolation-hopping conduction mechanism. Another application of the semiconductor NCs embedded in the oxide matrix is in memory devices. In such metal-oxide-semiconductor (MOS) structures the charge trapping may occur at (i) substrate–oxide matrix interface traps, (ii) traps inside the oxide matrix, (iii) inside NCs; (iv) NCs–oxide matrix interface traps [103]. The first step in analyzing the charge trapping properties of such MOS structures is to check the existence of substrate-oxide interface traps. This information can be obtained from temperature-dependent C-V measurements. The low temperature shift of C-V dependence is well known effect due to the discrete energy levels related to the interface states [104]. Thus, it is important for any electronic device applications to passivate such substrate-oxide matrix interface-related defects. Another source for increased density of interface traps is vacuum annealing, which is commonly used for NC crystallization (embedded in the oxide matrix). However, most of the interface defects induced during vacuum annealing can be neutralized by means of a low-temperature (450 °C) anneal in a hydrogen or forming gas atmosphere [100]. In addition to characterization of the interface defects, C-V dependence can provide valuable information about the memory window, i.e. the flat band voltage shift (ΔV_{FB}). The effective density of trapped charges is estimated from the flat band voltage shift using the following formula [105]:

$$N_{ch} = \frac{C_{ox}\Delta V_{FB}}{qA}, \tag{3}$$

where q is the elementary charge, A the area of the gate contact, and C_{ox} the capacitance of the MOS structure in the accumulation region. According to a model of fixed oxide charges, the flat band voltage shift depends on the size and density of embedded NCs [103]:

$$\Delta V_{FB} = \frac{qN_{ch}}{\varepsilon_{ox}}\left(d_{ox} + \frac{\varepsilon_{ox}}{\varepsilon_{NC}}R_{NC}\right), \tag{4}$$

where N_{ch} is the effective density of trapped charges, ε_{ox} and ε_{NC} are dielectric constants of the oxide and NC-material, respectively, d_{ox} is the oxide film thickness, and R_{NC} is the NC radius.

To get additional information about electrically active defects in systems with embedded NCs, deep level transient spectroscopy (DLTS) can be applied. This technique, commonly applied for studying the electrically active defects in bulk semiconductors, has been used for studying defects at the Si-SiO_2 interfaces [106] and within embedded semiconductor NCs [103,107].

Fig. 34 shows DLTS spectrum of the simple MOS structure, with Ge NCs embedded in a SiO_2 film grown on a Si substrate. Gold contacts were deposited via thermal evaporation on both the back-side surface of the Si substrate and the front-side side of the samples through a mask with circular openings with area of 0.8 mm^2. By careful adjustments of the measurement settings, the thermal emission of electrons from the NCs can be detected by DLTS [103]. Based on the DLTS analysis, the activation energy of the electron emission for the NC-related trap is estimated from the Arrhenius plot. The interpretation of the estimated activation energy follows the simple confinement model, in which this energy corresponds to the difference between the two lowest energies of the confined states [103,107].

11. Biointerphases

11.1. Challenges in biomedical interface synthesis and characterization

Research in the biomedical field is in continuous expansion increasingly favored by new advancements from other fields of science and technology. The control of biomolecular and cellular interactions is of crucial interest in this field, and can be approached through the modification of materials surfaces of all natures and at all scales. In parallel, progress in the biomedical field passes through involvement in the understanding of the intricate properties of biomedical interfaces. Relevantly, vacuum science and technology currently provides a palette of new techniques for the manipulation and characterization of matter, which are especially adapted for living structures, providing continuous breakthroughs [108]. In the forthcoming paragraphs we describe four different examples of the preparation of biointerfaces in which vacuum techniques play a fundamental role in the modification or ulterior analysis. These consist of supported (porous) nanomaterials, bulk (metallic) biomaterials, first stages of calcium phosphate nucleation and an additional example to illustrate current developments in the understanding of nanoparticle-molecule conjugates.

11.2. Surface functionalization of nanorough-porous structures

Nanorough-porous structures are reliable supports for an increasing number of biomedical processes applied to both diagnostic and therapeutic approaches. The increase of the specific surface area in these materials with respect to their bulk counterparts allows tailoring biomolecular interactions. For instance, surface chemistry modification has already been applied to porous alumina [109], titanium oxides [110] and silicates [111]to provide particular biomolecular functionality. Relevantly, a discrepancy in the early biomolecular/cell response

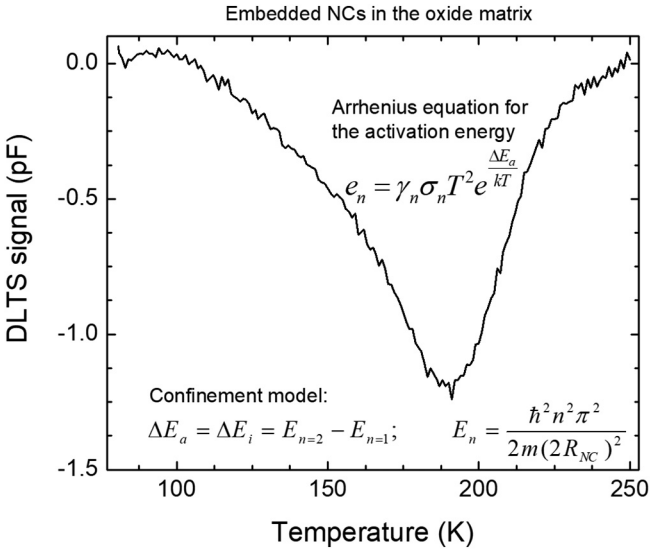

Fig. 34. An example of DLTS spectrum of the MOS structure, with Ge NCs embedded in the SiO_2 oxide matrix. Details about DLTS analysis are given elsewhere [94,103].

to nanorough surfaces remains, some authors claiming an increased affinity, and others claiming their antifouling properties [112].

We bring here as an example, the surface analysis of UV activated monolayers of aminopropyl triethoxy silane (APTS) on porous silicon (PS), a versatile matrix relevant for enhancing bioanalytical techniques such as desorption ionization mass spectrometry, surface-enhanced Raman scattering and chromatographic separation. PS is formed from Si wafers ((100) p-type B-doped) by anodization in HF electrolytes. The functionalization with APTS takes place in a glove box in EtOH solutions at very low concentration (0.2% v/v) and considering two UV irradiation times of 10 min and 30 min.

The analysis by XPS of this surface activation process demonstrates that it initially promotes the functionalization of the PS surface (10 min), but it is detrimental for the immobilization of amine groups at long times (30 min) as shown in Fig. 35(a). The general surface stoichiometry evidences the presence of C, N, O, Si and F (synthesis trace). Relevantly, the concentration of all these elements is reduced by the increased UV irradiation, with the exception of O, which increases moderately from 32.4 at.% to 43.4 at.%. The 10 min UV activation promotes an organic stratum of 12.7 at.% C, which is enough to sustain a N composition of 1.2 at.%. However, the long activation time depletes this organic support layer (10.1 at.%) and leads to a decrease of the immobilized N (0.8 at.%). A dramatic change of the bonding chemistry is revealed by the core level spectra. Fig. 35(b) shows the C1s core level spectra of the samples irradiated for 10 min and 30 min. Four mayor contributions can be outlined with the characteristic C—C bond at 285.0 eV binding energy (BE), the C—N from aminopropyl at 286.3 eV, the C—O contributions at 286.3 eV and the C═O bonds at 289.0 eV. The two intermediate peaks suffer from a clear inversion of intensities, indicating the progress of oxidation processes that deplete the C—N bonding in favor of C—O bonds. This oxidation process goes further into the PS matrix as evidenced by the analysis of the Si2p core level spectra in Fig. 35(c). It is shown that at short activation times, the nature of the structure still consists of Si—Si and Si—H bonds (peak at 99.5 eV),

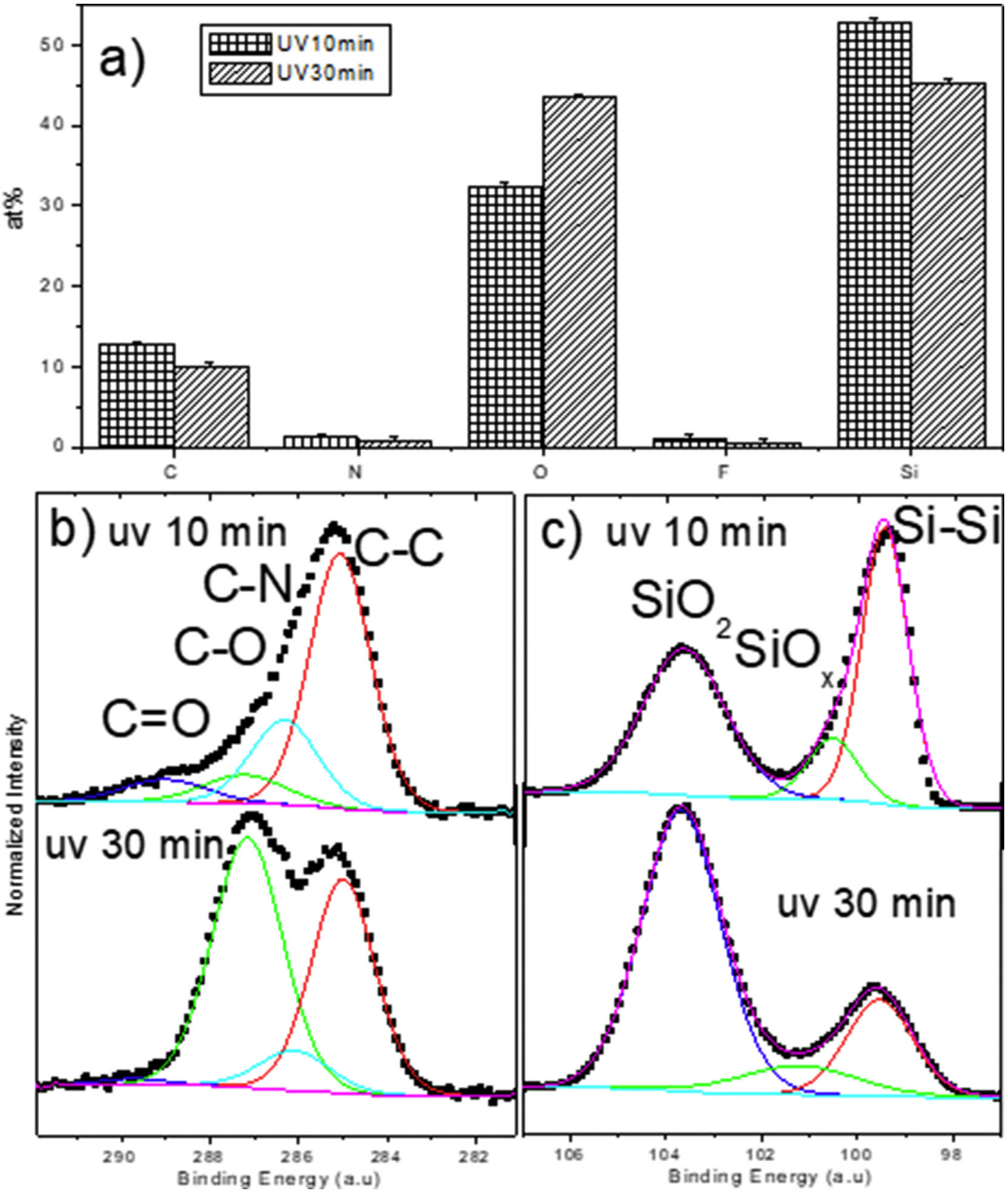

Fig. 35. XPS study of UV activated silanization of PS with APTS. (a) General surface stoichiometry after 10 and 30 min UV activation. C1s (b) and Si2p (c) core level spectra of the samples activated at the two different times.

although the presence of emerging (SiO_x) and consolidated silica species (SiO_2) is confirmed by the peaks at 101.0 and 103.5 eV, respectively. Again, the increase of UV activation induces an inversion in the peak contributions, and SiO_2 becomes the dominant contribution after activation for 30 min.

These transformations of the surface chemistry have a direct impact on the surface tension of the samples. Water contact angle (*wca*) measurements on these samples showed that a drastic decrease of the contact angle is induced, from hydrophobic behavior ($wca = 126^{\circ}$) for pristine PS dominated by Si−H bonds, with gradual decrease to 52° for short activation dominated by APTS and hydrophilic behavior ($wca = 32^{\circ}$) for long time functionalization dominated by the presence of C−O bonds. Overall, this study outlines that the UV activation passes through an ideal regime, but an overall oxidation/depletion of immobilized amine groups is facilitated by long exposure. Indirectly, the study outlines the importance of characterizing all surfaces (and in particular nanorough surfaces) before and after sterilization steps (often performed with UV) prior to any biomedical test, since the UV process can reverse the high affinity of the surface towards biomolecular interactions to an antifouling behavior (or vice-versa).

11.3. New smart metallic biomaterials: from corrosion resistance to biodegradable metallic devices

The history of metals as biomaterials is more recent than the history of biomaterials themselves as it dates back to Antiquity. The first record of an application of metal in a surgical procedure is from 1565. Before aseptic surgical techniques were known (1860), the metal devices were wires and pins, made of pure Fe, Au, Ag, Pt, etc. but their integration was not always successful due to the high risk of infection. The use of alloys in surgical implants is a relatively recent event, from the late 19th century and mainly during the 20th century [113,114].

Metallic biomaterials mainly (but not only) consist of alloys for prosthesis and stents: as temporary devices and total hip substitution (stainless steels), total joint replacements and dentistry castings (Co-Cr-Mo alloys), stem and cup of total hip replacements and permanent devices (Ti-based alloys), orthodontic dental archwires, vascular stents and staples (NiTi), and wire sutures (Ta). All these metals present excellent biocompatibility (immune response), suitable mechanical properties, osseo (or vascular) integration, reasonable cost and high corrosion resistance, being the latter of paramount importance [115].

Corrosion resistance has always been a key point for the development of new metallic biomaterials. In contact with human fluids (blood plasma, serum), corrosion can develop at the surface of metals and alloys used as biomaterials, generating chemical failure such as general dissolution or localized corrosion (galvanic or pitting). The human body requires low levels of metals and metallic ions to function properly, such as Fe(II) contained in heme groups of hemoglobin or myoglobin required for oxygen transport, or Cu (Cu^+ or $Cu_2{}^+$) allowing the regulation of iron transport, or Cr, playing a role in the regulation of the sugars level; however, these metals can be cytotoxic if the dose in biological fluids increases [116]. Corrosion resistance is directly linked to the presence of a spontaneously formed passivating oxide layer [117]. One way to improve corrosion resistance consists in elaborating alloys with elements improving this property. For example, Fe is not passivating at the physiological pH of human fluids (blood plasma, serum), resulting in iron salt release in the human body, but chromium addition (≥11 at.% to make stainless steels) can prevent the formation of rust or metal dissolution. Similarly, incorporation of Ni in steel allows the formation of austenitic phases with good corrosion protection. As an alloying element, Mo also limits the pitting corrosion [113].

Recently, a new generation of biomaterials called “third generation biomaterials” uses the property of biodegradability to improve the functionality of devices. For metallic materials, biodegradability consists in the dissolution of the metallic implant in the biological medium. Thus, corrosion is used in a favorable way. At pH values of about 7, only few metals can be dissolved. Cheng et al. tested the in vitro corrosion rate of Fe, Mg, Zn, Mn and W [118]. W presents a too low corrosion rate, while pure Mn has a high cytotoxicity which prevents using it alone, although it can be alloyed in the Mg. On the other hand, Zn may present cytotoxicity depending on the cells, but could be considered for specific implantation. Fe and Mg are currently the only biodegradable metals in use, but Mg presents both a relatively high dissolution rate and a high ratio of hemolysis, which improves in vitro by alloying [119].

Thus, control of the metal dissolution rate is the key question for the use of degradable metallic biomaterials and many parameters play a role in this phenomenon, among which: alloying elements, buffer solutions, concentration of inorganic ions, dissolved oxygen, and adsorption of biological molecules [120]. Metal dissolution can also introduce localized corrosion (pits, crevice, galvanic coupling) which can be particularly harmful.

However, the choice of Mg as a lightweight biodegradable metal via corrosion in the electrolytic environment of the body could be used in two medical applications: coronary stents [121] and bone repair [122]. It is a technological challenge to engineer biodegradable metallic implants dissolving as new tissue is formed. The paradigm in biomaterials science is thus no longer to develop highly corrosion resistant metals, but rediscovering Mg and Mg alloys. Main advantages consist of: no need to withdraw the implant (in orthopedic surgery for example) and no long term effects (as thrombosis and restenosis, or even thrombosis in the case of stents, Fig. 36).

However, development of biodegradable metal implants is a complex problem because it combines engineering and medical requirements for a material. One open question is the presence of H, related in the case of Mg dissolution [123], on which several theories are proposed: one of the more interesting relies on the presence of impurities in the metal, which catalyze the H^+ reduction (Negative Difference

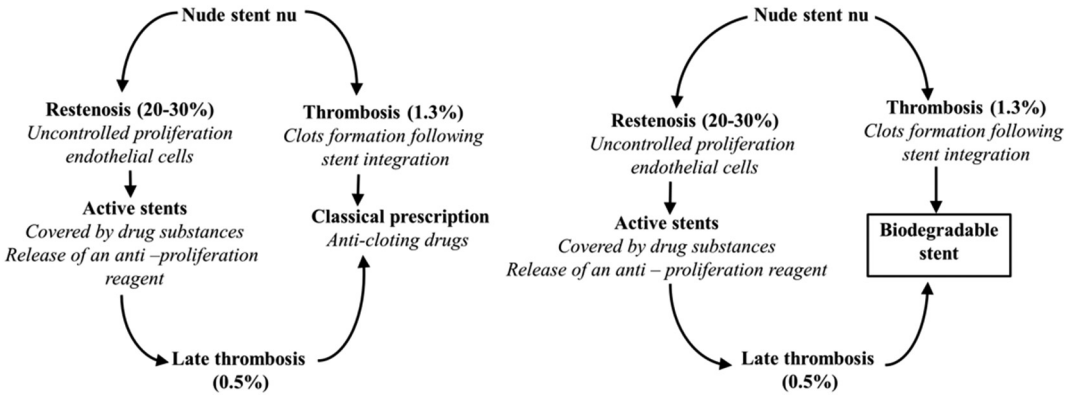

Fig. 36. Illustration of the benefit of a biodegradable biomaterial (for example Mg or Mg-based alloys) in the case of stents.

Effect). Another question of interest is the control of this dissolution by engineering a bioactive surface (implying biofunctionalization): there, research is going towards building 3rd generation biomaterials, making benefit of metal corrosion, as for example replacing classical prescriptions for biodegradable stents.

11.4. First nucleation stages of calcium phosphates studied by HAXPES

Another hot topic in the forthcoming years will derive from the growth of biomaterials for tissue engineering and regenerative medicine through layer by layer deposition methods. In these processes, elemental/molecular components are integrated in the sample on a cyclic basis, allowing a more precise control of final composition and properties. The most extended process, atomic layer deposition (ALD), emerged as a refinement of chemical vapor deposition (CVD) for particular biomaterial applications such as infiltration, and exploited for instance in the metallization of cellulose fibers [124]. Extending the process to organic functionalities, molecular layer deposition (MLD) has also been highlighted as a highly controllable process for biomaterials synthesis [125]. Analogue wet methods have been developed for the optimization of polyelectrolyte-enzyme complexes by cyclic polarization [126]. Here we present an example of nucleation of calcium phosphate (CaP) by cyclic electrochemical deposition (CED) designed in particular for the nucleation of hydroxyapatite (HAP). The first steps of this process have been studied on porous silicon substrates (PS/CaP) as a high surface area electroactive support. In order to study the chemical composition of the PS/CaP interface, hard X-ray photoelectron spectroscopy (HAXPES) was carried out exploiting its nanometer scale in-depth chemical sensitivity (SpLine, BM25, European Synchrotron Radiation Facility). Nucleation was activated in equimolar Ca^{2+} and PO_4^{3-} solutions using identical anodic and cathodic currents and activation times according to the ratio $t_{Ca}/t_P = 1$ (30 s each) [127]. P 1 s and Ca 1 s core level spectra were measured using photon excitation energies of 8.5, 12 and 15.5 keV. Fig. 37 shows spectra from the PSi/CaP interface.

The P 1 s spectra of the CaP interface are shown in Fig. 37(a). The peak detected at 2149.0 eV is assigned to P—O/P═O bonds (2148.5 eV) related to CaPs, while a peak for P^0 is identified at 2145.5 eV [128]. Similarly, Ca 1 s spectra of HAP reference are shown in Fig. 37(b), with a Ca^0 contribution detected at 4038.5 eV [128] and an additional peak at 4042 eV, assigned (in view of the higher oxidation state) to a CaP phase. Such CaP coating was previously characterized by X-ray diffraction (XRD), which confirmed the presence of a HAP phase, which has been used for labelling the mentioned CaP peak in the figure.

Although the full-width at half-maximum (FWHM) of the peak contributions increases for increasing photon energy, it is possible to observe that the P^0/(P—O + P═O) and Ca^0/HAP intensity ratios present a clear trend, showing an increase when photon energy is increased. This strongly suggests the presence of an in depth composition gradient, with a dominant fraction of oxidized states at the surface.

The Si 1 s spectra (not shown), present two contributions at 1838.9 and 1843.6 eV attributed to Si^0 and SiO_2 species, respectively, confirming the presence of an oxidation state gradient at the interface. In confluence with the previous Ca 1 s and P 1 s spectra, a mechanism of CaP nucleation on PS could be proposed. In fact, the presence of P^0 and Ca^0 components at the interface may be due to the electroactivity of PS, in which an oxidation process can induce the reduction of neighboring elements (especially metals) [129]. At lower excitation energies, the CaP phase is, however, readily oxidized and develops a HAP phase as identified by XRD. These results illustrate that the appropriate biomineralization of substrates for bone substitution/regeneration through a HAP layer can be controlled, but implies experimental conditions out of the expected stoichiometric equilibrium of the desired phase.

11.5. Nanomaterials in medicine

The possibility of integrating nanomaterials in medical devices is considered a great opportunity for customized, personalized and quantitative medicine in the future [130]. For instance, the possibility of using nanomaterials in neuronal prosthetic devices can improve their charge transfer, providing long term stability and open the possibility of realizing ultrasmall implantable devices [131]. On the other hand, the use of gold nanoparticles can strongly improve the efficiency of biosensors, while the application of different nanoparticles, ranging from metals to polymers, can provide modern platforms in theragnostic and drug delivery applications [132]. In fact the first nanoparticle-based therapy was approved by the FDA in the1980s. However, despite these encouraging results many efforts are still required to address several open issues related to the bioapplication of nanomaterials. In particular, there are still concerns about the possible adverse and toxic effects of these devices [133]. Moreover, the behavior of nanoparticles in biological environments is still far from understood. For instance, it is

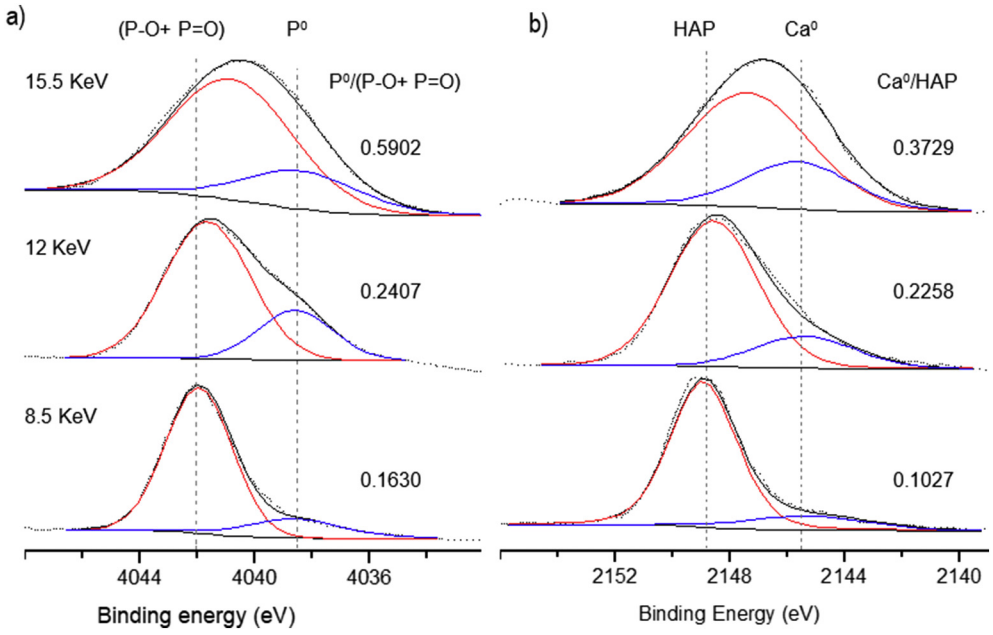

Fig. 37. Core level spectra of (a) P 1 s (4048 eV to 4032 eV BE) and (b) Ca 1 s (2156 eV to 2139 eV BE) obtained at 8.5, 12 and 15.5 keV excitation from HAP layer prepared by CED using identical I_{Ca}/I_P current fractions for 20 cycles of 30 s. Inset values refer to P^0/(P—O + P═O) and Ca^0/HAP intensity ratios.

accepted that upon entering in contact with a biological environment, nanoparticles are covered with a protein layer (or *protein corona*) [134]. However, the different mechanisms and the influence that the surface properties of nanoparticles may have on the proteins and cell organelles have still to be clarified. For instance, recent studies have shown that gold nanoparticles can influence the thermal folding and the secondary structure of human serum albumin (HSA), the most abundant blood protein [135]. Moreover, since most of the biomedical applications require robust, reliable and reproducible functionalization protocols, systematic characterization of nanoparticle surface chemistry needs to be carried out [136]. In this respect, it has been demonstrated that the application of X-ray Photoelectron Spectroscopy (XPS) and Time of Flight Secondary Ion Mass Spectrometry (ToF-SIMS) can provide valuable information, not only on the surface functionalization of nanoparticles, but also on their interactions with biological media [137].

However, to obtain useful and reproducible results, careful sample handling and preparation should be established [138]. For instance, a recent paper has shown that the use of XPS to assess biomolecules film thickness produced highly variable results due to the different sample preparation protocols used by different laboratories, thus indicating the need of a more standardized approach in the application of surface analysis techniques to nanomaterials [139]. Moreover, as shown in Fig. 38, XPS investigation of commercial nanoparticles indicate that the presence of undesirable surfactants and contaminants in nanoparticle solutions could lead to difficulties in obtaining surface functionalization, thus demonstrating the need of a careful assessment of the surface conditions of nanomaterials, especially if related to possible applications in the biomedical field.

12. Gaseous plasma for tailoring surface and sub-surface properties of materials

Non-equilibrium states of gases represent a powerful medium for tailoring surfaces and subsurface layers of solid and liquid materials. A common method for transferring gas at thermodynamic equilibrium to a non-equilibrium state is application of electrical fields. Free electrons in gaseous media interact with the field, gaining energy which is often sufficient to cause excitation, dissociation, or ionization of gaseous molecules—though the neutral gas kinetic temperature remains close to room temperature. The ionization events cascade, causing the density of charged particles to increase. If the electric fields are strong enough, the gas is transformed into the state of gaseous plasma. While the charged particles are neutralized in roughly a microsecond, many other species created in gaseous plasma persist well after the electric field has vanished. The lifetime of some species in a plasma reactor could be as large as a second, so the non-equilibrium state of the gas persists well after turning off the source of the electrical field. Such a state of non-equilibrium gas is often called plasma afterglow. A key challenge of plasma science is determination of the temporal and spatial distributions of reactive gaseous species. These include metastable particles, radicals such as neutral atoms and molecular fragments, and positively or negatively charged species as well as more exotic species that might form in gaseous plasma. The challenge is addressed both theoretically and experimentally. Due to the numerous reactions taking place in gaseous plasma and its afterglow, the theoretical models are complex. Some coefficients are not determined precisely enough, and furthermore they may drift with time and exposure to plasma treatment, particularly the surface properties of materials facing the plasma. The theory is therefore rather difficult, but current models predict the behavior of plasma species rather well providing the original gas is not too complex. Best results are obtained when modelling plasma in a pure gas and few gas mixtures such as a noble gas plus a reactive gas or air. A somewhat simplified approach, applicable to various plasmas, is to use global models. These can present an attractive first step, mainly due to their ease of development and use. These volume-averaged models describe plasmas with complex chemical kinetics, and without the computationally intensive numerical methods required for spatially resolved models. A review of such approaches has been published recently [140].

12.1. Low-pressure plasma

Solid materials are often treated by low-pressure plasma created in electronegative gases. In such gases, the free electrons may not be the dominant negatively charged gaseous species. Fig. 39 shows the time-averaged distribution of charged particles in plasma created by a radiofrequency (RF) discharge in a capacitive coupling mode (CCP) in tetrafluoromethane (CF_4). The density of negatively charged fluorine atoms is more than an order of magnitude larger than the electron density, and the density of CF_3^- ions is comparable. The results presented in Fig. 39 were obtained by a particle-in-cell simulation code for the case where plasma is sustained by composite voltage waveforms composed of four consecutive harmonics of peak-shaped waveforms [141]. The absolute value of the DC self-bias was found to increase by reducing the fundamental frequency, providing an increased range over which the DC self-bias could be controlled. The analytical model revealed that the increased DC self-bias was caused by changes in both the spatial profile and the mean value of the net charge density in the grounded electrode sheath. The spatio-temporally resolved simulation showed that the grounded electrode sheath region became

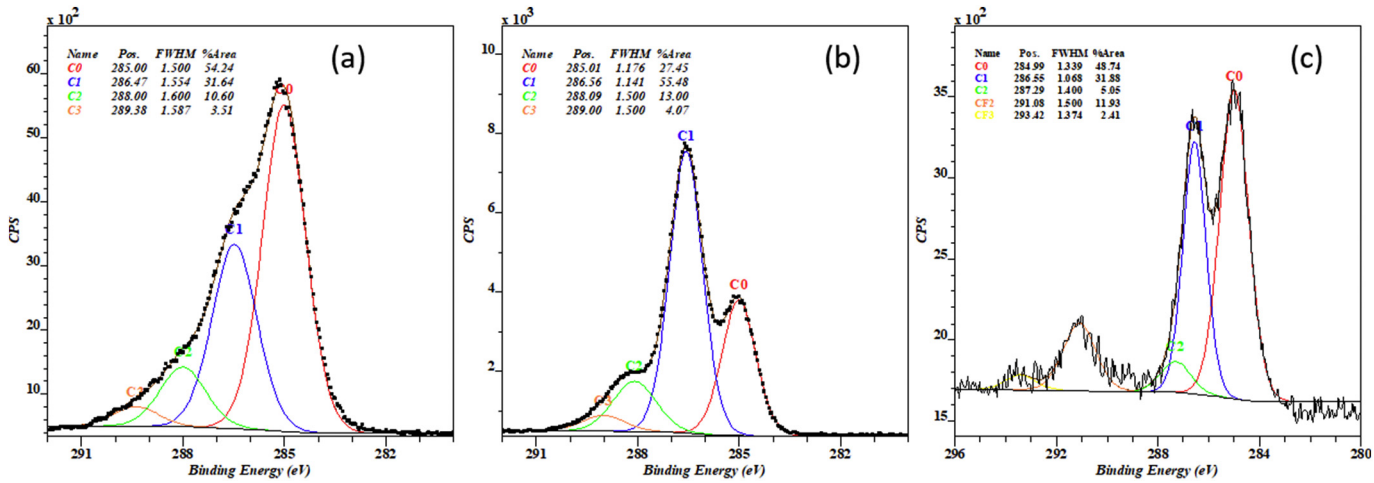

Fig. 38. C1s core level spectra of commercial gold nanoparticles: (a) as received, (b) after two centrifugation cycles and (c) after functionalization with 1H,1H,2H,2H-Perfluorodecanethiol ($CF_3(CF_2)_7CH_2CH_2SH$).

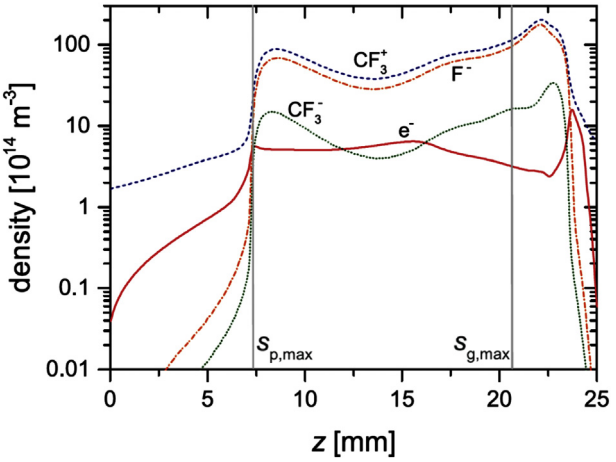

Fig. 39. The distribution of reactive gaseous species between the powered and grounded electrode of an capacitively coupled RF plasma sustained in CF_4 at pressure 80 Pa [145] The symbols $S_{p,max}$ and $S_{g\text{-}max}$ mark the maximal thickness of the sheath next to powered and grounded electrode, respectively.

electronegative as the frequency was reduced. The presence of negative ions in the sheath caused different dynamics in the power absorption of electrons, which in turn enhanced the local electronegativity and plasma density by ionization and attachment processes [142]. The ion flux to the grounded electrode (where the ion energy was lowest) could be up to twice that to the powered electrode. The ion kinetic energy and fluxes onto the solid materials play a crucial role in controlled etching of SiO_2 or more complex organo-silicate low-k dielectrics films in microelectronics [143] as well as functionalization of polymer materials for controlled adhesion of blood proteins [144].

Another type of electronegative gas that has attracted enormous attention of plasma scientists as well as users of plasma technologies is oxygen. Although it has been studied extensively for several decades, some aspects of oxygen plasmas remain poorly understood. Recent advances include application of tailored voltage waveforms for sustaining oxygen plasmas with capacitively coupled RF discharges [146]. The amplitude asymmetry effect and slope asymmetry effect at different fundamental frequencies has been studied experimentally and by kinetic simulations, in a range of pressures from 10 Pa to 100 Pa. Values of the DC self-bias were determined, and spatio-temporal excitation rates derived, from phase resolved optical emission spectroscopy. The spatio-temporal distributions of the excitation rate obtained from experiments are well reproduced by simulations. By changing the number of consecutive harmonics included in the driving voltage waveform, or by changing the gas pressure, we induced transitions of the discharge electron heating mode between the drift-ambipolar mode and the α-mode (low pressure electropositive discharge mode). Changing the number of harmonics in the waveform had a strong effect on the electronegativity of the discharge, on the generation of the DC self-bias and on the control of ion properties at the electrodes, both for pulse, as well as sawtooth driving voltage waveforms. The effect of the surface quenching rate of oxygen singlet delta metastable molecules on the spatio-temporal excitation patterns was also investigated in detail [147]. As in the case for CF_4 the density of negatively charged atomic ions was found much larger than the electron density and depended on the type of electrode material. Fig. 40reveals the densities of selected plasma species for the case of an oxygen plasma at 40 Pa driven by a capacitively coupled RF discharge.

Oxygen plasma is standardly used for tailoring surface properties of polymer materials. For this purpose, one can apply plasma in different discharge configurations. Particularly popular are electrode-less low pressure discharges where the dissociation fraction is high due to low loss of atoms by heterogeneous surface recombination on dielectric surfaces. Reactive oxygen species readily interact with polymers and cause at least two effects: functionalization with polar groups and nanostructuring. Both effects cause suitable surface conditions for capture of UV-responsive microcapsules which provide an excellent UV protection of light cotton fabrics [148].

Although the majority of research is still concentrated a “standard” reactive gases such as oxygen, nitrogen, hydrogen, hydrocarbons and fluorinated hydrocarbons other gases are becoming increasingly popular since they may assure a materials surface finish unachievable by plasma created in standard gases. Examples include sulfur-containing gases that may serve as a source of sulfur functional groups that are particularly useful when mimicking surface properties of biocompatible coatings. The properties of plasma created in sulfur dioxide have been studied for the case of inductively coupled RF discharge, which can operate in two modes (E or H mode). The E mode appears at a low input power, where plasma is sustained by a capacitive coupling. With the increasing input power, an abrupt transition to the H mode appears, where an inductive coupling prevails. The E mode is characterized by a low light emission, whereas in the H mode much brighter light emission appears and plasma shrinks to a small volume inside the coil. The transition between E and H modes have been elaborated using optical and mass spectroscopy techniques [149]. Fig. 41 reveals the emissivity of selected radicals as determined by optical emission spectroscopy versus the nominal power of the RF generator which was operating at the standard frequency of 27.12 MHz. The plasma luminosity increases by orders of magnitude at the abrupt transition from the E to H mode, but the emissivity from particular radicals varies significantly. The relative intensity of the S radiative transitions is rather poor in the E mode indicating incomplete dissociation of SO_2 molecules. In the H mode, however, the intensity increased by over four orders of magnitude and becomes comparable to the intensity of oxygen atomic lines. Such plasmas are suitable for modification of polymer surfaces in order to make optimal conditions for cell proliferation on polymeric scaffolds [150].

12.2. *Atmospheric-pressure plasma*

Modern and extremely challenging applications of gaseous plasmas are for modification of living matter such as biological cells, tissues, seeds or even whole plants [151]. The niches of plasma medicine and agriculture are among the most rapidly growing interdisciplinary scientific fields. The living matter is often in a liquid medium, so conventional low-pressure treatments are limited to samples that stand evacuation to appropriate pressure. The physics and chemistry of non-equilibrium atmospheric pressure gaseous plasmas are far more complex. Fig. 42 represents the interaction of atmospheric plasma with

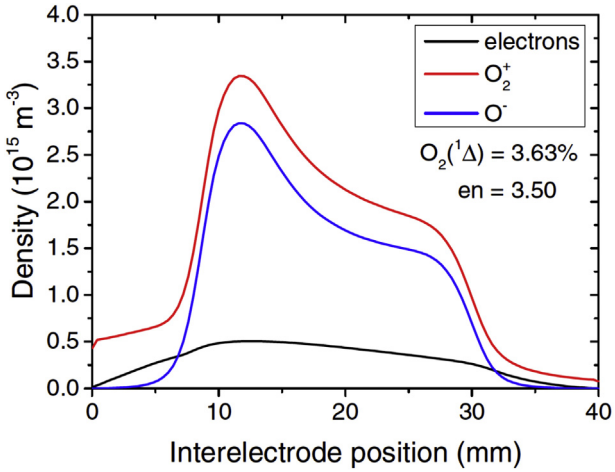

Fig. 40. The distribution of reactive oxygen species in a low-pressure capacitively coupled RF discharge [147]. “en” denotes the global electronegativity.

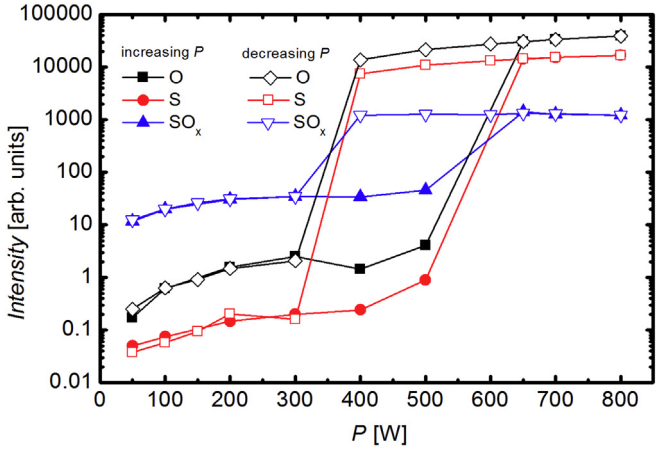

Fig. 41. The hysteresis behavior of neutral radicals created in are SO_2 plasma at the transition of the ICP from E to H modes [149]. Reproduced from Ref. [149], with the permission of AIP Publishing.

biological material in a schematic manner. Gaseous plasmas are typically sustained a few millimeters or even centimeters above the biological tissue. Charged particles gain energy in the region where a strong electric field is present. Plasma is often sustained in a noble gas with small quantities of a reactive gas, typically oxygen [152]. Then there is the effluent region where the plasma plume mixes with surrounding atmosphere (typically humid air) where rich gas-phase chemistry occurs. The plasma plume may, or may not, touch the liquid surface. The reactive species dissolve in the liquid [153] (often a suitable medium for cell culturing) and finally the species interact with biological matter. The interactions last over a time scale ranging from picoseconds to days. Namely, the electron dynamics are extremely fast due to their high mobility (low mass). The time between two subsequent collisions of electrons at atmospheric pressure is of the order of 10^{-12} s. The ion dynamics are slower since the ion mass is roughly four orders of magnitude larger. Plasma chemistry, i.e. establishment of stationary concentration of reactive plasma species, occurs over a time scale of μs to almost s. The treatment time is typically from seconds up minutes, but the resultant modification of biological matter may take days.

Characterization of atmospheric plasmas is still challenging due to huge gradients of reactive gaseous species. Techniques that have been developed for characterization of low-pressure plasma often fail, thus more sophisticated ones have to be invented. One recently applied technique is based on synchrotron radiation. As explained in Section 4, the synchrotron beamlines provide highly brilliant VUV light of adjustable photon energy at high fluxes. This allows for detection of atomic species by optical absorption. The atmospheric-pressure chamber containing gaseous plasma was mounted into an ultra-high vacuum chamber at DESIRS beamline of Soleil synchrotron. The VUV passed from the beamline through the atmospheric-pressure plasma via VUV-transparent windows as shown in Fig. 43. A VUV Fourier-transform spectrometer was used to measure the density of O and N atoms in helium plasma of synthetic air admixture. A maximum in the O atom concentration of 9×10^{20} m^{-3} was found at air admixtures of 0.35 vol % [155].

An alternative method for determination of the atomic oxygen density is Two-photon Absorption Laser Induced Fluorescence (TALIF). The technique has been validated for low-pressure plasmas (and especially afterglows) long ago, but characterization of atmospheric-pressure plasma is more demanding for many reasons including the quenching of laser-excited atoms due to collisions with other gaseous molecules. To overcome this obstacle, picosecond lasers should be applied. A suitable setup for such experiments is presented in Fig. 44. The duration of laser pulses was 30 ps and the repetition time 0.1 s. Two photon excitation of O atoms in the ground state was achieved through absorption of the photons at wavelength 225.65 nm. Fluorescence was

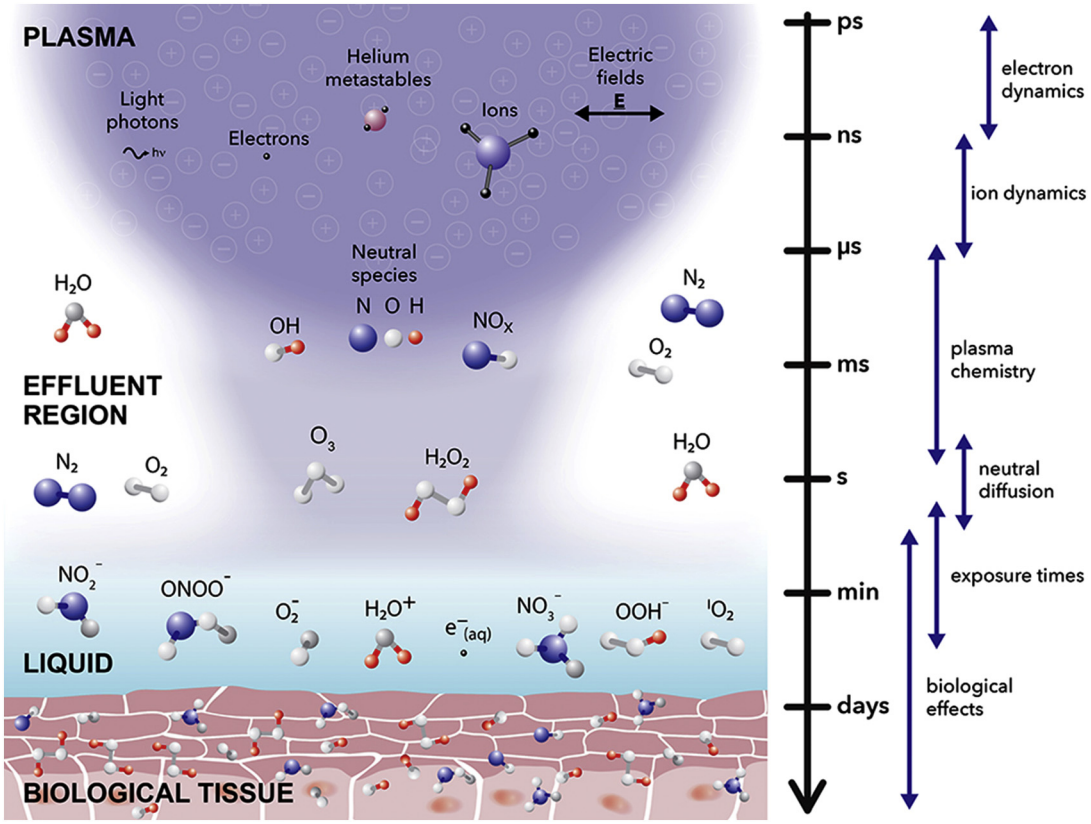

Fig. 42. Schematic of the interaction between atmospheric plasma and biological matter (modified from Ref. [154]).

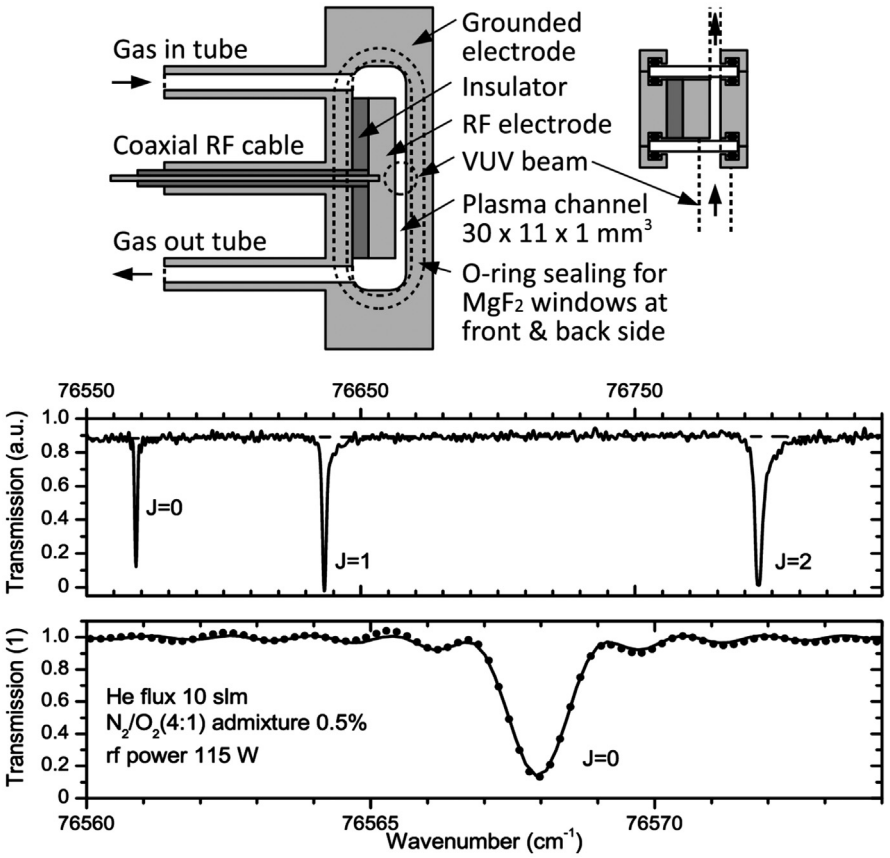

Fig. 43. The configuration of a discharge chamber mounted into a synchrotron beamline and absorption spectra of atomic oxygen [156].

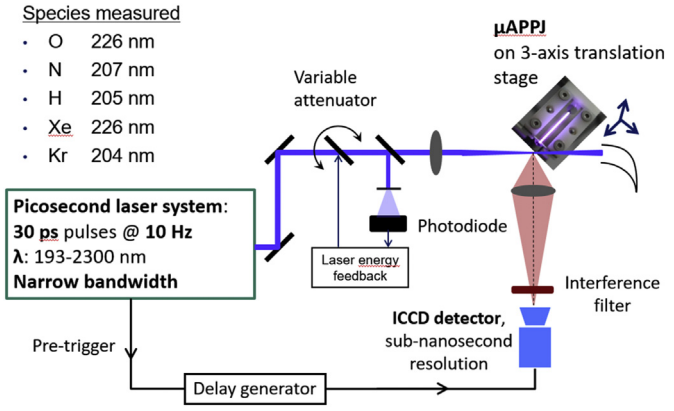

Fig. 44. An experimental setup suitable for measuring absolute densities of atomic species in atmospheric-pressure plasmas.

detected at a wavelength of 844.87 nm, which corresponds to a transition from 3p ^2P_j to 3 s ^3S excited states of oxygen atoms. The results using this technique have been compared to VUV absorption using synchrotron radiation and the discrepancy was only up to about 20%. All these experiments were performed in plasmas sustained by RF in a gap of 1 mm where the plasma is visually homogeneous.

Picosecond TALIF is also a suitable technique for characterization of plasma plumes where strong gradients (both longitudinal and radial) are observable even with a naked eye. Fig. 45 represents two-dimensional images of the O atom density in plasma plumes created due to atmospheric pressure in oxygen and synthetic air. Huge gradients are explained by the loss of O atoms due to three-body collisions that represent the major mechanism for recombination of neutral atoms to parent molecules at atmospheric pressure.

The maximum O atom density in non-equilibrium atmospheric-pressure plasmas as determined by both methods is about 1×10^{21} m^{-3}. This value is also typical for low-pressure plasmas sustained in pure oxygen by capacitively coupling, but an order of magnitude lower than in inductively coupled plasmas even though such plasmas are sustained in the E mode where the capacitive component prevails. The superior properties of plasmas created in electrodeless discharges has been explained by the absence of metallic materials facing the plasma which represent a sink for O atoms due to heterogeneous surface recombination [156].

13. Pressure metrology

The treatment of advanced materials, molecular-electronics, and characterization of synthesized materials is often accomplished under low-pressure conditions. Pressure metrology therefore remains a crucial scientific activity and researchers are seeking accurate, reliable, fast and cost-effective devices for pressure measurement [157].

NIST has recently developed a technique to determine pressure using laser interferometry to measure the pressure-dependent refractivity of a gas. As discussed below, when this new absolute pressure measurement technology is compared to legacy, but presently used,

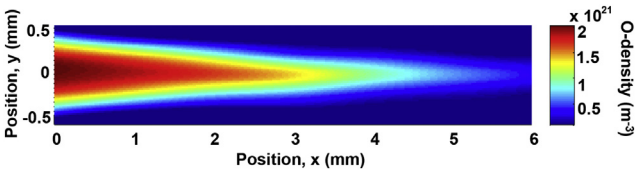

Fig. 45. The O-atom density in a plasma plume as determined by picosecond TALIF for oxygen.

high accuracy pressure measurement techniques, it is clear that optical interferometry is the future of gas pressure measurement in the pressure range of 1 Pa to 360 kPa, and perhaps beyond. Several other research groups have now begun programs to develop similar absolute pressure standards based upon the optical interferometry method [157]. An outline of the future of this technique is provided and discussed in detail.

The world's first gas pressure measurement was made in 1643 with Evangelista Torricelli's invention of the mercury barometer/manometer. Modern manometers which utilize ultrasonic interferometry to measure the column height, such as the Ultrasonic Interferometer Manometer (UIM), can obtain uncertainties between 10 parts in 10^6 Pa/Pa and 1000 parts in 10^6 Pa/Pa over a pressure range of 1 Pa to 100 kPa [158–161]. After nearly 400 years we finally have a technique that could break the reliance on liquid mercury for the highest accuracy pressure measurements.

Optical pressure measurement techniques have several advantages over manometers and other high accuracy mechanical and hydrostatic measurement techniques. These include: speed of measurement, vibration sensitivity, size/weight, safety concerns over the use of neurotoxin (mercury), and pressure range. The measurement technique uses a dual-cavity laser refractometer to measure the change in refractivity $(n-1)$ when gas is added to one of the cavities. This is proportional to the number density of the gas and thermal energy, k_BT. The technique utilizes interferometry (and laser wavelength) to determine the optical length of a Fabry–Perot (FP) cavity [162]. The laser light travels more slowly as more gas molecules are added to the cavity, resulting in an apparent optical path length change. From this, we can determine pressure from the relation:

$$p \propto (n-1)k_BT, \tag{5}$$

where p is the pressure, k_B is the Boltzmann constant, and T is the thermodynamic temperature. The refractivity is dependent on the gas species and the value of the refractivity of the gas can be a large part of the total uncertainty if it is not sufficiently known from experimental methods or fundamental quantum-chemistry calculations. Since this technique is based on a property of the gas, it can be easily miniaturized and requires no recalibration once the refractive index for a given gas is known and the temperature is measured at time of use.

NIST is constructing two different refractometer standards which will be described in the following sections. These will be contrasted with the current pressure standard technology. Additionally, the benefits and changes from current measurement methods will be discussed along with an outline for future improvements and related technologies.

13.1. Design of a pressure standard

13.1.1. Optical pressure measurement design

The heart of the new optical pressure measurement technique contains two cavities with mirrors at either end to form a dual Fabry–Perot (FP) interferometer. One of the cavities is at vacuum, and the other is filled with a gas. In principle, for an ideal system, the FP that remains at vacuum will determine the actual length of the cavity and the FP that is filled with gas will determine an apparent length of the cavity due to changes in refractivity.

To determine the apparent length, each FP has a laser that is frequency tuned to be resonant within the cavity. This method can achieve resolution in cavity length of better than 0.5 pm. This sensitivity is critical because the FP will only see a change of 0.4 nm/Pa. In contrast, the manometer sees 7600 nm/Pa of physical change in the mercury column height. Another way to state this is that at a pressure of 1 kPa and a desired accuracy of 0.0001%, we need to be able to measure better than 3 pm on a cavity length of 1 m. Since we care more about the ratio of reference cavity length to pressure cavity length, we do not calculate length but simplify the system to a determination of the

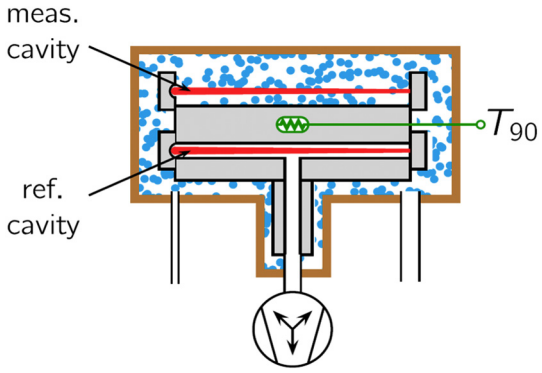

Fig. 46. FLOC diagram.

effective fractional change in cavity resonance frequency relative to the cavity free spectral range ν, $\Delta f/\nu$, which is equal in magnitude to the fractional length change $\Delta L/L$ of the cavity [162].

NIST devised and constructed three identical cavities of the design that we refer to as the Fixed Length Optical Cavity (FLOC). The FLOC design consists of a 15 cm long piece of Ultra Low Expansion (ULE) glass that has two main functions (1) separate the two cavities, gas from vacuum, and (2) mount the mirrors on a stable platform. The mirrors are partially reflective (reflectivity around 99.7%) and are silicate-bonded to the ULE glass to form the cavities as shown in Fig. 46. The vacuum or reference cavity consists of a hole drilled through the ULE and capped at both ends by the mirrors. A glass tube is bonded to the bottom of the cavity to allow for it to be continuously pumped to vacuum pressure below 1×10^{-5} Pa. The pressure or measurement cavity is a channel that is open to gas flow. This allows for easier flow of gas through the cavity and better thermal performance.

The gas is contained by a copper chamber (golden color boundary in Fig. 46) that helps to stabilize the temporal and special temperature fluctuations. From the ideal gas law, we know that temperature and pressure are proportional and that the uncertainty in the temperature of the gas is very critical. Stability of better than 0.3 mK is required to achieve our desired accuracy. To achieve this, the copper chamber was placed in an aluminum temperature controller (not shown in figure). The temperature was controlled to 30 °C and was monitored over 100 h and showing stability better than 0.1 mK (see Fig. 47).

Tunable HeNe lasers were chosen for the light source due to their narrow linewidth, relatively low cost, and low power output (inherently safe). Additionally, a HeNe laser frequency is known to within a GHz without calibration [163]. The frequency of HeNe lasers may be tuned by controlling the laser tube heaters with an analog signal. For faster

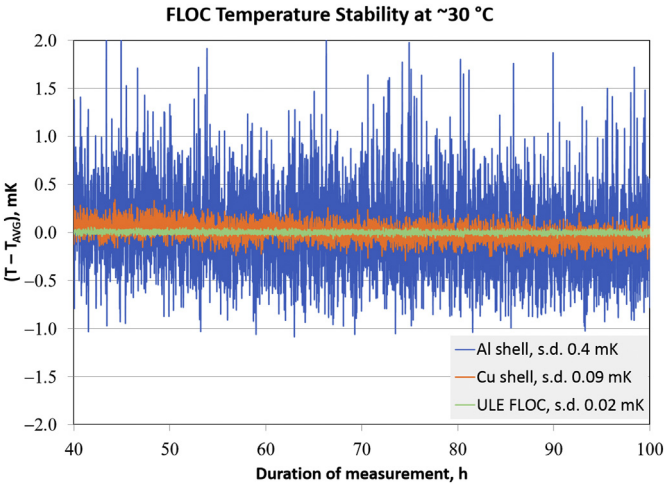

Fig. 47. FLOC thermal performance.

response tuning, acousto-optic modulators (AOM) are used. On the laser output of the cavity, an intensity detector feeds an error signal back to the AOM/Laser to achieve and maintain cavity resonance.

The FLOC suffers from one major limitation which is the physical bending and bulk compression caused by pressure applied to the outside of the ULE glass cavities. This force applies a bending moment to the cavities resulting in a change in length that is not due to the refraction change. This distortion characteristic of each FP cavity-based refractometer is unique, but once determined has been shown to be stable and reproducible over time. The FLOC bending distortion was modeled using Finite Element Analysis (FEA), as shown in Fig. 48, however, due to the high uncertainty of FEA, the best way to correct such distortions is to measure them individually. For the reference cavity, the combined effect of bulk compression of the glass and mirror bending can be determined by measuring the resonance frequency change as a function of applied pressure. For the measurement cavity, the refractivity must be compared using a gas of known index and a primary pressure measurement device. Using this technique, the distortion effects on the pressure uncertainty were kept below 2 parts in 10^6 Pa/Pa.

The calculation of pressure in the FLOC can be described by:

$$p_{FLOC} = \frac{1}{c_1 - d_m - d_r}\left(\frac{\Delta f}{\nu}\right) - \frac{c_2 - c_1 d_m}{(c_1 - d_m - d_r)^3}\left(\frac{\Delta f}{\nu}\right)^2 + \frac{2(c_2 - c_1 d_m)^2 - c_3(c_1 - d_m - d_r)}{(c_1 - d_m - d_r)^5}\left(\frac{\Delta f}{\nu}\right)^3, \quad (6)$$

where $\Delta f/\nu$ is the effective fractional change in cavity resonance frequency, and d_m and d_r are distortion terms for the measurement and reference cavities. c_1, c_2, and c_3 are defined by:

$$c_1 = \frac{3}{2k_B T} A_R, \quad (7)$$

$$c_2 = \frac{3}{8(k_B T)^2}(A_R^2 - 4A_R B_p + 4B_R), \quad (8)$$

$$c_3 = \frac{3}{16(k_B T)^3}(5A_R^3 - 4A_R^2 B_p + 16A_R B_p^2 + 4A_R B_p - 16B_p B_R - 8A_R C_p + 8C_R), \quad (9)$$

where A_R, B_R, C_R are the refractivity virial coefficients and B_p, C_p are the density virial coefficients. It is clear that the FLOC uncertainty is directly determined by the refractivity of the gas as will be discussed in the next section. The uncertainty was calculated in [164] as:

$$U(p_{FLOC}) = \sqrt{(2 \times 10^{-3})^2 + (8.8 \times 10^{-6} \times p)^2}, \quad (10)$$

where $U(p_{FLOC})$ is the expanded uncertainty in Pa, and p is the pressure in Pa, for pressure measurements from 0.1 Pa to 360 kPa. The uncertainty differences between FLOC and UIM are plotted in Fig. 49.

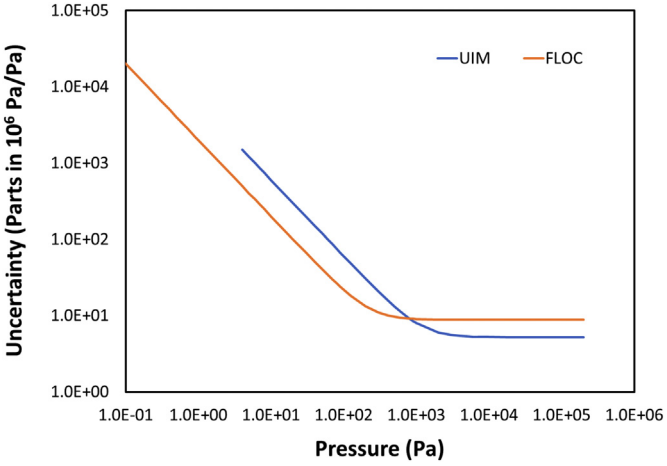

Fig. 49. FLOC vs UIM uncertainty comparison.

13.2. Determination of gas refractivity

The gas refractivity and density virial coefficients must be well known to achieve very high accuracy pressure measurements. Due to its simple electron structure and limited number of isotopes, helium's refractivity and density virial coefficients can be calculated through quantum mechanics as done by Puchalski [165]. Even with helium, the calculations required significant computer processing capabilities to achieve our desired uncertainty of < 0.5 parts in 10^6 Pa/Pa. This low uncertainty is critical for us to achieve uncertainties in pressure below that of the UIM and to provide a direct link to the International System

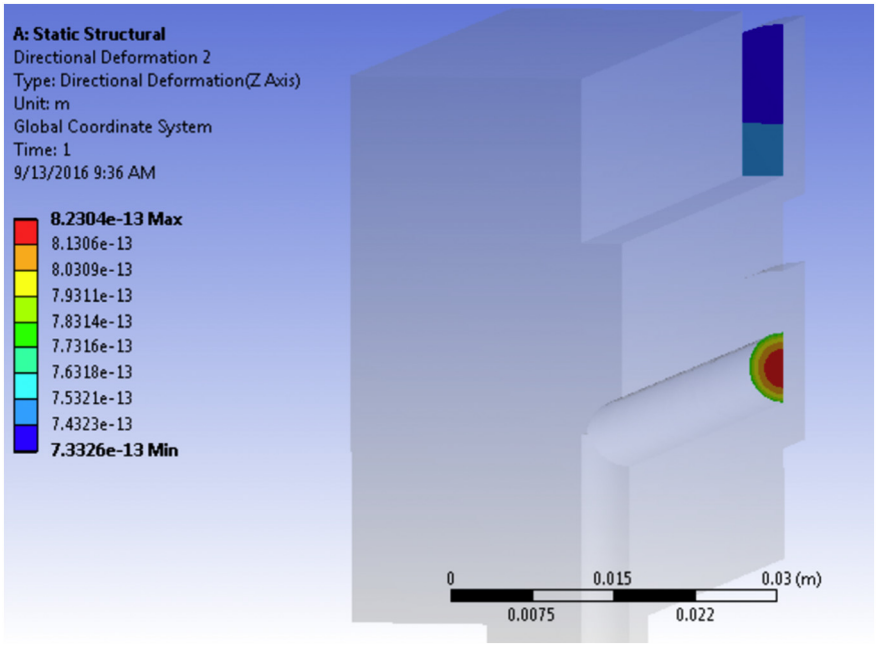

Fig. 48. FLOC pressure distortion.

of Units (SI) through quantum theory.

For gases like nitrogen (the most commonly used pressure calibration gas), the electron structure is far too complicated to calculate the refractivity directly. We must measure the virial coefficients using a device such as the FLOC and a stable pressure standard such as the UIM or a high accuracy piston gauge [162]. This can be accomplished for any pure gas such as nitrogen, argon, xenon, etc. However, a determination must be made relating the change in gas refractivity to the change in gas pressure before it can be used to make optical pressure measurements. The uncertainty in this measurement is directly related to the uncertainty in the pressure standard used, so we are limited in accuracy using this method. For example, the uncertainty in Eq. (11) is using nitrogen's virial coefficients as determined by the UIM and therefore has an uncertainty of 7.3 parts in 10^{-6} Pa/Pa associated with A_R. A_R is the limiting constraint at pressures near 100 kPa where we can see that the UIM provides a slightly lower uncertainty (see Fig. 49).

The uncertainty in the UIM, and the uncertainty in the FLOC, are clearly intertwined; however, NIST is constructing a device to produce measurements of refractive index without the need for the UIM or any other absolute pressure measurement. This device, referred to as the Variable Length Optical Cavity (VLOC), operates on principles similar to the FLOC; however, there are key differences. First, the VLOC has four cavities (three positioned at equal radius from a central cavity) as shown in Fig. 50. The central cavity, or measurement cavity, will be exposed to a gas at a constant pressure, whereas the outer cavities will be at vacuum. The four cavity mirrors on each end plate will be mounted on a monolithic piece to allow for equal displacement of all cavities simultaneously as the cavity is expanded/contracted.

The foremost benefit of the VLOC is the ability to change the length of the FP cavity without distortions. This gives us the ability to make a measurement of the refractivity in the measurement cavity, then increase the cavity length and take a second measurement. The reference cavities provide the displacement distance ($L_2 - L_1$), and the measurement cavities provide the optical path length (OPL) at the two positions (OPL_2, OPL_1). Subtracting the measurements at two different lengths results in the refractive index as described by:

$$n = \frac{OPL_2 - OPL_1}{L_2 - L_1}, \tag{11}$$

This method has the benefit of eliminating most errors that are common to both measurement positions. For example, distortion of the mirror due to pressure is the same at both positions, so the errors cancel. This will allow us to achieve uncertainties for the helium refractivity that are on the order of 1 part in 10^6 [166] and reduce the uncertainties for FLOC pressure measurements using nitrogen by a factor of five or more. The VLOC allows us a primary realization of the Pascal that is at least two times more accurate than the UIM. This will be the essential cornerstone to eliminating the use of mercury in pressure standards.

The VLOC design, as shown in Fig. 51, is currently under construction. The colors are used in the image to show each individual part, and clearly indicate the complexity of the apparatus in comparison to the conceptual drawing. Most of the complication comes from moving the entire cavity 15 cm to a new position without introducing errors and from maintaining the gas purity. The purity must be maintained to 50 nmol/mol to achieve the desired results.

The VLOC is critical in that it provides a method of precisely measuring refractivity of gases such as nitrogen that currently cannot accurately be calculated from first principles quantum chemistry calculations. However, once the VLOC makes an accurate measurement of the nitrogen refractive index, the data will become the traceability chain for all FLOC optical pressure measurement devices around the world. This will completely revolutionize the calibration of pressure instruments. Instead of relying on high accuracy calibrations against primary standards (such as the UIM), researchers or other end users can design (or, perhaps one day, purchase a FLOC) to calibrate their own devices. This will result in a significant savings in cost and efficiency because the end user's FLOC would not require any calibration. This will drastically reduce lifetime operating costs for pressure sensor calibrations. In addition, in many cases it may reduce the calibration uncertainty of the user's pressure sensors.

13.3. Future applications of the FLOC

The performance of the FLOC has demonstrated several advantages of optical pressure measurement versus manometry. Another improvement the FLOC technique can offer is a significant increase in measurement speed. The FLOC can make pressure measurements in the kHz range and can easily make measurements in dynamic pressure environments and would only be limited by the ability to measure gas temperature. In contrast, the UIM requires 45 s to collect one reading. This capability coupled with a dynamic feedback loop could improve process control and help speed up any manufacturing process requiring precise pressure control.

Another application of the FLOC technique is as a real-time measurement of refractivity, using the same device. Refractive index is very sensitive to gas composition and as such, it can be used for atmospheric monitoring or even as a humidity sensor. Additionally, for high precision interferometry measurements in air, corrections to the index are made by making pressure, temperature, gas composition, and humidity measurements at current barometric conditions. However, using a FLOC we can directly measure and correct the laser wavelengths with significantly higher accuracy. This would enable length measurements, such as on a factory floor, with uncertainty as low as 2 parts in 10^8 m/m.

Additionally, if a user was operating with a binary gas mixture, a FLOC could determine the precise ratio of the two partial pressures (assuming the refractivity of both gases is known). For example, this could be used for precision doping of gases for semiconductor fabrication, or to determine gas composition in natural gas pipelines. This method could also be used for calibration of humidity sensors (H_2O + N_2). The accuracy of these binary measurements can be as good as 1 part in 10^6.

The FLOC is not only a method to determine pressure, but it can also be used to measure temperature and calibrate high accuracy thermometers. This is clear from Eq. (5), if the pressure in the FLOC is determined using a separate pressure measurement device, the FLOC can be used as a temperature standard. For example, with a piston gauge, this standard would be accurate to better than 0.5 mK at 300 K and capable of calibrating high accuracy platinum resistance thermometers. It should be noted that the FLOC measures thermodynamic temperature, and not the international temperature scale of 1990 (ITS-90) which is a scale based on fixed points and interpolating devices.

There are also many improvements that can be made to advance the current FLOC pressure capabilities, and many can be made with current technology. One of the most exciting is that, since the physics does not dictate size, the FLOC can be reduced to fit into a small form similar in size to today's high accuracy sensors (a 10 cm cube, plus electronics). Another exciting aspect is the pressure range of the FLOC technique. Our experiments have shown resolution at pressures as low as 10^{-4} Pa. We also believe that the technique will work up to at least 10^6 Pa (and even higher if better virial coefficients can be determined). As shown in

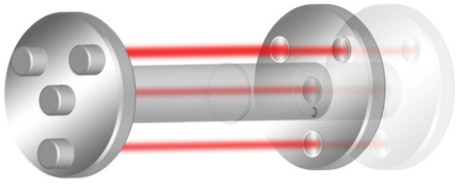

Fig. 50. VLOC conceptual drawing.

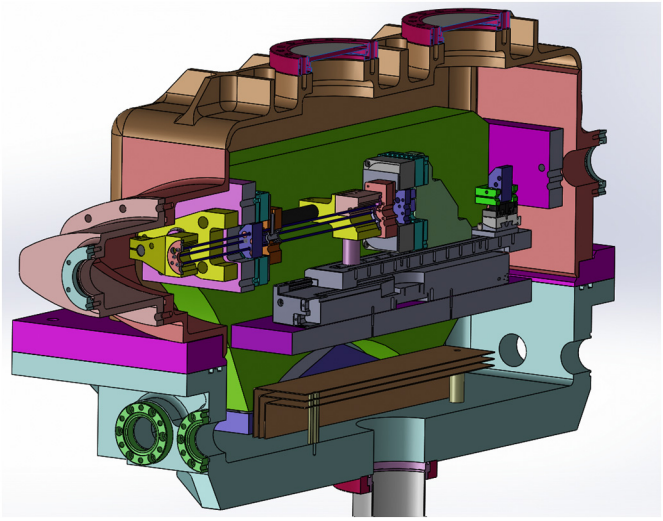

Fig. 51. VLOC 3-D drawing.

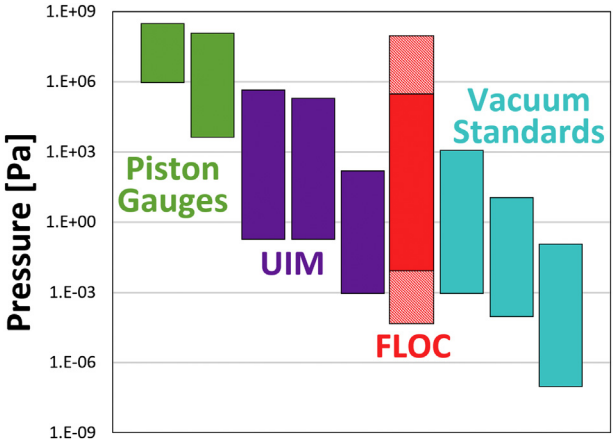

Fig. 52. NIST pressure and vacuum standards.

Fig. 52, this pressure range is currently covered by six different primary standards. The FLOC is depicted in Fig. 52 to show current capabilities with the hashed lines representing future improvements. Implementation of the FLOC will significantly reduce the number of standards previously required to cover same pressure range, potentially reducing costs in calibration and maintenance. The FLOC could drastically change metrology in many different fields in the next 10 years.

In conclusion, NIST has designed and tested the first primary standard that measures pressure using light. This device is redefining how we measure pressure. The technology is significantly smaller and more robust than manometers. The FLOC also has a compact design that can evolve into a portable standard and a commercial product; for many end-users, owning a primary standard can be a significant cost savings because it eliminates the need to send pressure sensors to external laboratories for re-calibration. These significant advantages over the mercury-based technology, along with the fact that the FLOC currently has an uncertainty equivalent to the UIM and is likely to surpass this uncertainty in the next few years, makes the FLOC an excellent manometer replacement.

In the near future, the FLOC technology will also expand into other metrology fields and will significantly change how the industry calibrates gauges/sensors. One standard will enable users to calibrate thermometers, pressure sensors, gas species detectors, humidity sensors. That same device could also be used to verify gas quality of systems or verify that a purchased tank of high purity gas meets specifications.

Refractometry is the future of pressure measurement. The world continues to move away from artifact based standards such as the kilogram, and more standards have become quantum or photonic based standards. Refractivity is enabling the revolution for gas pressure metrology away from artifact based standards and physical calibrations to a quantum based refractometer where pressure can be realized anywhere you have a FLOC.

14. Cold atom vacuum standard

NIST is presently developing a new type of vacuum standard that significantly departs from traditional vacuum metrology. The cold atom vacuum standard, or CAVS, will nominally cover the pressure range of 10^{-6} Pa to 10^{-10} Pa (ultra-high vacuum, UHV, to extreme-high vacuum, XHV) which, at present, is not covered by any primary standard. The CAVS is an absolute sensor of vacuum, thus departing from ionization gauges (which require calibration and are not absolute sensors) and from dynamic or static expansion standards (which are neither primary standards nor gas sensors). The CAVS is based on the loss-rate of ultra-cold atoms from a magnetic trap. This rate is largely determined by collisions of the background gas in the vacuum with the magnetically trapped sensor atoms. In UHV and XHV, the background gas in mostly comprised of H_2. We are building a low-uncertainty laboratory-scale CAVS that will use Li atoms as the sensor atoms and will therefore be based on a rate coefficient for Li + H_2, which is a fundamental atomic property. The measurement of the loss-rate is directly traceable to time. The rate coefficient, or thermalized collision cross section, for the Li + H_2 system will be determined from ab initio calculations presently underway at NIST. Rate coefficients for collisions of ultra-cold atoms with other gases of practical interest (e.g. N_2, H_2O, He, Ar, CO_2, etc.) will be determined experimentally or theoretically, allowing relative gas sensitivity factors to be determined. In parallel to creating a laboratory-scale CAVS, we are developing a portable chip-scale platform based on ultra-cold Li or Rb. Such a platform will not only allow the creation of a robust portable CAVS, but will also allow for the creation of other robust sensors based on cold atom technology, such as inertial sensors and gravimeters.

It has long been known that the loss-rate of ultra-cold atoms from a magnetic trap is largely determined by collisions of the background gas in the vacuum with the ultra-cold atom. However, there are other mechanisms which lead to the loss of atoms from the trap, such as two-body and three-body collisions of cold-atoms within the trap, losses due to non-adiabatic spin-flips, or heating due to trap fluctuations. Eliminating or quantifying these loss rates is essential to creating a laboratory-scale CAVS. Theoretic determination of the rate-coefficients for the Li + H_2 system is also crucial and will serve as a basis for the experimental determination of Li and Rb loss-rates for a variety of background gases. In the following, we focus discussion on the laboratory-scale CAVS apparatus and the experimental plan for determining the loss-rates.

14.1. CAVS apparatus

Many of the techniques used to laser cool and trap atoms were pioneered at NIST and are now the basis of the well-established field of cold-atom physics. Here we give only a brief and simplified explanation of the cooling and trapping; the interested reader is referred to more fundamental texts [167]. The first step to creating the CAVS is to cool sensor atoms (alkali atoms will become vacuum sensors in subsequent steps) to sub-millikelvin temperatures using laser-cooling. Laser cooling of atoms can be understood with the aid of Fig. 53, which depicts an idealized two-state atom of energy E_0 and E_1, the difference of which results in a resonant transition of frequency $\omega_0 = (E_1 - E_0)/\hbar$. By applying laser light with a frequency $\omega = \omega_0$, one can drive the atom into the excited state E_1. Once excited, the atom will return to the ground state by emitting a photon of frequency ω_0 in a random direction.

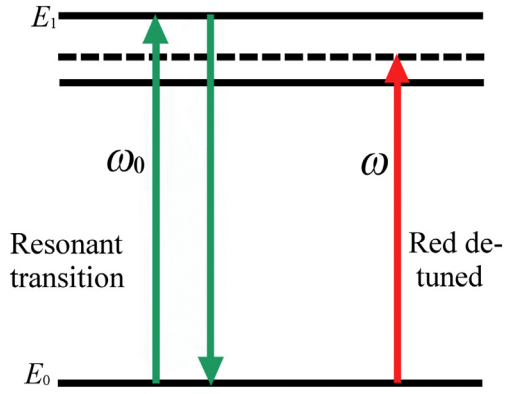

Fig. 53. Schematic diagram of energy levels in a two-state atom, resonant photons ω_0 and red-detuned photon ω.

Because each photon carries momentum $p = \frac{h}{\lambda}$, each time the atom scatters a photon it receives a momentum kick. On resonance, this process does not lead to cooling. Instead, to cool the atoms, one takes advantage of the Doppler effect. If an atom of velocity v moves towards a laser beam of frequency ω, the atom will see a laser frequency that is blue shifted (higher frequency), i.e. a Doppler shift, by $\frac{v}{c}\omega$. Thus, by tuning the laser frequency such that $\omega < \omega_0$, one can ensure that the atom only absorbs light from the laser and receives the corresponding momentum kick if it is moving in the direction opposite the laser beam. In this case, the laser applies a force on the atom that is directly proportional to its velocity. By arranging six laser beams to impinge upon the atom in six directions, a strong damping force is created in all directions and the atoms are cooled. This arrangement is often called an optical molasses and creates a velocity-dependent force in three dimensions.

Because this force is proportional only to the velocity of the atoms, the cooled atoms will eventually diffuse out and are therefore not trapped in space. To apply a force that is also dependent on an atom's position, one employs the Zeeman effect. The energy levels of atoms placed in a weak magnetic field will experience a shift proportional to the field. The direction of the energy shift (to a higher or lower energy level compared to that in zero magnetic field) will depend on the direction of the magnetic field relative to the angular momentum of the atom along the field direction. A magnetic field gradient can therefore be used to shift the atomic states into resonance with the six laser beams and create a position-dependent force. Suppose the laser is, again, tuned below the resonant frequency at zero field. As atoms move away from zero field near the center of the trap, the energy level will shift causing the laser frequency to be resonant and the atom will absorb more light. Combining the optical molasses with a magnetic field gradient produces creates a magneto-optical trap (MOT). The MOT can be used to trap and cool atoms to the sub-millikelvin temperatures required for the CAVS. Once cooled, the atoms are transferred from the MOT to a shallow magnetic trap. The magnetic trap is an arrangement of inhomogeneous magnetic fields used to trap neutral atoms with non-zero angular momentum. (For a sense of scale, typical magnetic field gradients in MOTs for Rb are about 15 G/cm and typical magnetic traps require gradients of over 300 G/cm). Once in the magnetic trap, the only way for atoms to leave the trap (ideally) is due to collisions with molecules in the background gas.

Many atoms can be laser-cooled and magnetically trapped, but the most obvious candidates for sensor atoms in the CAVS are alkali metal atoms such as Li or Rb. The hydrogen-like atomic structure makes these atoms easy to laser cool. Moreover, lasers that operate at red and near-infrared wavelengths, which are near, for example, the cooling transitions of Li and Rb, can be reasonably low cost. Fig. 54 illustrates the concept of the CAVS design based on Li, and Fig. 55 shows the vacuum chamber in its present state of construction. There are two separate trap regions: a pre-cooling trap chamber, where the atoms are first cooled in a 2D (two-dimensional) MOT; and an XHV sensing trap chamber where the vacuum level is detected and the alkali background is kept to a very low density. Alkali atoms are first loaded into a pre-cooling 2D MOT where they are cooled in two spatial directions and drift along the third direction into the sensor chamber. The pre-cooled atoms pass through a small differential pumping tube (baffle tube) before entering the CAVS sensing trap chamber, where the cold atoms are captured in a second MOT and subsequently transferred to a magnetic trap with sub-millikelvin temperatures and densities of $\approx 10^{10}$ atoms/cm^3. The second MOT and the magnetic trap occupy the same space; cold-atom transfer occurs by turning off the MOT lasers and turning on the magnetic field of the trap. The cold atoms are now sensing vacuum pressure as they are ejected from the shallow magnetic trap by collisions with background molecules. After a time, Δt, the atoms are imaged through absorption imaging: a well-understood technique in which the atoms are illuminated by a resonant laser beam, scatter that light and cast a shadow. This shadow is imaged with a camera and gives a measure of the population of atoms that remain in the trap. The initial number of cold atoms loaded into the shallow magnetic trap is similarly determined. The loss rate Γ is calculated from the fractional change in the cold-atom number, and the background gas number density is given by $n = \Gamma/K_{loss}$, where $K_{loss} = \langle v\sigma \rangle$ is the thermally averaged loss-rate coefficient for atom loss from the trap. Here σ is a collision cross section and v is the collision velocity. The CAVS traps can be re-loaded from the pre-cooling 2D MOT and the process can be repeated for different Δt to improve statistical uncertainty. Nominally, we expect Δt to vary from seconds to tens of minutes over a pressure range of 10^{-6} to 10^{-10} Pa, based on $K_{\text{loss}} \sim 5 \times 10^{-9}$ cm^3/s. This is consistent with reported trap lifetimes of 300 s at 10^{-9} Pa [168]. Finally, gauges to be calibrated are attached to the test vacuum system and their reading is compared to the pressure determined by the CAVS. Alternatively, the CAVS could be used to monitor the vacuum level in the test vacuum system.

A critical challenge to creating the CAVS will be to experimentally and theoretically determine the loss rate coefficients K_{loss}, or cross sections σ, that lead to the loss of the sensor atoms from the trap due to collisions with the background gas in the vacuum. H_2 is the most common and therefore important residual gas (mostly due to outgassing from stainless steel and other metals) in UHV/XHV, and the laboratory-scale CAVS will ultimately be based on the precise knowledge of the Li + H_2 cross section. Other gases contribute as minor constituents of the background or—perhaps more importantly—as calibration or test gases, such as N_2, Ar, He, CO_2, CH_4, and He. Our own semi-classical estimates of rate coefficients for alkali-metal atoms colliding with various room temperature gases yield thermalized loss-rates on the order of 10^{-9} cm^3/s and show a 20% variation for the various constituent gases. Therefore, the CAVS is not expected to be strongly dependent on gas species for these common gases. Since, in the UHV/XHV environment, typically 95% of background gas is H_2, uncertainty in the exact composition of the remaining gas will only be a small contribution to the total uncertainty. When a process gas or calibration gas is leaked into the system, the gas composition will be exactly known.

We will experimentally determine cross sections for collisions of cold alkali-metal atoms with H_2 and many other molecules by building a dynamic expansion standard in tandem with the CAVS. This will allow

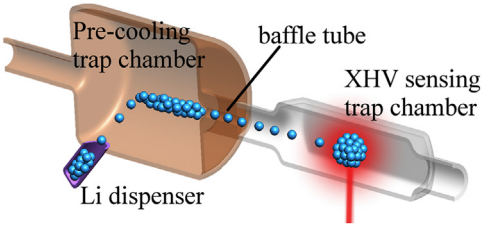

Fig. 54. Laboratory-scale CAVS with test vacuum.

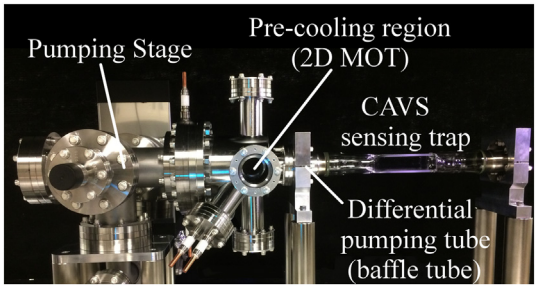

Fig. 55. The assembled CAVS vacuum chamber. Not shown are the optics systems and the magnetic field coils for the CAVS.

us to generate a known vacuum gas pressure in the CAVS. By setting a known pressure and measuring the trap lifetime, the cross sections leading to trap loss will be determined. Cross sections are a fundamental property and not pressure dependent, therefore their determination will be made at pressures of approximately 10^{-6} Pa, where the uncertainty of the generated pressure is expected to be < 2%. Moreover, the cross section determination will be made without reliance on a calibrated pressure gauge. With experimentally known cross sections, one can calculate relative sensitivity coefficients, and the SI traceability of the ab initio Li + H_2 system can be extended to the Li + X or Rb + X system (X is any gas) by these relative sensitivity coefficients. The details of this determination are beyond the scope of this work, but have been recently published by the authors [169]. With a trap lifetime measured with similar accuracy, this will be a state-of-the-art instrument for determining absolute collision cross sections.

To summarize, NIST is developing a program to create a primary vacuum sensor using an ultra-cold atom trap. Presently there is interest in this line of research by several groups [169–173]. The CAVS will be a primary standard based on an ab initio calculation of the Li + H_2 rate coefficient. Our measured collision rates will allow the traceable determination of relative gas sensitivity factors. Our ultimate goal will be to develop a robust deployable CAVS that can be used as an absolute vacuum sensor in a variety of environments.

15. Photonic sensors for temperature and pressure measurement

In recent years a wide variety of novel photonic measurement schemes for temperature monitoring have been proposed including the use of dyes [174,175], hydrogels [176–178], nitrogen vacancy (NV) diamond particles, fiber optic sensors [179–181], and on-chip integrated silicon photonic nanostructures [182–185]. At NIST, our efforts are aimed at developing novel photonic-based sensors and standards capable of outperforming legacy equipment [186]. The gamut of technologies under consideration runs from macroscale sapphire-based microwave whispering gallery mode resonator (WGMR) [187] to micron-scale fiber Bragg gratings (FBG), to novel nanoscale silicon photonic crystal cavities.

15.1. Fiber Bragg gratings

FBGs are narrow band filters fabricated using photo-sensitive optical fibers (e.g., H_2-loaded Ge-doped fibers) that are exposed to spatially varying UV light. This modifies the local structure of silica, creating a periodic variation in the local refractive index, which acts like a Bragg grating [179,188] with resonant wavelength being reflected, while non-resonant wavelengths pass through the fiber. The Bragg period is sensitive to both linear expansion of the grating and changes in refractive index. Changes in surrounding temperature change the effective grating period due to linear thermal expansion and the thermo-optic effect (refractive index due to temperature), resulting in a wavelength shift of ≈10 pm/°C [179,188]. In a recent study, over the temperature range of −40 °C to 120 °C, we demonstrated that a FBG has a measurement uncertainty of ≈ 0.5 °C, comparable to Type J thermocouples [189]. Embedding a FBG into structures such as 3D printed scaffolds [190] or aerospace-grade composite materials [191,192] can provide useful information on the structural properties of the material. However, as we have shown recently that covariance between temperature and strain response of FBG sensors is significant and limits their usefulness in such applications [190]. With careful experimental design however, such problems can be overcome.

15.2. Silicon photonics

Silicon photonic thermometers are another class of photonic thermometers that exploit a material's thermo-optic coefficient (TOC) to achieve high temperature sensitivity. Silicon's TOC is approximately 10× larger than silica's which enables temperature sensitivities that are nearly an order of magnitude greater than those of FBG sensors. These nanoscale sensors are fabricated using conventional silicon-on-insulator (SOI) CMOS-technology.

We have recently fabricated a wide variety of photonic temperature sensors, including Si waveguide Bragg reflectors (Si WBG) [193], ring resonators [182,194–197], and photonic crystal cavities [192]. In a recent study, we examined the temperature dependence of Si WBG over the temperature range of 5 °C to 160 °C, achieving a combined expanded measurement uncertainty (k = 2) of 1.25 °C, which is dominated by the uncertainty resulting from peak center measurement [193].

Lower uncertainties could be achieved in narrower band stop devices, such as ring resonators and photonic crystal cavities where measurement uncertainties of 50 mK and a noise floor of < 100 μK have been demonstrated [182]. Our device optimization work with ring resonators indicates that a zone of stability exists in the parameter space (*waveguide width* > 600 nm, *waveguide-ring gap* ≈ 130 nm and *ring radius* > 10 μm), where devices are less susceptible to routine fabrication errors. Consequently, these devices consistently show Q ≈ 10^4 and $\Delta\lambda/\Delta T$ ≈ 80 pm/°C [194,196]. Our preliminary results suggest that device interchangeability on the order of 0.1 °C can be readily achieved by implementing more rigorous process controls.

Our future work will focus on the fabrication and characterization of opto-mechanical devices. In opto-mechanical devices, the optical field of the cavity is coupled to its mechanical motion, providing a convenient means of probing the thermal Brownian motion of the cavity [196]. These devices would provide a convenient means of directly realizing thermodynamic temperature in the field and, by eliminating the need for a traceability chain, opto-mechanical devices of this type could lead to significant reductions in the cost of sensor ownership. In addition, the underlying photonic sensor technology will be easily adapted for (bio)chemical sensing by use of chemically selective cladding. For example, use of hydroscopic cladding material such as cellulose or polyimide would render a photonic sensor sensitive to humidity changes. Such a nanoscopic temperature and humidity sensor package could be useful in the study of biophysical processes such as pseudopolymorphic transitions in protein crystals [198].

15.3. Dynamic measurement of pressure

The dynamic measurement of pressure is critical for a wide variety of industrial processes, transportation, human health, ballistics, and the environment. For example, gasoline and diesel combustion engines experience maximum combustion pressures of 0.1 MPa to 10 MPa [199,200]. Gas turbines, used in aircraft and for power generation, operate at pressures of up to 4.5 MPa with a frequency spectrum of several hertz to 30 kHz [201]. Accurate measurement of dynamic pressure for combustion supports improved optimization of fuel efficiency. A major cause of traumatic brain injury for soldiers comes from exposure to blast waves, which typically have peak pressures of 1 MPa and rise times on the order of microseconds [202–205]. Medical

applications of dynamic pressure, such as blood pressure measurements, have a range of 10 kPa to 100 kPa, with a frequency content of the order of 100 Hz (a 1% time slice of a heart beat) [206]. Other applications include process control, rapid determination of crash severity to signal automotive airbag deployment system [207], energy production, large instrument control in manufacturing, and injection molding [208].

Unlike static or steady state pressure, there are no commercially-available SI-traceable calibration services for transient pressure; therefore the quantifiable uncertainties of transient pressure sensors and measurements are unknown [208]. Although many National Metrology Institutes have SI-traceable standards for acoustics, ultrasound, and vibration, these differ significantly from transient pressure measurements. Acoustic measurement calibrations typically span micropascal to tens of pascal. Although these measurements are made at relatively high frequencies (a few tens of kilohertz), the measurements are of highly repeatable sinusoidal waves enabling deep integration times. The examples listed above illustrate the range in transient pressure measurements which span tens of kilopascal to hundreds of megapascal. Additionally, these measurements are typically one-time events with bandwidths up to megahertz. Thus, creating these dynamic events reproducibly and then performing accurate characterization is extremely challenging.

There are currently no National Metrology Institutes that list a Calibration Measurement Capability (CMC) for dynamic pressure in the BIPM (Bureau International des Poids et Mesures) Key Comparison Database. An assumption is made that the sensor will have the same linear amplitude response to a rapid pressure change as it would to a steady-state pressure of the same magnitude, as long as the sensor's natural frequency far exceeds that of the generated pressure. Validating this assumption requires a transient pressure source of known (traceable) performance; however, over the dynamic pressure range of interest, such a standard does not exist. In addition, there are also no known absolute sensors for dynamic pressure that can be used to characterize a source or compare with an uncalibrated gauge.

We are developing a pressure standard for dynamic measurements using line-of-sight absorption spectroscopy to measure dynamic pressure and temperature in a gas [209]. This relies on the same traceability principle as first proposed by Rosasco et al. [210], using the unique quantum mechanical characteristics of the gas-phase molecules (pressure induced line broadening) as the standard for pressure (see Ref. [211] for more details) [212,213]. In contrast to the non-linear two photon CARS (coherent anti-Stokes Raman spectroscopy) approach, we propose employing wavelength modulation spectroscopy that can achieve very high sensitivity with measurement rates on the order of tens of kilohertz [209]. To achieve kHz range dynamic measurements of pressure and temperature using absorption spectroscopy, we need to develop novel methods for executing high-speed-laser scans that cover ~500 GHz (over 16 cm^{-1}) or more in few microseconds. In a recent work [214] we have demonstrated laser scanning over 17 cm^{-1} and more recently extended to 20 cm^{-1}. The broad and rapid tuning has been used to precisely measure pressure and temperature by performing multi-line spectral fits. The target uncertainty goal of our spectroscopic approach is 5%.

16. Conclusions

The scientific activities in the fields encompassed by International Union for Vacuum Science, Techniques and Applications have expanded enormously over the past few years. Researchers worldwide are facing new and exciting challenges in the fields of pure and applied surface science, surface engineering, plasma technologies, electronic and nano-materials, as well as biological materials. The advances in these fields often depend on achievements in vacuum science and pressure metrology. This review paper has highlighted some of the recent advances in these scientific fields in addition to those in vacuum science and technology. New challenges will be met with innovative solutions developed in multidisciplinary teams where physics and chemistry meets electrical engineering, biology and medicine.

Acknowledgements

Authors acknowledge MSC project Thinface (GA 607232), beamtime allocation and technical support at SpLine by J. Rubio, E. Punzón-Quijorna, D. Gallach-Pérez, and D. Gallach (BM25, ESRF) and the NIST/CNST NanoFab facility for providing opportunity to fabricate silicon photonic temperature sensors.

The authors Christian Teichert, Sidney R. Cohen, and Ana G. Silva, would like to thank Nancy Burnham (Worcester Polytechnic Institute), Antonin Fejfar (Czech Academy of Sciences, Prague), Hongjun Gao (Chinese Academy of Sciences, Beijing), Leo Gross and Gerhard Meyer (IBM Rüschlikon), Thomas Michely (University of Cologne), as well as Sander Otte (Kavli Institute of Nanoscience, Delft University of Technology) for providing figures.

The authors acknowledge the financial support from the Slovenian Research Agency (research core funding no. P2-0082) and Czech Science Foundation (17-05095S).

References

[1] http://www.iuvsta.org/.
[2] M. Mozetic, K. Ostrikov, D.N. Ruzic, D. Curreli, U. Cvelbar, A. Vesel, G. Primc, M. Leisch, K. Jousten, O.B. Malyshev, J.H. Hendricks, L. Kover, A. Tagliaferro, O. Conde, A.J. Silvestre, J. Giapintzakis, M. Buljan, N. Radic, G. Drazic, S. Bernstorff, H. Biederman, O. Kylian, J. Hanus, S. Milosevic, A. Galtayries, P. Dietrich, W. Unger, M. Lehocky, V. Sedlarik, K. Stana-Kleinschek, A. Drmota-Petric, J.J. Pireaux, J.W. Rogers, M. Anderle, Recent advances in vacuum sciences and applications, J. Phys. D Appl. Phys. 47 (153001) (2014) (23 pp).
[3] K. Oura, M. Katayama, A.V. Zotov, V.G. Lifshits, A.A. Saranin, Surface Science: An introduction, Springer, Berlin, Heidelberg, 2003.
[4] M. Rajkiewicz, W. Tyszkiewicz, Z. Wertejuk (Eds.), Chemistry and Physics of Complex Materials: Concepts and Applications, Apple Academic Press, 2013(ISBN 9781926895604).
[5] D.R. Baer, M.H. Engelhard, G.E. Johnson, J. Laskin, J.F. Lai, K. Mueller, P. Munusamy, S. Thevuthasan, H.F. Wang, N. Washton, A. Elder, B.L. Baisch, A. Karakoti, S.V.N.T. Kuchibhatla, D. Moon, Surface characterization of nanomaterials and nanoparticles: Important needs and challenging opportunities, J. Vac. Sci. Technol. A 31 (2013) 050820.
[6] E.J. Cho, H. Holback, K.C. Liu, S.A. Abouelmagd, J. Park, Y. Yeo, Nanoparticle characterization: state of the art, challenges, and emerging technologies, Mol. Pharm. 10 (2013) 2093–2110.
[7] V.J. Mohanraj, Y. Chen, Nanoparticles-a review, Trop. J. Pharm. Res. 5 (2006) 561–573.
[8] A. Lopez-Serrano, R.M. Olivas, J.S. Landaluze, C. Camara, Nanoparticles: a global vision. Characterization, separation, and quantification methods. Potential environmental and health impact, Anal Methods UK 6 (2014) 38–56.
[9] A. Kahru, K. Savolainen, Potential hazard of nanoparticles: from properties to biological and environmental effects, Toxicology 269 (2010) 89–91.
[10] S.M. Rosendahl, F. Borondics, T.E. May, T.M. Pedersen, I.J. Burgess, Synchrotron infrared radiation for electrochemical external reflection spectroscopy: a case study using ferrocyanide, Anal. Chem. 83 (2011) 3632–3639.
[11] S. Kumar, X. Liu, F. Borondics, Q.F. Xiao, R.F. Feng, E. Goormaghtigh, F. Nikolajeff, Insights into biochemical alteration in cancer-associated fibroblasts by using novel correlative spectroscopy, Chemistryopen 6 (2017) 149–157.
[12] A.L.D. Kilcoyne, T. Tyliszczak, W.F. Steele, S. Fakra, P. Hitchcock, K. Franck, E. Anderson, B. Harteneck, E.G. Rightor, G.E. Mitchell, A.P. Hitchcock, L. Yang, T. Warwick, H. Ade, Interferometer-controlled scanning transmission X-ray microscopes at the advanced light source, J. Synchrotron Radiat. 10 (2003) 125–136.
[13] H.N. Chapman, MICROSCOPY a new phase for X-ray imaging, Nature 467 (2010) 409–410.
[14] E. Bauer, Surface Microscopy With Low Energy Electrons, Springer, New York, 2014.
[15] C.S.S.R. Kumar, Surface Science Tools for Nanomaterials Characterization, Springer, New York, 2015.
[16] B. Bozzini, M. Amati, L. Gregoratti, M. Kiskinova, In-situ photoelectron microspectroscopy and imaging of electrochemical processes at the electrodes of a self-driven cell, Sci. Rep. UK 3 (2013) 2848.
[17] A. Dazzi, R. Prazeres, E. Glotin, J.M. Ortega, Local infrared microspectroscopy with subwavelength spatial resolution with an atomic force microscope tip used as a photothermal sensor, Opt. Lett. 30 (2005) 2388–2390.
[18] A. Dazzi, R. Prazeres, F. Glotin, J.M. Ortega, Subwavelength infrared spectromicroscopy using an AFM as a local absorption sensor, Infrared Phys. Technol. 49 (2006) 113–121.
[19] A. Dazzi, R. Prazeres, F. Glotin, J.M. Ortega, Analysis of nano-chemical mapping

performed by an AFM-based ("AFMIR") acousto-optic technique, Ultramicroscopy 107 (2007) 1194–1200.
[20] A. Bostwick, E. Rotenberg, J. Avila, M.C. Asensio, Zooming in on electronic structure: nanoARPES at SOLEIL and ALS, Synchrotron Radiation News 25 (2012) 19–25.
[21] J. Avila, M.C. Asensio, First nanoARPES user facility available at SOLEIL: an innovative and powerful tool for studying advanced materials, Synchrotron Radiat. News 27 (2014) 24–30.
[22] J. Avila, I. Razado-Colambo, S. Lorcy, B. Lagarde, J.-L. Giorgetta, F. Polack, M.C. Asensio, ANTARES, a scanning photoemission microscopy beamline at SOLEIL, J. Phys. Conf. Ser. 425 (2013) 192,023, http://dx.doi.org/10.1088/1742-6596/425/19/192023.
[23] P. Vogt, P. De Padova, C. Quaresima, J. Avila, E. Frantzeskakis, M.C. Asensio, A. Resta, B. Ealet, G. Le Lay, Silicene: compelling experimental evidence for graphenelike two-dimensional silicon, Phys. Rev. Lett. 108 (155) (2012) 501.
[24] L.I. Johansson, R. Armiento, J. Avila, C. Xia, S. Lorcy, I.A. Abrikosov, M.C. Asensio, C. Virojanadara, Multiple pi-bands and Bernal stacking of multilayer graphene on C-face SiC, revealed by nano-angle resolved photoemission, Sci. Rep. UK 4 (4157) (2014) 5.
[25] I. Razado-Colambo, J. Avila, J.P. Nys, C. Chen, X. Wallart, M.C. Asensio, D. Vignaud, NanoARPES of twisted bilayer graphene on SiC: absence of velocity renormalization for small angles, Sci. Rep. UK 6 (2016) 27,261.
[26] B. Zhan, C. Li, J. Yang, G. Jenkins, W. Huang, X. Dong, Graphene field-effect transistor and its application for electronic sensing, Small 10 (20) (2014) 4042–4065, http://dx.doi.org/10.1002/smll.201400463.
[27] H. Coy Diaz, J. Avila, C. Chen, R. Addou, M.C. Asensio, M. Batzill, Direct observation of interlayer hybridization and dirac relativistic carriers in graphene/MoS2 van der Waals heterostructures, Nano Lett. 15 (2015) 1135–1140.
[28] Y. Ma, H.C. Diaz, J. Avila, C. Chen, V. Kalappattil, R. Das, M.-H. Phan, T. Čadež, J.M.P. Carmelo, M.C. Asensio, M. Batzill, Angle resolved photoemission spectroscopy reveals spin charge separation in metallic MoSe2 grain boundary, Nat. Commun. 8 (14231) (2017) 14212.
[29] L. Brown, E.B. Lochocki, J. Avila, C.J. Kim, Y. Ogawa, R.W. Havener, D.K. Kim, E.J. Monkman, D.E. Shai, H.F.I. Wei, M.P. Levendorf, M. Asensio, K.M. Shen, J. Park, Polycrystalline graphene with single crystalline electronic structure, Nano Lett. 14 (2014) 5706–5711.
[30] M. Noked, C. Liu, J. Hu, K. Gregorczyk, G.W. Rubloff, S.B. Lee, Electrochemical thin layers in nanostructures for energy storage, Acc. Chem. Res. 49 (10) (2016) 2336–2346, http://dx.doi.org/10.1021/acs.accounts.6b00315 (2016).
[31] H.S. Ko, Introduction: hierarchical nanostructures for energy devices, in: H.S. Ko, C.P. Grigoropoulos (Eds.), Hierarchical Nanostructures for Energy Devices, RSC Nanoscience & Nanotechnology No. 35, 2015, http://dx.doi.org/10.1039/9781849737500-00001.
[32] M.K. Passarelli, C.F. Newman, P.S. Marshall, A. West, I.S. Gilmore, J. Bunch, M.R. Alexander, C.T. Dollery, Single-cell analysis: visualizing pharmaceutical and metabolite uptake in cells with label-free 3D mass spectrometry imaging, Anal. Chem. 87 (2015) 6696–6702.
[33] G. Kourousias, L. Pascolo, P. Marmorato, J. Ponti, G. Ceccone, M. Kiskinova, A. Gianoncelli, High-resolution scanning transmission soft X-ray microscopy for rapid probing of nanoparticle distribution and sufferance features in exposed cells, X-Ray Spectrom. 44 (2015) 163–168.
[34] J.S. Fletcher, N.P. Lockyer, J.C. Vickerman, Developments in molecular sims depth profiling and 3d imaging of biological systems using polyatomic primary ions, Mass Spectrom. Rev. 30 (2011) 142–174.
[35] V. Cizinauskas, N. Elie, A. Brunelle, V. Briedis, Fatty acids penetration into human skin ex vivo: ATOF-SIMS analysis approach, Biointerphases 12 (2017).
[36] B. Winter, Liquid microjet for photoelectron spectroscopy, Nucl. Instrum. Meth. A 601 (2009) 139–150.
[37] A. Jürgensen, N. Esser, R. Hergenröder, Near ambient pressure XPS with a conventional X-ray source, Surf. Interface Anal. 44 (2012) 1100–1103.
[38] J. Knudsen, J.N. Andersen, J. Schnadt, A versatile instrument for ambient pressure X-ray photoelectron spectroscopy: the Lund cell approach, Surf. Sci. 646 (2016) 160–169.
[39] E.G. Michel, Perspectives on surface science, J. Phys. Condens. Matter 22 (8) (2010).
[40] D.M. Eigler, E.K. Schweizer, Positioning single atoms with a scanning tunnelling microscope, Nature 344 (1990) 524–526.
[41] F.E. Kalff, M.P. Rebergen, E. Fahrenfort, J. Girovsky, R. Toskovic, R. Toskovic, J.L. Lado, J. Fernández Rossier, A.F. Otte, A kilobyte rewritable atomic memory, Nat. Nanotechnol. 11 (2016) 926–929.
[42] K.-H. Ernst, S. Baumann, C.P. Lutz, J. Seibel, L. Zoppi, A.J. Heinrich, Pasteur's experiment performed at the nanoscale: manual separation of chiral molecules, one by one, Nano Lett. 15 (2015) 5388–5392.
[43] T. Kudernac, N. Ruangsupapichat, M. Parschau, B. Macia, N. Katsonis, S.R. Harutyunyan, K.-H. Ernst, B.L. Feringa, Electrically driven directional motion of a four-wheeled molecule on a metal surface, Nature 479 (2011) 208–211.
[44] L. Gross, F. Mohn, N. Moll, B. Schuler, A. Criado, E. Guitian, D. Pena, A. Gourdon, G. Meyer, Bond-order discrimination by atomic force microscopy, Science 337 (2012) 1326–1329.
[45] N. Pavliček, B. Schuler, S. Collazos, N. Moll, D. Pérez, E. Guitián, G. Meyer, D. Peña, L. Gross, On-surface generation and imaging of arynes by atomic force microscopy, Nat. Chem. 7 (2015) 623–628.
[46] J. Brede, N. Atodiresei, V. Caciuc, M. Bazarnik, A. Al-Zubi, S. Blügel, R. Wiesendanger, Long-range magnetic coupling between nanoscale organic–metal hybrids mediated by a nanoskyrmion lattice, Nat. Nanotechnol. 9 (2014) 1018–1023.
[47] M. Peres, F. Rocha, N. Catarino, C. Cruz, L.C. Alves, E. Alves, K. Lorenz, A.G. Silva, E. Nogales, I. López, L.I.B. Méndez, J. Piqueras, X. Biquard, B. Daudin, E.G. Víllora, K. Shimamura, 13th Expert Evaluation and Control of Compound Semiconductor Materials and Technologies EXMATEX, Portugal, (June 2016), pp. 6–10.
[48] I. Beinik, M. Kratzer, A. Wachauer, L. Wang, Y.P. Piryatinski, G. Brauer, X.Y. Chen, Y.F. Hsu, A.B. Djurisic, C. Teichert, Photoresponse from single upright-standing ZnO nanorods explored by photoconductive AFM, Beilstein J. Nanotechnol. 4 (2013) 208–217.
[49] M. Müller, M. Hývl, M. Kratzer, C. Teichert, S. Misra, M. Foldyna, L. Yu, P. Roca i Cabarrocas, T. Itoh, Z. Hájková, A. Vetushka, M. Ledinský, J. Kočka, A. Fejfar, Jap. J. Appl. Phys. 54 (2015) 08KA08.
[50] S. Mukhopadhyay, S.R. Cohen, D. Marchak, N. Friedman, I. Pecht, M. Sheves, D. Cahen, Nanoscale electron transport and photodynamics enhancement in lipid-depleted bacteriorhodopsin monomers, ACS Nano 8 (2014) 7714–7722.
[51] A.K. Geim, K.S. Novoselov, The rise of graphene, Nat. Mater. 6 (2007) 183–191.
[52] P. Ajayan, P. Kim, K. Banerjee, Two-dimensional van der Waals materials, Phys. Today 69 (2016) 39–44.
[53] L. Li, Y. Wang, S. Xie, X.-B. Li, Y.-Q. Wang, R. Wu, H. Sun, S. Zhang, H.-J. Gao, Two-dimensional transition metal honeycomb realized: Hf on Ir(111), Nano Lett. 13 (2013) 4671–4674.
[54] C. Herbig, E.H. Åhlgren, U.A. Schröder, A.J. Martínez-Galera, M.A. Arman, J. Kotakoski, J. Knudsen, A.V. Krasheninnikov, T. Michely, Xe irradiation of graphene on Ir(111): from trapping to blistering, Phys. Rev. B 92 (2015) 085429.
[55] M. Kratzer, C. Teichert, Thin film growth of aromatic rod-like molecules on graphene, Nanotechnology 27 (2016) 292001.
[56] A. Matković, J. Genser, D. Lüftner, M. Kratzer, R. Gajić, P. Puschnig, C. Teichert, Epitaxy of highly ordered organic semiconductor crystallite networks supported by hexagonal boron nitride, Sci. Rep. UK 6 (2016) 38519.
[57] B. Schuler, G. Meyer, D. Peña, O.C. Mullins, L. Gross, Unraveling the molecular structures of asphaltenes by atomic force microscopy, J. Am. Chem. Soc. 137 (2015) 9870–9876.
[58] X. Yu, N.A. Burnham, R.B. Mallick, M. Tao, A systematic AFM-based method to measure adhesion differences between micron-sized domains in asphalt binders, Fuel 113 (2013) 443–447.
[59] F.J. Schmied, C. Teichert, L. Kappel, U. Hirn, R. Schennach, Joint strength measurements of individual fiber-fiber bonds: an atomic force microscopy based method, Rev. Sci. Instrum. 83 (2012) 073902.
[60] F.J. Schmied, C. Teichert, L. Kappel, U. Hirn, W. Bauer, R. Schennach, What holds paper together: nanometre scale exploration of bonding between paper fibres, Sci. Rep. UK 3 (2013) 2432.
[61] B. Alling, H. Hogberg, R. Armiento, J. Rosen, L. Hultman, A theoretical investigation of mixing thermodynamics, age-hardening potential, and electronic structure of ternary (M1-xMxB2)-M-1-B-2 alloys with AlB2 type structure, Sci. Rep. UK 5 (2015) 9888.
[62] A. Mockute, J. Palisaitis, B. Alling, P. Berastegui, E. Broitman, L.Å. Näslund, N. Nedfors, J. Lu, J. Jensen, L. Hultman, J. Patscheider, U. Jansson, P.O.Å. Persson, J. Rosen, Age hardening in (Ti1 − xAlx)B2 + Δ thin films, Scr. Mater. 127 (2017) 122–126.
[63] H. Bolvardi, J. Emmerlich, M.T. Baben, D. Music, J. von Appen, R. Dronskowski, J.M. Schneider, Systematic study on the electronic structure and mechanical properties of X2BC (X = Mo, Ti, V, Zr, Nb, Hf, Ta and W), J. Phys. Condens. Matter 045501 (2013) 25.
[64] J. Emmerlich, D. Music, M. Braun, P. Fayek, F. Munnik, J.M. Schneider, A proposal for an unusually stiff and moderately ductile hard coating material: Mo2BC, J. Phys. D. Appl. Phys. 42 (185) (2009) 406.
[65] H. Bolvardi, J. Emmerlich, S. Mráz, M. Arndt, H. Rudigier, J.M. Schneider, Low temperature synthesis of Mo2BC thin films, Thin Solid Films 542 (2013) 5–7.
[66] S. Djaziri, S. Gleich, H. Bolvardi, C. Kirchlechner, M. Hans, C. Scheu, J.M. Schneider, G. Dehm, Are Mo2BC nanocrystalline coatings damage resistant? Insights from comparative tension experiments, Surf. Coat. Technol. 289 (2016) 213–218.
[67] J. Vlcek, J. Rezek, J. Houska, R. Cerstvy, R. Bugyi, Process stabilization and a significant enhancement of the deposition rate in reactive high-power impulse magnetron sputtering of ZrO2 and Ta2O5 films, Surf. Coat. Technol. 236 (2013) 550–556.
[68] J. Rezek, J. Vlček, J. Houška, R. Čerstvý, High-rate reactive high-power impulse magnetron sputtering of Ta–O–N films with tunable composition and properties, Thin Solid Films 566 (2014) 70–77.
[69] B.R. Natarajan, A.H. Eltoukhy, J.E. Greene, T.L. Barr, Mechanisms of reactive sputtering of indium II: growth of indium oxynitride in mixed N2-O2 discharges, Thin Solid Films 69 (1980) 217–227.
[70] J. Vlcek, J. Rezek, J. Houska, T. Kozak, J. Kohout, Benefits of the controlled reactive high-power impulse magnetron sputtering of stoichiometric ZrO2 films, Vacuum 114 (2015) 131–141.
[71] J. Vlcek, A. Belosludtsev, J. Rezek, J. Houska, J. Capek, R. Cerstvy, S. Haviar, High-rate reactive high-power impulse magnetron sputtering of hard and optically transparent HfO2 films, Surf. Coat. Technol. 290 (2016) 58–64.
[72] K. Macák, V. Kouznetsov, J. Schneider, U. Helmersson, I. Petrov, Ionized sputter deposition using an extremely high plasma density pulsed magnetron discharge, J. Vac. Sci. Technol. A 18 (2000) 1533–1537.
[73] G. Greczynski, J. Lu, M.P. Johansson, J. Jensen, I. Petrov, J.E. Greene, L. Hultman, Role of Tin+ and Aln + ion irradiation (n = 1, 2) during Ti1-xAlxN alloy film growth in a hybrid HIPIMS/magnetron mode, Surf. Coat. Technol. 206 (2012) 4202–4211.
[74] G. Greczynski, J. Lu, J. Jensen, I. Petrov, J.E. Greene, S. Bolz, W. Kölker, C. Schiffers, O. Lemmer, L. Hultman, Metal versus rare-gas ion irradiation during

Ti1 − xAlxN film growth by hybrid high power pulsed magnetron/dc magnetron co-sputtering using synchronized pulsed substrate bias, J. Vac. Sci. Technol. A 30 (2012) 061504.
[75] G. Greczynski, J. Lu, J. Jensen, I. Petrov, J.E. Greene, S. Bolz, W. Kölker, C. Schiffers, O. Lemmer, L. Hultman, Strain-free, single-phase metastable Ti0.38Al0.62 N alloys with high hardness: metal-ion energy vs. momentum effects during film growth by hybrid high-power pulsed/dc magnetron cosputtering, Thin Solid Films 556 (2014) 87–98.
[76] G. Greczynski, J. Patscheider, J. Lu, B. Alling, A. Ektarawong, J. Jensen, I. Petrov, J.E. Greene, L. Hultman, Control of Ti1 − xSixN nanostructure via tunable metal-ion momentum transfer during HIPIMS/DCMS co-deposition, Surf. Coat. Technol. 280 (2015) 174–184.
[77] G. Greczynski, J. Lu, S. Bolz, W. Kölker, C. Schiffers, O. Lemmer, I. Petrov, J.E. Greene, L. Hultman, Novel strategy for low-temperature, high-rate growth of dense, hard, and stress-free refractory ceramic thin films, J. Vac. Sci. Technol. A 32 (2014) 041515.
[78] J. Keckes, M. Bartosik, R. Daniel, C. Mitterer, G. Maier, W. Ecker, J. Vila-Comamala, C. David, S. Schoeder, M. Burghammer, X-ray nanodiffraction reveals strain and microstructure evolution in nanocrystalline thin films, Scr. Mater. 67 (2012) 748–751.
[79] M. Stefenelli, J. Todt, A. Riedl, W. Ecker, T. Muller, R. Daniel, M. Burghammer, J. Keckes, X-ray analysis of residual stress gradients in TiN coatings by a Laplace space approach and cross-sectional nanodiffraction: a critical comparison, J. Appl. Crystallogr. 46 (2013) 1378–1385.
[80] J. Zalesak, M. Bartosik, R. Daniel, C. Mitterer, C. Krywka, D. Kiener, P.H. Mayrhofer, J. Keckes, Cross-sectional structure-property relationship in a graded nanocrystalline Ti1 − xAlxN thin film, Acta Mater. 102 (2016) 212–219.
[81] A. Zeilinger, J. Todt, C. Krywka, M. Müller, W. Ecker, B. Sartory, M. Meindlhumer, M. Stefenelli, R. Daniel, C. Mitterer, J. Keckes, In-situ observation of cross-sectional microstructural changes and stress distributions in fracturing TiN thin film during nanoindentation, Sci. Rep. UK 6 (2016) 22670.
[82] I.E. Agency, IEA Statistics - CO2 Emissions From Fuel Combustion - Highlights, OECD/IEA, Paris, France, 2013.
[83] R.D. Lide, CRC Handbook of Chemistry and Physics, 88th ed., CRC Press, Boca Raton, FL, 2007.
[84] S. Sherif, D. Yogi Goswami, E.K. Stefanakos, A. Steinfeld, Handbook of Hydrogen Energy, CRC Press, Taylor & Francis Group, Boca Raton, London, New York, 2014.
[85] D.J. Durbin, C. Malardier-Jugroot, Review of hydrogen storage techniques for on board vehicle applications, Int. J. Hydrog. Energy 38 (2013) 14595–14617.
[86] U.S. Department of Energy, Technical System Targets: Onboard Hydrogen Storage for Light-Duty Fuel Cell Vehicles (updated May 2017), https://www.energy.gov/sites/prod/files/2017/05/f34/fcto_myrdd_table_onboard_h2_storage_systems_doe_targets_ldv_1.pdf.
[87] M. Keding, M. Tajmar, Method and Installation for Storing and Releasing hydrogen, (2008).
[88] M.A.M. Division, Glass bubbles: 3 M energy and advanced materials: 3 M Europe, http://multimedia.3m.com/mws/media/694361O/3m-glass-bubbles-s38.pdf, (2015).
[89] R.F. Bunshah, Deposition Technologies for Films and Coatings - Developments and Applications, Noyes Publications, Park Ridge, New Jersey, U.S.A., 1982.
[90] G.H.S. Schmid, C. Eisenmenger-Sittner, A method for uniformly coating powdery substrates by magnetron sputtering, Surf. Coat. Technol. 236 (2013) 353–360.
[91] G.H.S. Schmid, C. Eisenmenger-Sittner, J. Hell, M. Quirchmair, Austrian Patent AT, 513037 (January 2015), p. 15.
[92] V.L. Popov, Kontaktmechanik und Reibung, Springer Heidelberg, Dordrecht, London, New York, 2010.
[93] Commercial equipment, instruments, or materials are identified in this paper in order to specify the experimental procedure adequately. Such identification is not intended to imply recommendation or endorsement by NIST or any of the other author's institutions, nor is it intended to imply that the materials or equipment identified are necessarily the best available for the purpose.
[94] I. Capan, A. Carvalho, J. Coutinho, Silicon and germanium nanocrystals: properties and characterization, Beilstein J. Nanotechnol. 5 (2014) 1787–1794.
[95] E.G. Barbagiovanni, D.J. Lockwood, P.J. Simpson, L.V. Goncharova, Quantum confinement in Si and Ge nanostructures: theory and experiment, Appl. Phys. Rev. 1 (2014) 011302.
[96] K. Murakami, R. Shirakawa, M. Tsujimura, N. Uchida, N. Fukata, S.-i. Hishita, Phosphorus ion implantation in silicon nanocrystals embedded in SiO2, J. Appl. Phys. 105 (2009) 054307.
[97] A. Mimura, M. Fujii, S. Hayashi, D. Kovalev, F. Koch, Photoluminescence and free-electron absorption in heavily phosphorus-doped Si nanocrystals, Phys. Rev. B 62 (2000) 12625–12627.
[98] I.F. Crowe, N. Papachristodoulou, M.P. Halsall, N.P. Hylton, O. Hulko, A.P. Knights, P. Yang, R.M. Gwilliam, M. Shah, A.J. Kenyon, Donor ionization in size controlled silicon nanocrystals: The transition from defect passivation to free electron generation, J. Appl. Phys. 113 (2013) 024304.
[99] M. Zacharias, J. Heitmann, R. Scholz, U. Kahler, M. Schmidt, J. Bläsing, Size-controlled highly luminescent silicon nanocrystals: a SiO/SiO2 superlattice approach, Appl. Phys. Lett. 80 (2002) 661–663.
[100] D.K. Schroder, Semiconductor Material and Device Characterization, Wiley, New Jersey, 2006.
[101] O. Jambois, Y. Berencen, K. Hijazi, M. Wojdak, A.J. Kenyon, F. Gourbilleau, R. Rizk, B. Garrido, Current transport and electroluminescence mechanisms in thin SiO2 films containing Si nanocluster-sensitized erbium ions, J. Appl. Phys. 106 (2009) 063526.
[102] X. Zhou, K. Usami, M.A. Rafiq, Y. Tsuchiya, H. Mizuta, S. Oda, Influence of nanocrystal size on the transport properties of Si nanocrystals, J. Appl. Phys. 104 (2008) 024518.
[103] M. Buljan, J. Grenzer, V. Holý, N. Radić, T. Mišić-Radić, S. Levichev, S. Bernstorff, B. Pivac, I. Capan, Structural and charge trapping properties of two bilayer (Ge + SiO2)/SiO2 films deposited on rippled substrate, Appl. Phys. Lett. 97 (2010) 163117.
[104] L. Dobaczewski, S. Bernardini, P. Kruszewski, P.K. Hurley, V.P. Markevich, I.D. Hawkins, A.R. Peaker, Energy state distributions of the Pb centers at the (100), (110), and (111) Si/SiO2 interfaces investigated by Laplace deep level transient spectroscopy, Appl. Phys. Lett. 92 (2008) 242104.
[105] J. Martin-Sanchez, A. Chahboun, M.J.M. Gomes, A.G. Rolo, B. Pivac, I. Capan, Carrier storage in Ge nanoparticles produced by pulsed laser deposition, Phys. Status. Solidi R 6 (2012) 223–225.
[106] I. Capan, V. Janicki, R. Jacimovic, B. Pivac, C–V and DLTS studies of radiation induced Si–SiO2 interface defects, Nucl. Instrum. Methods Phys. Res., Sect. B 282 (2012) 59–62.
[107] I.V. Antonova, V.I. Popov, S.A. Smagulova, J. Jedrzejewski, I. Balberg, Charge deep-level transient spectroscopy of SiO2 and Al2O3 layers with embedded Ge nanocrystals, J. Appl. Phys. 113 (2013) 084308.
[108] D.G. Castner, Biomedical surface analysis: evolution and future directions (review), Biointerphases 12 (2017) 02C301.
[109] S. Bauer, P. Schmuki, K. von der Mark, J. Park, Engineering biocompatible implant surfaces part I: materials and surfaces, Prog. Mater. Sci. 58 (2013) 261–326.
[110] A. Flasker, M. Kulkarni, K. Mrak-Poljsak, I. Junkar, S. Cucnik, P. Zigon, A. Mazare, P. Schmuki, A. Iglic, S. Sodin-Semrl, Binding of human coronary artery endothelial cells to plasma-treated titanium dioxide nanotubes of different diameters, J. Biomed. Mater. Res. A 104 (2016) 1113–1120.
[111] P. Rivolo, S.M. Severino, S. Ricciardi, F. Frascella, F. Geobaldo, Protein immobilization on nanoporous silicon functionalized by RF activated plasma polymerization of acrylic acid, J. Colloid Interface Sci. 416 (2014) 73–80.
[112] D.G. Perez, E.P. Quijorna, R. Sanz, V. Torres-Costa, J.P.G. Ruiz, M.M. Silvan, Nanotopography enhanced mobility determines mesenchymal stem cell distribution on micropatterned semiconductors bearing nanorough areas, Colloid Surf. B 126 (2015) 146–153.
[113] A. Balamurugan, S. Rajeswari, G. Balossier, A.H.S. Rebelo, J.M.F. Ferreira, Corrosion aspects of metallic implants - an overview, Mater. Corros. 59 (2008) 855–869.
[114] J. Black, Orthopedic Biomaterials in Research and Practice, Churchill-Livingstone, New York, 1988, p. 276.
[115] B.D. Ratner, A.S. Hoffman, F.J. Schoen, J.E. Lemons, Biomaterials Science, An Introduction to Materials in Medicine, 2nd ed., Elsevier, San Diego, 2004.
[116] Y.-J. Park, Y.-H. Song, J.-H. An, H.-J. Song, K.J. Anusavice, Cytocompatibility of pure metals and experimental binary titanium alloys for implant materials, J. Dent. 41 (2013) 1251–1258.
[117] A. Ithurbide, I. Frateur, A. Galtayries, P. Marcus, XPS and flow-cell EQCM study of albumin adsorption on passivated chromium surfaces: influence of potential and pH, Electrochim. Acta 53 (2007) 1336–1345.
[118] J. Cheng, B. Liu, Y.H. Wu, Y.F. Zheng, Comparative in vitro study on pure metals (Fe, Mn, Mg, Zn and W) as biodegradable metals, J. Mater. Sci. Technol. 29 (2013) 619–627.
[119] X. Gu, Y. Zheng, Y. Cheng, S. Zhong, T. Xi, In vitro corrosion and biocompatibility of binary magnesium alloys, Biomaterials 30 (2009) 484–498.
[120] Y.F. Zheng, X.N. Gu, F. Witte, Biodegradable metals, Mater. Sci. Eng. R. Rep. 77 (2014) 1–34.
[121] H. Hermawan, D. Dubé, D. Mantovani, Developments in metallic biodegradable stents, Acta Biomater. 6 (2010) 1693–1697.
[122] F. Witte, The history of biodegradable magnesium implants: a review, Acta Biomater. 6 (2010) 1680–1692.
[123] S. Thomas, N.V. Medhekar, G.S. Frankel, N. Birbilis, Corrosion mechanism and hydrogen evolution on Mg, Curr. Opinion Solid State Mater. Sci. 19 (2015) 85–94.
[124] G.K. Hyde, S.D. McCullen, S. Jeon, S.M. Stewart, H. Jeon, E.G. Loboa, G.N. Parsons, Atomic layer deposition and biocompatibility of titanium nitride nano-coatings on cellulose fiber substrates, Biomed. Mater. 4 (2009) 025001.
[125] K. Gregorczyk, M. Knez, Hybrid nanomaterials through molecular and atomic layer deposition: Top down, bottom up, and in-between approaches to new materials, Prog. Mater. Sci. 75 (2016) 1–37.
[126] L.X. Shi, Y.X. Lu, J. Sun, J. Zhang, C.Q. Sun, J.Q. Liu, J.C. Shen, Site-selective lateral multilayer assembly of bienzyme with polyelectrolyte on ITO electrode based on electric field-induced directly layer-by-layer deposition, Biomacromolecules 4 (2003) 1161–1167.
[127] J. Hernandez-Montelongo, D. Gallach, N. Naveas, V. Torres-Costa, A. Climent-Font, J.P. Garcia-Ruiz, M. Manso-Silvan, Calcium phosphate/porous silicon biocomposites prepared by cyclic deposition methods: spin coating vs electrochemical activation, Mater. Sci. Eng. C Mater. 34 (2014) 245–251.
[128] J.A. Bearden, A.F. Burr, Reevaluation of X-ray atomic energy levels, Rev. Mod. Phys. 39 (1967) 125–142.
[129] Y.H. Ogata, K. Kobayashi, M. Motoyama, Electrochemical metal deposition on silicon, Curr. Opin. Solid State Mater. 10 (2006) 163–172.
[130] A.Y. Lo, C. Wang, W.H. Hung, A.M. Zheng, B. Sen, Nano- and biomaterials for sustainable development, J. Nanomater. 2015 (2015) 129894.
[131] H. Zhang, J. Shih, J. Zhu, N.A. Kotov, Layered nanocomposites from gold nanoparticles for neural prosthetic devices, Nano Lett. 12 (2012) 3391–3398.
[132] S. Maher, T. Kumeria, Y. Wang, G. Kaur, D. Fathalla, G. Fetih, A. Santos, F. Habib, A. Evdokiou, D. Losic, From the mine to cancer therapy: natural and biodegradable theranostic silicon nanocarriers from diatoms for sustained delivery of chemotherapeutics, Adv. Healthc. Mater. 5 (2016) 2667–2678.

[133] C. Buzea, I.I. Pacheco, K. Robbie, Nanomaterials and nanoparticles: sources and toxicity, Biointerphases 2 (2007) MR17–MR71.
[134] M.A. Dobrovolskaia, A.K. Patri, J.W. Zheng, J.D. Clogston, N. Ayub, P. Aggarwal, B.W. Neun, J.B. Hall, S.E. McNeil, Interaction of colloidal gold nanoparticles with human blood: effects on particle size and analysis of plasma protein binding profiles, Nanomed. Nanotechnol. 5 (2009) 106–117.
[135] R. Capomaccio, I.O. Jimenez, P. Colpo, D. Gilliland, G. Ceccone, F. Rossi, L. Calzolai, Determination of the structure and morphology of gold nanoparticle-HSA protein complexes, Nanoscale 7 (2015) 17653–17657.
[136] D.W. Grainger, D.G. Castner, Nanobiomaterials and nanoanalysis: opportunities for improving the science to benefit biomedical technologies, Adv. Mater. 20 (2008) 867–877.
[137] A.G. Shard, A. Straightforward Method, For interpreting XPS data from core–shell nanoparticles, J. Phys. Chem. C 116 (2012) 16806–16813.
[138] D.R. Baer, D.J. Gaspar, P. Nachimuthu, S.D. Techane, D.G. Castner, Application of surface chemical analysis tools for characterization of nanoparticles, Anal. Bioanal. Chem. 396 (2010) 983–1002.
[139] N.A. Belsey, D.J.H. Cant, C. Minelli, J.R. Araujo, B. Bock, P. Brüner, D.G. Castner, G. Ceccone, J.D.P. Counsell, P.M. Dietrich, M.H. Engelhard, S. Fearn, C.E. Galhardo, H. Kalbe, J.W. Kim, L. Lartundo-Rojas, H.S. Luftman, T.S. Nunney, J. Pseiner, E.F. Smith, V. Spampinato, J.M. Sturm, A.G. Thomas, J.P.W. Treacy, L. Veith, M. Wagstaffe, H. Wang, M. Wang, Y.-C. Wang, W. Werner, L. Yang, A.G. Shard, Versailles project on advanced materials and standards interlaboratory study on measuring the thickness and chemistry of nanoparticle coatings using XPS and LEIS, J. Phys. Chem. C 120 (2016) 24070–24079.
[140] A. Hurlbatt, A.R. Gibson, S. Schroter, J. Bredin, A.P.S. Foote, P. Grondein, D. O'Connell, T. Gans, Concepts, capabilities, and limitations of global models: a review, Plasma Process. Polym. 14 (2017).
[141] B. Bruneau, T. Gans, D. O'Connell, A. Greb, E.V. Johnson, J.-P. Booth, Strong ionization asymmetry in a geometrically symmetric radio frequency capacitively coupled plasma induced by sawtooth voltage waveforms, Phys. Rev. Lett. 114 (2015) 125002.
[142] B. Bruneau, T. Lafleur, T. Gans, D. O'Connell, A. Greb, I. Korolov, A. Derzsi, Z. Donko, S. Brandt, E. Schüngel, J. Schulze, P. Diomede, D.J. Economou, S. Longo, E. Johnson, J.-P. Booth, Effect of gas properties on the dynamics of the electrical slope asymmetry effect in capacitive plasmas: comparison of Ar, H2 and CF4, Plasma Sources Sci. Technol. 25 (2016) 1–6.
[143] A. Rezvanov, A.V. Miakonkikh, A.S. Vishnevskiy, K.V. Rudenko, M.R. Baklanov, Cryogenic etching of porous low-k dielectrics in CF3Br and CF4 plasmas, J. Vac. Sci. Technol. B Nanotechnol. Microelectron. Mater. Process. Meas. Phenom. 35 (2017) 021204.
[144] N. Recek, G. Primc, A. Vesel, M. Mozetic, J. Avila, I. Razado-Colambo, M.C. Asensio, Degradation of albumin on plasma-treated polystyrene by soft X-ray exposure, Polymers Basel 8 (2016).
[145] E. Schungel, I. Korolov, B. Bruneau, A. Derzsi, E. Johnson, D. O'Connell, T. Gans, J.P. Booth, Z. Donko, J. Schulze, Tailored voltage waveform capacitively coupled plasmas in electronegative gases: frequency dependence of asymmetry effects, J. Phys. D. Appl. Phys. 49 (2016) 265203.
[146] A. Derzsi, B. Bruneau, A.R. Gibson, E. Johnson, D. O'Connell, T. Gans, J.P. Booth, Z. Donko, Power coupling mode transitions induced by tailored voltage waveforms in capacitive oxygen discharges, Plasma Sources Sci. Technol. 26 (2017) 034002.
[147] A. Greb, A.R. Gibson, K. Niemi, D. O'Connell, T. Gans, Influence of surface conditions on plasma dynamics and electron heating in a radio-frequency driven capacitively coupled oxygen plasma, Plasma Sources Sci. Technol. 24 (2015) 044003.
[148] M. Gorjanc, M. Mozetič, G. Primc, A. Vesel, K. Spasić, N. Puač, Z.L. Petrović, M. Kert, Plasma treated polyethylene terephthalate for increased embedment of UV-responsive microcapsules, Appl. Surf. Sci. 19 (2017) 224–234.
[149] R. Zaplotnik, A. Vesel, M. Mozetic, Investigation of reactive plasma species created in SO2 by an inductively coupled RF discharge in E- and H-mode, J. Appl. Phys. 120 (2016).
[150] N. Recek, M. Resnik, R. Zaplotnik, M. Mozetic, H. Motaln, T. Lah-Turnsek, A. Vesel, Cell proliferation on polyethylene terephthalate treated in plasma created in SO2/O-2 mixtures, Polymers Basel 9 (2017).
[151] A.M. Hirst, M.S. Simms, V.M. Mann, N.J. Maitland, D. O'Connell, F.M. Frame, Low-temperature plasma treatment induces DNA damage leading to necrotic cell death in primary prostate epithelial cells, Br. J. Cancer 112 (2015) 1536–1545.
[152] J. Golda, J. Held, B. Redeker, M. Konkowski, P. Beijer, A. Sobota, G. Kroesen, N.S.J. Braithwaite, S. Reuter, M.M. Turner, T. Gans, D. O'Connell, V. Schulz-von der Gathen, Concepts and characteristics of the 'COST reference microplasma jet, J. Phys. D. Appl. Phys. 49 (2016) 1–11.
[153] Y. Gorbanev, D. O'Connell, V. Chechik, Non-thermal plasma in contact with water: the origin of species, Chem. 22 (2016) 3496–3505.
[154] A.M. Hirst, F.M. Frame, M. Arya, N.J. Maitland, D. O'Connell, Low temperature plasmas as emerging cancer therapeutics: the state of play and thoughts for the future, Tumor Biol. 37 (2016) 7021.
[155] K. Niemi, D. O'Connell, N. de Oliveira, D. Joyeux, L. Nahon, J.P. Booth, T. Gans, Absolute atomic oxygen and nitrogen densities in radio-frequency driven atmospheric pressure cold plasmas: synchrotron vacuum ultra-violet high-resolution Fourier-transform absorption measurements, Appl. Phys. Lett. 103 (2013) 034102.
[156] G. Primc, A. Vesel, G. Dolanc, D. Vrančić, M. Mozetič, Recombination of oxygen atoms along a glass tube loaded with a copper sample, Vacuum 138 (2017) 224–229.
[157] K. Jousten, J. Hendricks, D. Barker, K. Douglas, S. Eckel, P. Egan, J. Fedchak, J. Flügge, C. Gaiser, D. Olson, J. Ricker, T. Rubin, W. Sabuga, J. Scherschligt, R. Schödel, U. Sterr, J. Stone, G. Strouse, Perspectives for a new realization of the pascal by optical methods, Metrologia 54 (2017) S146, http://dx.doi.org/10.1088/1681-7575/aa8a4d.
[158] J. Ricker, J. Hendricks, B. Thomas, D. Pražák, K. Tokihiko, T. Jorge, S. Irina, Final report on the key comparison CCM.P-K4.2012 in absolute pressure from 1 Pa to 10 kPa, Metrologia 54 (2017) 07002.
[159] A.P. Miiller, G. Cignolo, M.P. Fitzgerald, M.P. Perkin, Final report on key comparison CCM.P-K5 of differential pressure standards from 1 Pa to 1000 Pa, Metrologia 39 (2002) 07002.
[160] C. Tilford, A. Miiller, S. Lu, A new low-range absolute pressure standard, Proc. 1998 NCSL Workshop and Symposium, 1998, pp. 211–219.
[161] C. Tilford, New developments in barometric range pressure standards, Proc. 1988 NCSL Workshop and Symposium, 35-15 1988, p. 35-31.
[162] P.F. Egan, J.A. Stone, J.H. Hendricks, J.E. Ricker, G.E. Scace, G.F. Strouse, Performance of a dual Fabry-Perot cavity refractometer, Opt. Lett. 40 (2015) 3945–3948.
[163] J.A. Stone, J.E. Decker, P. Gill, P. Juncar, A. Lewis, G.D. Rovera, M. Viliesid, Advice from the CCL on the use of unstabilized lasers as standards of wavelength: the helium-neon laser at 633 nm, Metrologia 46 (2009) 11–18.
[164] P.F. Egan, J.A. Stone, J.E. Ricker, J.H. Hendricks, Comparison measurements of low-pressure between a laser refractometer and ultrasonic manometer, Rev. Sci. Instrum. (2016) 87.
[165] M. Puchalski, K. Piszczatowski, J. Komasa, B. Jeziorski, K. Szalewicz, Theoretical determination of the polarizability dispersion and the refractive index of helium, Phys. Rev. A (2016) 93.
[166] J. Stone, P. Egan, J. Hendricks, G. Strouse, D. Olson, J. Ricker, G. Scace, D. Gerty, Metrology for comparison of displacements at the picometer level, Key Eng. Mater. 625 (2015) 79–84.
[167] C.J. Foot, Atomic Physics, Oxford University Press, 2005.
[168] K.M. O'Hara, S.R. Granade, M.E. Gehm, T.A. Savard, S. Bali, C. Freed, J.E. Thomas, Ultrastable CO2 laser trapping of lithium fermions, Phys. Rev. Lett. 82 (1999) 4204–4207.
[169] J. Scherschligt, J.A. Fedchak, D.S. Barker, S. Eckel, N. Klimov, C. Makrides, E. Tiesinga, Development of a new UHV/XHV pressure standard (cold atom vacuum standard), Metrologia 54 (2017) S125.
[170] D.E. Fagnan, J. Wang, C. Zhu, P. Djuricanin, B.G. Klappauf, J.L. Booth, K.W. Madison, Observation of quantum diffractive collisions using shallow atomic traps, Phys. Rev. A 80 (2009) 022712.
[171] T. Arpornthip, C.A. Sackett, K.J. Hughes, Vacuum-pressure measurement using a magneto-optical trap, Phys. Rev. A 85 (2012) 033420.
[172] J.-P. Yuan, Z.-H. Ji, Y.-T. Zhao, X.-F. Chang, L.-T. Xiao, S.-T. Jia, Simple, reliable, and nondestructive method for the measurement of vacuum pressure without specialized equipment, Appl. Opt. 52 (2013) 6195–6200.
[173] V.B. Makhalov, K.A. Martiyanov, A.V. Turlapov, Primary vacuometer based on an ultracold gas in a shallow optical dipole trap, Metrologia 53 (2016) 1287.
[174] J.S. Donner, S.A. Thompson, M.P. Kreuzer, G. Baffou, R. Quidant, Mapping intracellular temperature using green fluorescent protein, Nano Lett. 12 (2012) 2107–2111.
[175] C.W. Meyer, D.C. Meier, C.B. Montgomery, S. Semancik, Temperature measurements of microhotplates using fluorescence thermometry, Sensors Actuators A Phys. 127 (2006) 235–240.
[176] Z. Ahmed, E.A. Gooding, K.V. Pimenov, L. Wang, S.A. Asher, UV resonance Raman determination of molecular mechanism of poly(*N*-isopropylacrylamide) volume phase transition, J. Phys. Chem. B 113 (2009) 4248–4256.
[177] Z. Ahmed, J.P. Scaffidi, S.A. Asher, Circular dichroism and UV-resonance Raman investigation of the temperature dependence of the conformations of linear and cyclic elastin, Biopolymers 91 (2009) 52–60.
[178] Z. Ahmed, N.S. Myshakina, S.A. Asher, Dependence of the AmII'p proline Raman band on peptide conformation, J. Phys. Chem. B 113 (2009) 11252–11259.
[179] S.J. Mihailov, Fiber Bragg grating sensors for harsh environments, Sensors Basel 12 (2012) 1898–1918.
[180] A.D. Kersey, T.A. Berkoff, Fiber-optic Bragg-grating differential-temperature sensor, IEEE Photon. Technol. Lett. 4 (1992) 1183–1185.
[181] Y.J. Rao, D.J. Webb, D.A. Jackson, L. Zhang, I. Bennion, In-fiber Bragg-grating temperature sensor system for medical applications, J. Lightwave Technol. 15 (1997) 779–785.
[182] H.T. Xu, M. Hafezi, J. Fan, J.M. Taylor, G.F. Strouse, Z. Ahmed, Ultra-sensitive chip-based photonic temperature sensor using ring resonator structures, Opt. Express 22 (2014) 3098–3104.
[183] M.-S. Kwon, W.H. Steier, Microring-resonator-based sensor measuring both the concentration and temperature of a solution, Opt. Express 16 (2008) 9372–9377.
[184] B. Guha, B.B.C. Kyotoku, M. Lipson, CMOS-compatible athermal silicon microring resonators, Opt. Express 18 (2010) 3487–3493.
[185] G.-D. Kim, H.-S. Lee, C.-H. Park, S.-S. Lee, B.T. Lim, H.K. Bae, W.-G. Lee, Silicon photonic temperature sensor employing a ring resonator manufactured using a standard CMOS process, Opt. Express 18 (2010) 22215–22221.
[186] Z. Ahmed, N.N. Klimov, K. Douglass, J. Fedchak, J. Scherschligt, J. Hendricks, J. Ricker, G. Strouse, Towards photonics enabled quantum metrology of temperature, pressure, and vacuum, Dekker Encyclopedia of Nanoscience and Nanotechnology, Dekker Encyclopedia of Nanoscience and Nanotechnology, Taylor & Francis, 2016.
[187] A. Jamgochian, J. Quintavalle, A. Torres-Diaz, J. Filla, G.F. Strouse, Z. Ahmed, Developing Microwave Photonic Temperature Sensors, Progress in Electromagnetics Research Symposium (PIERS), The Electromagnetics Academy, Prague, Czech Republic, 2015, pp. 2403–2407.
[188] D.A. Krohn, Fiber Optic Sensors: Fundamentals and Applications, 3rd ed., ISA, Research Triangle, NC, 2000.

[189] Z. Ahmed, J. Filla, W. Guthrie, J. Quintavalle, Fiber Bragg grating based thermometry, NCSLI Measure 10 (2015) 28–31.
[190] P.C. Liacouras, G.T. Grant, K. Choudhry, G.F. Strouse, Z. Ahmed, Fiber Bragg gratings embedded in 3D-printed scaffolds, NCSLI Measure 10 (2015) 50–52.
[191] J.A. Guemes, J.M. Menendez, Response of Bragg grating fiber-optic sensors when embedded in composite laminates, Compos. Sci. Technol. 62 (2002) 959–966.
[192] K.S.C. Kuang, R. Kenny, M.P. Whelan, W.J. Cantwell, P.R. Chalker, Embedded fibre Bragg grating sensors in advanced composite materials, Compos. Sci. Technol. 61 (2001) 1379–1387.
[193] N.N. Klimov, S. Mittal, M. Berger, Z. Ahmed, On-chip silicon waveguide Bragg grating photonic temperature sensor, Opt. Lett. 40 (2015) 3934–3936.
[194] N.N. Klimov, M. Berger, Z. Ahmed, Characterization of Ring Resonator Structures for Applications in Photonic Thermometry, Advance Photonics Congress, The Optical Society, Boston, 2015.
[195] N.N. Klimov, M. Berger, Z. Ahmed, Silicon photonic temperature sensors, WorldTech Connect, 2015.
[196] N.N. Klimov, M. Berger, Z. Ahmed, Towards reproducible ring resonator based temperature sensors, Sens. Transducers 191 (2015) 63–66.
[197] N.N. Klimov, T. Purdy, Z. Ahmed, On-chip silicon photonic thermometers: from waveguide Bragg grating to ring resonators sensors, Proc. SPIE 9486, Advanced Environmental, Chemical, and Biological Sensing Technologies XII, Washington, DC, 2015 (pp. 948609-948609-948608).
[198] Z. Ahmed, S.G. Chou, K. Siegrist, D.F. Plusquellic, State-resolved THz spectroscopy and dynamics of crystalline peptide-water systems, Faraday Discuss. 150 (2011) 175–192.
[199] M.F.J. Brunt, C.R. Pond, J. Biundo, Gasoline Engine Knock Analysis using Cylinder Pressure Data, SAE International, 1998.
[200] M. Syrimis, D.N. Assanis, Knocking cylinder pressure data characteristics in a spark-ignition engine, J. Eng. Gas Turbines Power 125 (2003) 494–499.
[201] C. Hudson, X. Gao, R. Stone, Knock measurement for fuel evaluation in spark ignition engines, Fuel 80 (2001) 395–407.
[202] G. Paniagua, R. Denos, Digital compensation of pressure sensors in the time domain, Exp. Fluids 32 (2002) 417–424.
[203] J.M. Ortega, Non-lethal blast wave interactions with a human head, Comput. Fluids 52 (2011) 92–103.
[204] M.W. Courtney, A.C. Courtney, Working toward exposure thresholds for blast-induced traumatic brain injury: thoracic and acceleration mechanisms, NeuroImage 54 (2011) S55–S61.
[205] A. Nakagawa, G.T. Manley, A.D. Gean, K. Ohtani, R. Armonda, A. Tsukamoto, H. Yamamoto, K. Takayama, T. Tominaga, Mechanisms of primary blast-induced traumatic brain injury: insights from shock-wave research, J. Neurotrauma 28 (2011) 1101–1119.
[206] S. Poeggel, D. Tosi, D. Duraibabu, G. Leen, D. McGrath, E. Lewis, Optical fibre pressure sensors in medical applications, Sensors Basel 15 (2015) 17115–17148.
[207] M. Brauer, K. Krupka, Advanced pressure sensors with high flexibility for side crash detection, in: J. Valldorf, W. Gessner (Eds.), Advanced Microsystems for Automotive Applications, 2006 Springer, Berlin Heidelberg, Berlin, Heidelberg, 2006, pp. 45–51.
[208] J. Hjelmgren, Dynamic Measurement of Pressure: A Literature Survey, SP Rapport, Swedish National Testing Institute, 2002, pp. 1–65.
[209] K.O. Douglass, D.A. Olson, Towards a standard for the dynamic measurement of pressure based on laser absorption spectroscopy, Metrologia 53 (2016).
[210] G.J. Rosasco, V.E. Bean, W.S. Hurst, A proposed dynamic pressure and temperature primary standard, J. Res. Natl. Inst. Stan. 95 (1990) 33–47.
[211] P.F. Bernath, Spectra of Atoms and Molecules, 2nd ed., Oxford University Press, New York, 2005.
[212] J. Tennyson, P.F. Bernath, A. Campargue, A.G. Csaszar, L. Daumont, R.R. Gamache, J.T. Hodges, D. Lisak, O.V. Naumenko, L.S. Rothman, H. Tran, N.F. Zobov, J. Buldyreva, C.D. Boone, M.D. De Vizia, L. Gianfrani, J.M. Hartmann, R. McPheat, D. Weidmann, J. Murray, N.H. Ngo, O.L. Polyansky, Recommended isolated-line profile for representing high-resolution spectroscopic transitions (IUPAC Technical Report), Pure Appl. Chem. 86 (2014) 1931–1943.
[213] L.S. Rothman, I.E. Gordon, Y. Babikov, A. Barbe, D. Chris Benner, P.F. Bernath, M. Birk, L. Bizzocchi, V. Boudon, L.R. Brown, A. Campargue, K. Chance, E.A. Cohen, L.H. Coudert, V.M. Devi, B.J. Drouin, A. Fayt, J.M. Flaud, R.R. Gamache, J.J. Harrison, J.M. Hartmann, C. Hill, J.T. Hodges, D. Jacquemart, A. Jolly, J. Lamouroux, R.J. Le Roy, G. Li, D.A. Long, O.M. Lyulin, C.J. Mackie, S.T. Massie, S. Mikhailenko, H.S.P. Müller, O.V. Naumenko, A.V. Nikitin, J. Orphal, V. Perevalov, A. Perrin, E.R. Polovtseva, C. Richard, M.A.H. Smith, E. Starikova, K. Sung, S. Tashkun, J. Tennyson, G.C. Toon, V.G. Tyuterev, G. Wagner, The HITRAN2012 molecular spectroscopic database, J. Quant. Spectrosc. Radiat. Transf. 130 (2013) 4–50.
[214] Z. Ahmed, D. Olson, K.O. Douglass, Precision spectroscopy to enable traceable dynamic measurements of pressure, Conf. Laser Electr. (2016), http://dx.doi.org/10.1364/CLEO_AT.2016.ATu1J.1.